Fabricage van nanofotonische structuren
met gefocusseerde ionenbundels

Focused Ion Beam Processing of Nanophotonic Structures

Jonathan Schrauwen

Promotor: prof. dr. ir. D. Van Thourhout
Proefschrift ingediend tot het behalen van de graad van
Doctor in de Ingenieurswetenschappen: Toegepaste Natuurkunde

Vakgroep Informatietechnologie
Voorzitter: prof. dr. ir. D. De Zutter
Faculteit Ingenieurswetenschappen
Academiejaar 2008 - 2009

UNIVERSITEIT
GENT

ISBN 978-90-8578-254-4
NUR 926
Wettelijk depot: D/2009/10.500/11

Promotor:

Prof. dr. ir. D. Van Thourhout	Universiteit Gent, INTEC

Examencommissie:

Prof. dr. ir. D. De Zutter, voorzitter	Universiteit Gent, INTEC
Prof. dr. ir. R. Baets	Universiteit Gent, INTEC
Prof. dr. ir. P. Bienstman, secretaris	Universiteit Gent, INTEC
Prof. dr. ir. M. Burgelman	Universiteit Gent, ELIS
Prof. dr. ir. R.M. De Ridder	Universiteit Twente
Dr. ir. S. Reyntjens	FEI Company
Dr. ir. G. Roelkens	Universiteit Gent, INTEC

Universiteit Gent
Faculteit Ingenieurswetenschappen

Vakgroep Informatietechnologie (INTEC)
Sint-Pietersnieuwstraat 41
9000 Gent
Belgie

Tel.: +32-9-264.33.19
Fax: +32-9-264.35.93
http://www.intec.ugent.be

Een deel van dit werk werd uitgevoerd in het kader van het Europees project ePIXnet.

Dankwoord

Mijn doctoraat. Helemaal klaar. Maar niet zonder een woord van dank de wereld in te sturen.

Ik zou om te beginnen de kans willen grijpen om mijn promotor en begeleider Dries en Roel te bedanken. Vooral om me de vrijheid te geven om zelf fouten te maken. En om een helpende hand te zijn bij het oplossen ervan. Een doctoraatsstudent begeleiden heeft iets van ouderschap; jullie vaderschap was schitterend. Ook al durfde ik jullie al eens de foute vraag stellen (zoals aan Dries tijdens onze eerste autorit), of een duwtje teveel geven richting water.

Ik wil ook graag de vele mensen bedanken die bijgedragen hebben tot de exact wetenschappelijke inzichten die ik verworven heb tijdens mijn doctoraat. De gesprekken met Wico Hopman, Edwin Klein en Feridun Ay van Universiteit Twente hebben hier veel toe bijgedragen, alsook de vele vragen die ik mocht stellen aan Steve Reyntjens en zijn collega's van FEI, Christophe Detavernier en de mensen van de S1, en aan Hugo Bender van IMEC. Liesbet en Jeremie, bedankt om met mij vele uren naar het scherm van de FIB te zitten staren en om werkjes voor anderen uit mijn handen te nemen. Steven, zonder u zou de cleanroom vierkant draaien. Maar vooral Dries, bedankt om altijd tijd te maken.

Wat de minder exacte kant van de wetenschappen betreft heb ik enorm veel levenswijsheid verworven in de Photonics groep tijdens de vele lange extracollegiale gesprekken gepaard met spijs en drank in de Vooruit, de Marimain, den Backstage... Menige kroeg zag onze zware bieren en andere spirituoza over de toog schuiven als waren het watertjes. Bedankt iedereen om op mijn directe vragen te antwoorden en om geen enkel gespreksonderwerp te mijden. Bedankt occasionele rokers om met mij vele 'groepspakken' te delen. De Photonics groep is bangelijk.

Een andere groep mensen die een bijzondere rol gespeeld hebben in de voorbije jaren zijn mijn ex-burgie-klasgenoten van de natuurkunde. Een groot deel van onze studentikoze tijd heeft zich afge-

speeld in de laatste vier jaar. Bedankt voor de menige feestjes, etentjes en uitjes; ze staan gegrift in mijn geheugen. Bedankt voor het beste verjaardagscadeau van mijn leven. Iedereen bewandelt vanaf nu andere paden, maar ik ben zeker dat die zigzaggend door elkaar zullen kronkelen.

De (hoofdzakelijk) West-Vlaamse moatens hebben in de voorbije vier jaar gezorgd voor dynamiek. Allemaal energiebommen zijn jullie. Van feestjes op het ministerie van financiën, over scheuren in Ghost Valley, tot roeien naar Engeland; jullie waren erbij. Over mijn favoriete uitlaatklep gesproken!

Mijn Antwerpse makkers en vaste waarden gaan al veel langer terug dan de voorbije vier jaar. Aan *the magic four* heb ik al teveel herinneringen om ze hier allemaal neer te schrijven. En ik hoop dat ik er al niet teveel vergeten ben door al die wetenschap.

Tenslotte wil ik mijn familie bedanken. Mama en Papa, bedankt om altijd in mij te geloven. Ben, bedankt om een groot deel van het doctoraatspad voor mij te effenen. De vele lunchgesprekken over ons werk hebben me veel bijgedragen. Ben, Natalie en Sarah, bedankt voor de familiale warmte en vele leuke zondagen. En als allerlaatste maar allerbelangrijkste: Karolien, bedankt voor de beste verjaardagscadeau van mijn leven. *You make my every day.*

Jonathan Schrauwen
Gent, 20 Januari 2009

Contents

Nederlandstalige Samenvatting

Nanofotonica en gefocusseerde ionenbundels

Fotonica is de wetenschap die het maken, geleiden, veranderen en opvangen van licht behandelt. Dit jonge onderzoeksdomein vindt zijn oorsprong bij de uitvinding van de eerste laser, een vijftigtal jaar geleden. Enkele tientallen jaren later werden optische vezels ontwikkeld met lage propagatieverliezen, in het bijzonder voor golflengtes in het nabije infrarood. Sindsdien werd licht wijdverspreid als be meest geschikte drager van informatie voor communicatie over lange afstand.

Er is sterke vraag naar meer bandbreedte zowel voor lange afstandscommunicatie, waar bandbreedteverslindende internetdiensten meer aandacht krijgen, als voor informatieoverdracht over korte afstanden, waar bijvoorbeeld processoren met meerdere kernen of grote datacentra meer datatrafiek vereisen. Deze evoluties hebben geleid tot vooruitgang in het gebeid van optische informatieoverdracht vanwege de inherente hoge bandbreedte ervan. Enkele belangrijke thema's zijn de vermindering van het aantal omvormingen tussen elektrische en optische signalen, en de integratie van optische functies op kleinschalige geïntegreerde circuits. Alhoewel historisch gezien veel van het onderzoek in de fotonica gedreven word door telecommunicatie zijn er toch een heel aantal andere vakgebieden bij betrokken. Zo worden bijvoorbeeld lasers gebruikt voor medische toepassingen, worden biomoleculen gemeten met behulp van fluorescentie, worden glasvezels gebruikt voor de stabiliteitscontrole van grote constructies, enz.

Een van de manieren om meer optische functies op een enkel fotonisch IC (geïntegreerd circuit) onder te brengen is de miniaturisatie van de golfgeleiders tot de orde van micrometers door een groter brekingsindexcontrast te gebruiken. Dit is mogelijk in halfgeleider-

materialen zoals Si of InP. Voor de fabricage van deze *nanofotonische* structuren kunnen technologieën uit de micro-elektronica gebruikt worden, zoals optische lithografie of elektronenbundellithografie. De flexibiliteit van deze technieken is echter beperkt; alternatieve technieken zijn daarom gewenst.

Door het gebruik van een gefocusseerde ionenbundel (FIB, wat staat voor *focused-ion-beam*) kunnen rechtstreeks structuren geschreven worden in alle materialen, door ze lokaal te beschieten met een gefocusseerde bundel van versnelde ionen. De botsingen die hierbij ontstaan zorgen ervoor dat er materiaal verwijderd wordt; en omdat de ionenbundel typisch fijner is dan 10 nm is de vorming van extreem kleine structuren mogelijk. FIB is daarom geschikt om op een flexibele manier nanofotonische structuren met een complexe geometrie te fabriceren of aan te passen, wat niet mogelijk is met andere technieken. Het grote nadeel van deze techniek zijn echter de grote optische verliezen (hoofdzakelijk in halfgeleiders) die veroorzaakt worden door het beschieten met versnelde ionen. Het doel van dit werk is om dit probleem op te lossen en om de toepasbaarheid van FIB voor de fabricage van nanofotonische structuren te onderzoeken.

Verlagen van de optische verliezen

Materiaalschade in halfgeleiders, zoals Si of InP, veroorzaakt grote optische verliezen. Etsen met een gefocusseerde ionenbundel veroorzaakt dit soort schade vanwege het inherente sputtermechanisme. Dit werkt als volgt: wanneer de invallende ionen het substraatmateriaal binnendringen verplaatsen ze verschillende substraatatomen vanwege opeenvolgende botsingen; sommige hiervan krijgen voldoende energie om te kunnen ontsnappen uit het substraat. Hierbij is het dus duidelijk dat niet alle verplaatste substraatatomen verwijderd worden. Het grote aantal verplaatste substraatatomen in de nabijheid van de geëtste put beschadigen de kristalstructuur van de halfgeleider en veroorzaken daardoor grote optische verliezen.

Een aantal technieken kunnen dit probleem mogelijk oplossen. Een eerste voorbeeld is het gebruik van chemische etsversnellers: door specifieke chemische elementen aan de ionenbotsing toe te voegen wordt het verwijderen van substraatatomen vergemakkelijkt. In dit werk hebben we voor het eerst gedemonstreerd dan de optische verliezen, zowel in Si als in InP, sterk kunnen verminderd worden door gebruik te maken van de combinatie van chemische versnelling

en opeenvolgend een thermische behandeling. Een tweede methode is om het beschadigde halfgeleiderkristal te bakken op hoge temperatuur (∼1000°C) en zo onzuiverheden te verwijderen en de kristalstructuur te herstellen. Een derde aanpak die we onderzocht hebben is de volledige verwijdering van de beschadigde laag materiaal door *nat* chemisch etsen of *droog* plasma etsen.

Fabricage van componenten

Om de toepasbaarheid van FIB voor de fabricage van componenten te beoordelen hebben we eerst een bestaande structuur gekopieerd: een verticale roosterkoppelaar om het licht tussen een optische vezel en een silicium IC te koppelen. Deze component bestaat uit een diffractierooster dat in een brede silicium golfgeleider wordt aangebracht. We hebben een dunne laag alumina gebruikt om het silicium te beschermen op plaatsen waar geen rooster moest geëtst worden, en hebben het recept voor vermindering van de verliezen toegepast met jodium etsversnelling en opeenvolgende thermische behandeling. Op deze manier hebben we gedemonstreerd dan het FIB geëtste rooster dezelfde hoeveelheid optisch vermogen koppelt tussen glasvezel en silicium optisch IC als diffractieroosters die met standaard technieken vervaardigd werden.

In een tweede stap hebben we de flexibiliteit van FIB gebruikt om componenten te ontwerpen en fabriceren die niet, of nog niet, met conventionele technieken kunnen gemaakt worden. Een eerste voorbeeld is een schuine roosterkoppelaar. Deze component heeft dezelfde functie als de gewone roosterkoppelaar die net vermeld werd, maar koppelt meer optisch vermogen tussen glasvezel en optisch circuit dankzij een aangepast ontwerp. Een schuine roosterkoppelaar bestaan uit roostertanden die schuin opgesteld staan en smaller zijn dan bij gewone koppelaars (wat niet mogelijk is met de huidige standaard technieken). We hebben een dergelijke koppelaar ontworpen en gemaakt en hebben zo de toepasbaarheid aangetoond van het verlies verminderingsmechanisme voor het maken van prototypes van componenten met hogere complexiteit en met betere prestaties dan de huidige standaardtechnologieën. Een andere component die op een analoge manier gemaakt werd is een sleufringresonator.

Een verschillende aanpak om de mogelijkheid van FIB om complexe driedimensionale structuren te maken te benutten, terwijl de problemen van materiaalschade vermeden worden, is door FIB te

gebruiken om inverse vormen te etsen in een stempel, en deze te kopiëren in een ander materaal door te drukken. Deze aanpak hebben we met succes gebruikt of refractieve polymeerwiggen te maken bovenop roosterkoppelaars. Dit laat de aanhechting van lasers met een verticale caviteit toe op silicium fotonische IC's.

Afstemmen

Een andere toepassing van een flexibele directe etsmethode als FIB is om kleine aanpassingen te doen aan bestaande componenten om ze zo af te stemmen. Het afstemmen van nanofotonische componenten is noodzakelijk vanwege hun extreme gevoeligheid voor fabricage-imperfecties. De conventionele technieken die typisch gebruikt worden voor micro-elektronische componenten, waar imperfecties tot 10% getolereerd worden, zijn niet voldoende nauwkeurig voor de fabricage van heel aantal nanofotonische componenten. Zo kunnen bijvoorbeeld filters niet op een voldoende reproduceerbare manier gamaakt worden. Dit komt omdat in praktijk een fabricagefout van 1 nm in de breedte van een golfgeleider (0.5 μm), een typische verschuiving van de resonantiegolflengte van 1 nm veroorzaakt. Dit is onaanvaardbaar voor de meeste toepassingen.

In dit werk hebben we FIB etsen toegepast om silicium ringresonatoren af te stemmen. Hierbij maten we echter een significante verslechtering van de optische eigenschappen vanwege de geïnduceerde materiaalverliezen. Daarom hebben we onderzoek verricht naar een alternatieve techniek om circuits af te stemmen: door te bestralen met een elektronenbundel. Deze techniek hebben we met succes gebruikt om de resonantiegolflengte van een silicium ringresonator af te stemmen over verschillende nanometers (wat voldoende is om fabricagefouten te compenseren) zonder achteruitgang van de filterkarakteristieken.

Besluit

Het gepresenteerde werk bestudeert de optische verliezen van FIB geëtste nanofotonische structuren in Si en InP. De verliezen kunnen sterk gereduceerd worden door gebruik te maken van jodium etsversnelling en opeenvolgend een thermische behandeling. Deze techniek is compatibel met aanpassingen aan afgewerkte componenten. We hebben de fabricage van verschillende prototypes van silicium nanoftonische componenten gedemonstreerd. Daarenboven

hebben we de toepasbaarheid gedemonstreerd van FIB voor de fabricage van grote volumes: eerst als een techniek om afgewerkte componenten af te stemmen, vervolgens om stempels te maken die kunnen gekopieerd worden door drukken. Om te besluiten toont dit werk de toepasbaarheid aan van FIB zowel om prototypes van nanofotonische componenten te maken als voor fabricage in grote volumes ervan.

English Summary

Focused ion beam and nanophotonics

Photonics is the science of making, guiding, altering and detecting light. This recent field of research came to life about a half century ago with the invention of lasers. Some decades later glass fibers with low optical losses in the near infrared wavelength range were developed. Since then light has become widely spread as the best suitable information carrier for long distance communications.

The demand for bandwidth rises both for long distance communications, where high bandwidth internet services gain interest, and for short distance information transport, where for example multicore processors or large data centers require ever increasing data traffic. These evolutions have ignited advancements in the field of optical data transport due to its inherent broadband capability. Some of the prominent themes are the reduction of conversions between electronic and optical signals, and the integration of optical functions on small scale integrated circuits. Although telecommunications have historically driven much of the research in photonics, many other fields of science have been involved. For example the use of lasers for medical applications, of fluorescence for the sensing of bio molecules, of fibers for stability monitoring of constructions, and many, many more.

One of the approaches in reaching more optical functions on a single integrated circuit is the miniaturization of optical waveguides below the range of micrometers by increasing the refractive index contrast. This can be obtained in semiconductor materials such as silicon or indium phosphide. For the fabrication of these *nanophotonic* structures, fabrication technologies from the micro electronics industry such as optical or electron beam lithography can be used. However, the flexibility of these techniques is limited and an alternative would be desirable.

Focused-ion-beam (FIB) is a direct etch technique that allows to directly write structures in any material by locally bombarding it with a focused beam of accelerated ions. This bombardment causes removal of the material, and thanks to the beam size of below 10 nm extremely small structures can be fabricated. FIB is therefore well suited to flexibly fabricate or modify nanophotonic structures with complex geometries, which is impossible with any other technique. However, the major inconvenience of this approach is the optical losses that are induced (specifically in semiconductors) by the ion bombardment. The goal of this work is to overcome this hurdle and to demonstrate the applicability of FIB for the fabrication of nanophotonic devices.

Reducing the optical losses

Material damage in semiconductors, such as silicon and indium phosphide, leads to high optical absorption. Etching with FIB creates such material damage because of the inherent sputter bombardment process that works as follows: As the impinging ions penetrate in the substrate material they move several substrate atoms around; some of these gain enough momentum to escape from the substrate. It is clear that not all the affected substrate atoms are sputtered. The large number of displaced substrate atoms in the vicinity of the etch crater deteriorate the crystal lattice of the semiconductor and cause large optical losses.

A number of techniques can potentially alleviate this problem. A first one is the use of chemical etch enhancement: by adding specific chemical elements to the ion collision the removal of substrate atoms can be facilitated. In this work we have demonstrated for the first time that the optical losses, both in Si and InP, greatly decrease by using a combination of chemical gas enhancement and a subsequent thermal treatment. A second approach is high temperature annealing ($\sim$1000°C) of the damaged semiconductor crystal to remove impurities and recover the crystal structure. A third approach that was investigated is the complete removal of the damaged material by *wet* chemical etching or *dry* plasma etching.

Fabrication of devices

To assess the applicability of FIB fabrication of photonic devices we have first duplicated an existing structure: a vertical fiber coupler

for coupling light between a fiber and a silicon integrated circuit. This device consists of a diffractive grating that is etched in the top surface of a broad waveguide. We have used a thin alumina layer to protect the silicon circuit from FIB irradiation in the regions where no grating is etched, and we have applied the loss reducing etch recipe with iodine etch enhancement and subsequent thermal treatment. In this way we have demonstrated that a FIB etched grating couples the same amount of power from fiber to silicon circuit as gratings etched with standard techniques.

In a next step we have used the flexibility of FIB to design and fabricate devices that can not, or not yet, be fabricated with standard techniques. A first example is a slanted grating coupler. This device has the same functionality as a regular grating coupler that was just mentioned, but couples more optical power between fiber and optical circuit thanks to a different design. In a slanted grating coupler the grating grooves are placed under an angle and are much thinner than in a regular grating coupler (which is impossible to achieve with current standard fabrication techniques). We have designed and fabricated such a grating coupler and have therefore demonstrated the applicability of the loss reduction mechanism to the prototyping of a device with higher complexity and better functionality than current standard technology. Another device that was successfully fabricated with a similar fabrication process is a slot ring resonator.

A different approach to profit from the ability of FIB to make complex three dimensional structures, yet avoid the difficulties of material damage, is to use FIB to fabricate inverse shapes into a mold and copy these into another material by imprinting. This approach was successfully pursued to define refractive polymer wedges on top of grating couplers that enable flip-chip bonding of vertical cavity lasers on top of a silicon photonic integrated circuit.

Trimming

Another application of a flexible direct write technique such as FIB is the modification of existing devices for trimming purposes. Trimming of nanophotonic devices is necessary due to their extreme sensitivity to fabrication imperfections. Conventional fabrication techniques, typically used for micro electronics where fabrication imperfections of 10% can be tolerated, are not sufficiently accurate for the reproducible fabrication of many optical functions such as fil-

ters. For example, an error of 1 nm in the width (0.5 μm) of a silicon ring resonator causes a typical resonance wavelength shift of 1 nm, which is unacceptable for many applications.

In this work we have adopted FIB etching for the trimming of silicon ring resonators, but we have measured considerable deterioration of device properties due to the induced material damage. We have therefore investigated an alternative trimming technique based on electron beam induced stress in silicon. This technique was successfully used to trim the resonance wavelength of silicon ring resonators over several nanometers (sufficient to correct for fabrication imperfections) without deterioration of the filter characteristics.

Conclusions

The presented work has studied the optical losses of FIB etched structures in Si and InP nanophotonic devices. The losses can greatly be reduced by using iodine etch enhancement and subsequent baking; a technique that is compatible with the modification of finished devices. We have demonstrated the prototyping of several silicon nanophotonic devices. Furthermore we have presented the applicability of FIB for high volume fabrication: first as a technique to trim finished devices, than as a technique to pattern molds that can be replicated by imprint. To conclude this work proves the applicability of FIB for both prototyping and volume manufacturing of nanophotonic devices.

List of Abbreviations

BCA binary collision approximation

CMOS complementary metal oxide semiconductor

DFB distributed feedback

DBR distributed Bragg reflector

EBID electron beam induced deposition

EBSD electron backscatter diffraction

EDX energy dispersive X-ray spectroscopy

FDTD finite difference time domain

FIB focused-ion-beam

IBID ion beam induced deposition

ICP inductively coupled plasma

LED light emitting diode

LMIS liquid metal ion source

MBE molecular beam epitaxy

RTA rapid thermal annealing

SEM scanning electron microscopy

SIM scanning ion microscopy

SIMS secondary ion mass spectroscopy

SOI silicon on insulator

SRIM Stopping and range of ions in matter

TEM transmission electron microscopy

TFA trifluoroacetamide

UV ultraviolet

VCSEL vertical cavity surface emitting laser

XPS X-ray photoelectron spectroscopy

Chapter 1

Introduction

1.1 Photonics

"Something with light probably." is usually what non-scientists answer when you ask them about this young field of research; and it is not far from the truth. Photonics is the science of making, guiding, and detecting light. The typical wavelengths of the electromagnetic radiation considered as *light* range from ultraviolet to near-infrared, i.e. typically 100-3000 nm. The application of this light for telecommunications, sensing, medicine, display technology and optical computing form the subject of photonics. Historically the invention of the first lasers in the 1960s marks the beginning of many emerging applications of light, beyond lighting. The technological development of a low-loss transmission medium - glass fiber - in the 1980s entailed the first widespread use of light as a means of information carrier. Combine this with the success of semiconductor lasers and detectors to convert the information between the electrical and optical domain, and an unbeaten backbone for the telecommunication network emerges. Photons are presently still the dominant long distance information carriers. Many advancements have been made on the amount of data transported on a single fiber and the speed of modulators and detectors. However, the information network has also become increasingly complex and loaded, requiring more switching and routing. Therefore limiting the number of conversions between an electrical and optical signal has become the primary target in making the network faster and less energy consuming. This demands for all-optical circuits with functions such as

filtering, splitting, and memory; ideally brought together on a single chip by photonic integration.

1.2 Integrated photonics and nanophotonics

Photonic integration - the integration of guiding and other functions on a planar chip - has been the approach of interest for many years. This approach was ignited by the success of electronic integration, which has dramatically increased the density of electronic functions and consequently lowered the cost. For photonics, platforms in various material systems have been used both for research purposes and for industrial deployment. These include glass, silica-on-silicon, silicon-on-insulator (SOI), III-V semiconductors, etc. The important criteria include transmission loss of waveguides, the refractive index contrast, and the possibility to include active functions such as sources and detectors. Glass based circuits feature low losses, but due to the limited index contrast (typically provided by impurities in the silica matrix) waveguide bend radii and waveguide pitches must be rather large, leading to circuits of several square centimeters in size. Furthermore it is not straightforward to include active functions in these circuits. Semiconductor material (e.g. silicon or indium phosphide) has a larger refractive index ($\sim$3.5) as compared to glass ($\sim$1.5) and can therefore be used for light guiding structures with much higher index contrast, and accordingly smaller mode volumes. These smaller modes can be guided through much shorter bends and allow for much denser integration. However, these smaller modes (100-500 nm) are also much more sensitive to fabrication imperfections, which makes the fabrication increasingly challenging. Typically a fabrication imperfection of 1 nm causes a wavelength shift of 1 nm, which authorizes the use of the name *nanophotonics* for photonics in high index contrast material systems.

III-V semiconductor platforms, such as InP or GaAs based material systems, are inherently well suited for active functions because of their direct bandgap that enables efficient opto-electronic conversions. However, III-V substrates as well as III-V processing remain expensive , which hinders massive deployment. Furthermore, the incorporation of high refractive index contrast necessitates the use of membranes, which greatly increases the cost since no industrial III-V wafer-splicing-and-bonding techniques are available today. On the contrary, the silicon-on-insulator (SOI) platform doesn't suffer these inconveniences as substrates with a thin silicon layer on top of an

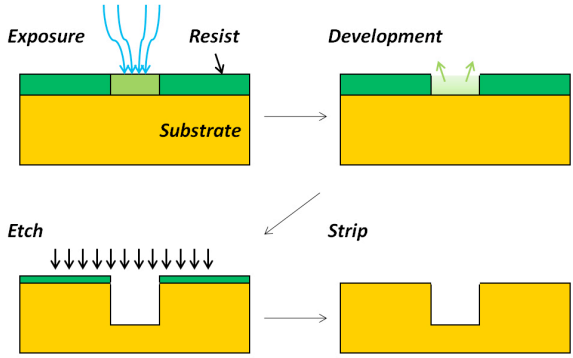

Figure 1.1: Basic steps of the most common fabrication scheme for structures down to tens of nanometers.

oxide buffer layer are commercially available at relatively low cost. Furthermore, for the fabrication of devices one can rely on large and reliable manufacturing facilities used in the micro-electronics industry (currently fabricating on wafer sizes up to 300 mm), and the integration of optic and electronic circuits is possible. This enables high volume fabrication of densely integrated photonic chips with various functions such as waveguides, filters and modulators [1, 2, 3]. However, since silicon is an indirect bandgap semiconductor, efficient and compact silicon lasers have not been demonstrated so far [4]. Recently this problem has been addressed both by academic and industrial researchers by adoption of slightly more complex fabrication schemes such as glueing or bonding of finished III-V devices or un-patterned III-V films (heterogeneous integration) [5, 6, 7].

1.3 Fabrication technologies

A typical fabrication scheme for structures with dimensions down to tens of nanometers uses lithography for pattern definition into a radiation sensitive layer, and etching techniques to transfer the layer into a substrate material (depicted in Fig. 1.1). This paragraph gives a brief overview of the most commonly used techniques. The arguments used in this paragraph hold for the fabrication of microstructures in general and not only for nanophotonic fabrication. We will discuss the basic limitations of resist based techniques.

Optical and electron beam lithography

The most commonly used patterning technology for integrated circuits (both electronic and photonic) on planar substrates is lithography. This technique uses a radiation-sensitive material, i.e. a resist. A pattern is defined in the resist layer either by a focused beam of radiation or by selective illumination using a mask. The first technique usually adopts a beam of electrons (electron beam lithography) and is serial, meaning that each feature needs to be written sequentially, thus requiring a time that scales linearly with the number of structures. This makes the technique not suitable for high volume manufacturing of devices. Illumination using a shading mask, either by pressing the mask onto the substrate (contact lithography) or by projecting an image of the mask onto the resist layer, is a parallel technique suited for mass fabrication since its speed is in principle independent of the number of circuits. However, it requires an expensive mask and the cost for development of new circuits is high. Therefore, serial and parallel lithography go hand in hand when it comes to the development and high volume fabrication of integrated circuits: serial techniques are used for device prototyping and mask fabrication, and optical lithography is used for high-volume fabrication of chips.

However, resist based processes have a number of limitations. To discuss these in more detail we will divide the process flow of optical or electron beam lithography in the following 3 steps:

1. radiation propagation through the optical system,

2. radiation-induced changes in the resist,

3. development.

Each of these steps places its limits on the smallest obtainable features; furthermore they each need extensive optimization.

As an example, the size of the smallest feature after the first step is limited by the fundamental properties of the radiation source. For optical lithography systems the wavelength of the source limits the resolution due to diffraction (step 1), and thus constrains the obtainable degree of integration. This has caused a shift in recent years from visible light sources to deep ultraviolet (UV) (248 nm and 193 nm) excimer lasers with substrates immersed in liquids to increase the numerical aperture and consequently improve the resolution of the imaging system. The evolution is currently ongoing

with efforts to exploit the extreme UV (13.5 nm) and X-ray ($< 1\ nm$) regions of the electromagnetic spectrum.

For electron beam lithography, with a beam energy of typically 30 to 100 keV, the particle wavelength of about 4 pm is not the limiting factor; nor is the typical beam size (1 nm) of electron beam systems. However, the resolution is constrained by the mechanism of energy loss of the electrons in the resist, since it occurs through a large number of binary collisions that alter the path of the electron and generate secondary electrons. Therefore the irradiated spot under the resist surface is much larger than the beam size due to this electron spread (effective beam broadening). Increasing the electron energy and decreasing the resist thickness minimize this effect, but the formation of secondary electrons can not be avoided. A similar beam broadening comes into the picture for extreme UV and X-ray optical lithography when a feature size below 50 nm is targeted.

Subsequently the properties of the resist are altered by the impinging radiation (step 2) through a chemical reaction that makes the resist soluble or insoluble in a suitable developer. For adequate pattern definition, which is inherently a binary process, a sufficiently nonlinear response of the resist is required. This means that the binary condition "soluble" versus "insoluble" in developer (after irradiation) has a sharp step in function of the illumination dose. An ideally nonlinear response function is a step function, which allows the definition of sharp edges. The pattern is then defined by development (step 3), i.e. a selective removal of material, either the radiation softened material (positive process) or the non-hardened material (negative process). This process is usually conducted in a wet chemical etch bath. The precise development parameters, such as chemical composition, temperature and duration influence the final resist pattern when the resist is not ideally nonlinear, and need careful optimization.

It can be concluded from these three steps that fundamental physical interactions and the inherent molecular properties of the resist are the resolution-limiting factors of a standard lithography based process flow.

Imprint lithography

To circumvent these limitations an alternative approach was developed to define a pattern in a resist layer: by using a mechanical deformation. This can be done by pressing a mold into the resist when it is still liquid, and then solidifying, or curing, the layer by heat or

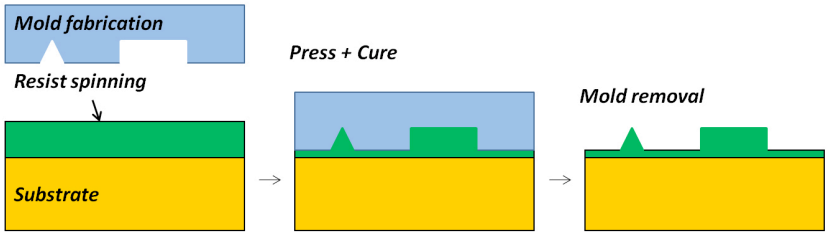

Figure 1.2: Schematic overview of the different steps of imprint lithography.

radiation (see Fig. 1.2). This novel approach does not rely on the selective radiative changes in the molecular structure of the resist, but rather on the purely mechanical deformation of the viscous liquid resist. The resolution and quality of the copied shapes is therefore unprecedented.

By properly controlling the adhesion of the mold to the resist, the mold can be removed and the patterns are transferred to the resist layer. The greatest advantage of this technique is its simplicity: there is no need for expensive lasers or optical systems. Furthermore, the technique is fit for high-throughput and low cost fabrication of high resolution structures. And the replication process is not limited to planar structures; it can copy 3D structures from the mold into the resist layer.

However, as depicted in Fig. 1.2, the imprint process leaves behind a thin resist layer, also called the residual layer, which has to be removed to transfer the structures into the substrate material. This process of residual layer removal is often performed by plasma etching and needs careful optimization; it can be compared to the development step in optical lithography. Another concern is wear of the mold that is easily damaged by the repeated mechanical contact. Furthermore, imprint lithography does not avoid the limitations of etch processes for pattern transfer into the substrate.

Etching techniques

Once the pattern has been defined in the resist (by either kind of lithography) it still has to be copied into the substrate material. This requires a subsequent etch step, which can be performed in a *wet* etch bath or a *dry* plasma chamber. Wet etching is usually isotropic, meaning that it etches the substrate equally fast in all directions.

This causes rounding of edges and under-etch, and greatly reduces the resolution of the transferred pattern. Dry etching is performed in a plasma; the most common techniques are reactive ion etching (RIE) and inductively coupled plasma etching (ICP). In an RIE reactor a plasma is generated above the substrate by placing it on one of the plates of a capacitor that is powered at radio frequency. The ions are then accelerated towards the substrate by applying a constant bias voltage between the capacitor plates. For ICP etching the generation of the plasma is uncoupled from the sample surface; it is done inside a solenoid that inductively couples its power into the plasma. This allows for more control in the energy and the amount of ions bombarding the sample surface. The ion species inside the plasma are chosen according to the desired chemical reaction with the substrate material and the undesired reaction with the resist material. The ratio between these is called the etch selectivity, and it determines the maximum substrate etch depth for a given resist thickness. Since most resist layers are polymers that are usually much softer that the substrate material it is often difficult to find etch parameters that allow etching with high selectivity. This causes resist erosion during the etch process, which can lead to angled sidewalls and roughness. It is clear that the etch step has a large number of degrees of freedom and needs careful optimization. Furthermore, due to the limited etch selectivity, pattern quality is often deteriorated and the resolution is therefore limited.

Conclusion

It can be concluded that from a point of view of resolution and processing simplicity, a direct interaction between the pattern-defining-radiation and the substrate material would be desirable. This would allow the fabrication of devices with better resolution because it eliminates the radiation sensitive layer. Furthermore, as an extra development and etching step are no longer required the process flow can be significantly simplified.

1.4 Focused ion beam and nanophotonics

Focused-ion-beam technology is a technique that allows such direct interaction with the substrate material. It uses a finely focused beam of accelerated ions to locally sputter a material. Fig. 1.3 gives a schematic overview of the mechanisms and effects that play an im-

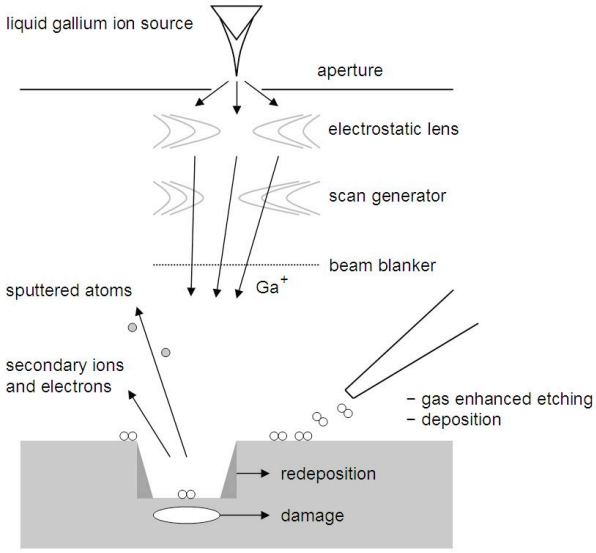

Figure 1.3: Schematic overview of FIB etching. The indicated mechanisms will be discussed in more detail later.

portant role in FIB technology; they will be discussed in more detail in Chapter 2. FIB was mainly developed in the late 1970s and the early 1980s, primarily enabled by the development of good ion sources. The driving force behind this progress was failure analysis of micro-electronic devices. In the beginning focused-ion-beam (FIB) was used as a miniaturized drill or milling machine with beam sizes of around one micron. It was the only available technique to drill small holes in electronic chips and reveal buried defects. The technique is particularly interesting because ion bombardment with a focused ion beam allows not only the local sputtering of material, but also the imaging by secondary electron emission (similar to electron microscopy).

In later years the advancements in particle optics and ion source technology have pushed the ion beam size down to the nanometer range. Furthermore, systems with both an ion and an electron beam have recently become commercially available. These enable in situ inspection through high resolution scanning electron microscopy (SEM) of the FIB etched structures. These systems are therefore extremely flexible nanofabrication tools that have been adopted for new applications such as the three dimensional *slice and view* microscopy [8].

The properties of FIB make it an attractive alternative for the current fabrication technologies of nanophotonic structures. In the

following two paragraphs we give a detailed overview of the advantages and applications of FIB for photonic devices. A number of these applications were investigated previously, but a number of important questions regarding the applicability of FIB for *nano*photonics remain. To answer these questions is the goal of this work, as will be discussed in the next section.

1.4.1 Advantages

Direct write

Patterning with FIB consists of hitting a material locally with high energy ions; in most commercial systems these are gallium ions with an energy of around 30 keV, focused in a spot of typically 10 nm in size. Due to the large mass and momentum of the impinging particles they cause substrate atoms to move around as their energy dissipates in a series of collisions inside the material. This leads to localized sputtering of substrate atoms, which makes FIB a direct write technique, which does not require a resist.

Etching any material

Most of the commonly used etch processes rely for a large part on chemical reactions between substrate atoms and chemical compounds in a plasma. This makes chemically stable materials, such as diamond or gold, hard to etch. Since the fundamental process of sputtering is less dependent on the chemical composition of materials, it can be used to etch any solid material (metals, semiconductors, polymers, ceramics,...). Furthermore, charging problems on insulating materials can be circumvented by charge neutralization with electrons. Literature reports on the FIB etching of optical structures in a wide variety of materials, including diamond [9] and gold [10, 11].

Nano-patterning

Since FIB is a direct write technique, the resolution is only limited by the size of the beam and the fundamental process of ion solid interactions. It is not limited by any resist or secondary etching process, as is the case in standard lithography approaches. In current commercial systems the ion beam can be focused in a spot of about 10 nm, and this size is likely to decrease as ion beam optical systems improve [12]. FIB therefore has an unprecedented resolution

potential and can open the way to flexible fabrication of nanoscale structures.

3D patterning

FIB can be used to etch angled features such as slits and facets, and structures with more complex 3D geometry, which is not possible with standard planar etching techniques. This allows an extra degree of freedom for the design of photonic devices and can therefore open a world of new devices with increasingly complex functionality. Angled slits or facets can be made by simply tilting the substrate during the etch process. But by carefully designing the scanning algorithm, much more complex etch shapes can be achieved. For instance the angle dependence of the sputter yield and redeposition (see later), have to be taken into account in the design of suitable scanning algorithms for the etching of arbitrary 3D shapes. Simulations with several models have been proposed to predict the shape of FIB etched structures, as a function of the applied scanning algorithm. These were mostly used for the etching of curved surfaces, such as for probe tips and micro-machining tools [13, 14] and for lenses or lens molds [15, 16] (although no optical characteristics were reported). However, no inverse solving method has been presented so far. This is necessary for the rapid fabrication of arbitrary shapes. Nevertheless, the excellent agreement between simulation and experiment of the full 3D model recently presented in Ref. [17] suggests that this is within reach.

1.4.2 Applications

From these four basic advantages (direct writing of nanoscale 3D structures in any material) a number of potential applications in photonics can be derived. Some of these applications were investigated previously. However, at the onset of this work, few working nanophotonic devices had been presented.

Prototyping

As mentioned the development of new nanophotonic structures with increasing functionality requires serial fabrication techniques due to the high mask cost of deep-UV lithography. One needs prototyping technologies that enable rapid and flexible fabrication of nanophotonic components. The most common example nowadays is electron

beam lithography, which is a serial technique, too slow for the mass fabrication of large devices, but attractive as prototyping technique because of its high resolution compared to standard optical lithography. One of the inconveniences is the fact that it requires resist layers and etching with plasma etching. This slows down the optimization process and limits the designs to planar structures. FIB has a similar advantage of being a rapid and flexible technique; furthermore it is suited for the fabrication of nanometer scale structures with 3D geometry in any material. In addition, when a machine with both electron and ion beam is used, one can directly inspect the fabricated device, which greatly accelerates the process optimization. Therefore FIB is potentially well suited for the prototyping of nanophotonic structures.

Device modifications - Trimming

Although resist-based techniques can in principle be overlayed on pre-existing structures (i.e. patterning on pre-existing patterns), this is only possible when the underlying structures are planarized, i.e. with a flat top surface. This is required to allow reproducible spinning of the resist layer. On the contrary, with a direct write technique, one can modify existing non-planar structures. One can for instance etch gratings in the sidewall of existing ridge waveguides or etch slots in ring resonators without requiring planarization. Therefore FIB is a promising technique to perform device modifications with unprecedented resolution. This is of specific interest if one combines the high-volume fabrication capability of a parallel technology such as deep-UV lithography, with the high-resolution capability of FIB. FIB can be used to make small - and therefore rapid - high-resolution modifications to pre-fabricated devices. This is for example necessary for the trimming of devices with slightly incorrect dimensions, and for etching small features that are beyond the resolution capabilities of the parallel fabrication technology. Other than for small modifications FIB can also be used to etch structures that are hard to make with other techniques, such as vertical or angled laser facets. Some examples of device modifications by FIB have been demonstrated in literature: Distributed Feedback gratings in InP ridge waveguides [18], laser facets in GaN [19], laser facets and Distributed Bragg Reflectors in AlGaInP [20], photonic crystal cavity mirrors in InP [21], plasmonic gratings on laser facets to reduce beam divergence [22], gratings in silicon rib waveguides [23] and gratings on VCSEL's to improve modal behavior [24]. However,

a deterioration of the optical properties of the devices was always observed.

Imprint mask fabrication

Imprint lithography offers the possibility to reproduce 3D structures from a mold in a parallel way, with a resolution smaller than 10 nm. FIB can be used to etch structures with 3D geometry, but only serially and thus more slowly. Therefore the combination of imprint lithography and FIB is complementary: FIB can be used to etch nanometer sized structures with 3D geometry in a mold that is replicated many times by imprint lithography. Since FIB is one of the only techniques that allows the flexible fabrication of nanoscale 3D shapes, it enables the high volume fabrication of these structures through imprint. This is important for nanophotonics because it opens the door to high volume production of structures with more design flexibility and accordingly more complex functionality.

1.5 Goal of this work

So far we have discussed the existing literature on the application of FIB in photonics, and we have discussed the potential future applications of FIB for the fabrication of nanophotonic structures. From this discussion we can conclude that a number of devices was fabricated with FIB, however, a deterioration of the optical properties was always observed. In many examples the deterioration is so pronounced that no optical characteristics were reported.

The primary questions that therefore arise are what mechanisms cause this deterioration of the optical properties and whether they can be avoided. The goal of this work is to answer these questions and to adopt FIB for the fabrication and modification of nanophotonic devices. Let us discuss this in more detail.

Reducing material damage in Si and InP

It was discussed in literature that FIB etching leads not only to material removal but also to implantation and material damage. This leads, particularly in semiconductors, to optical losses. Literature reports on the post-processing of III-V devices with FIB, such as Distributed Feedback gratings in InP ridge waveguides [18], laser facets in GaN [19], Distributed Bragg Reflectors in InP [20] and photonic crystal cavity mirrors in InP [21]. In all these examples the volume of

the optical mode is big compared to the etched region. A degradation of the optical properties is often reported, but can be overcome by pumping in the undamaged regions. However, in silicon one is often limited to passive devices, and wants to exploit very tight confinement and small modal volumes. When a silicon device with its optical mode close to the focused-ion-beam etched region is fabricated, large optical losses are observed [23, 25]. To adopt FIB fabrication for nanophotonic structures, the challenge remains to reduce the optical losses that are generated by FIB etching, both in silicon and in III-V semiconductors.

Prototyping of nanophotonic devices

FIB was used for the fabrication of prototypes of several devices, such as mode controlling VCSEL mirrors [24, 26], Bragg reflectors in silicon rib waveguides [23], grating couplers in SiN [27], micropillars in GaN [28], photonic crystal structures in lithium niobate [29] and chalcogenide glass [30] and slanted rib waveguide walls for polarization conversion [31]. However, prototyping of nanophotonic devices in silicon or III-V semiconductors remains a challenge due to the required fabrication precision (sub 100 nm features, vertical sidewall angle, etc.) and the discussed optical losses. The goal of this work is to investigate the potential and the limitations of FIB prototyping. This includes a precise characterization of the FIB induced material damage and how it relates to device performance. Furthermore it includes the exploration of the ultimate patterning potential of current systems and the optimization of fabrication procedures such as alignment.

Trimming of nanophotonic devices

We have discussed the potential of FIB to do device modifications and trimming. The goal of this work is to investigate whether sufficiently low material deterioration can be obtained for industrial applicability of FIB trimming. Furthermore it is the goal to explore the possibility of *live* trimming, i.e. trimming a device while its transmission is monitored.

1.6 Achievements and Overview

The remainder of this work is divided in 6 chapters. In Chapter 2 we present the basics of FIB technology. Then we will discuss the reduc-

tion of the optical losses in silicon nanophotonic structures. We have performed experiments with gas enhanced etching and - in collaboration with Twente University (The Netherlands) in the framework of the European Network of Excellence (FP6) ePIXnet - with high temperature annealing. The results, as presented in Chapter 3, are a reduction in optical losses to practicable values. This approach is then used for the fabrication of various nanophotonic devices in Chapter 4. These include grating couplers with high efficiency and slot ring resonators. In the following chapter we investigate the feasibility of trimming with FIB and by electron beam irradiation (Chapter 5). Next we will dwell on the fabrication of 3D imprint molds with FIB in Chapter 6; by imprinting this mold we have fabricated a polymer wedge that enables flip-chip bonding of VCSELs on silicon. Finally we will investigate the FIB etching of III-V semiconductors in Chapter 7.

The work presented here was conducted in the Photonics Research Group of Ghent University - IMEC, founded and headed by Roel Baets. This group has worked on the integration of photonic devices for more than 20 years, and has closely participated in the shift to integrated photonic circuits in the silicon-on-insulator (SOI) platform.

The scientific achievements of this work have resulted in patent applications, publications in scientific journals, and contributions to conferences and workshops. We refer to Appendix A for a complete list of patents and publications.

Chapter 2

Focused-ion-beam technology

2.1 Interaction of ions with solids

2.1.1 Elastic and inelastic collisions

A collision of a particle with a solid target leads to energy and momentum loss of the impinging particle. The physical laws that govern these reactions depend on the nature of the particle (charged / neutral, light / heavy, slow / fast) and the atomic number of the target. The important particles for this work are electrons and ions. They will lose their energy in a solid by consecutive collisions with nuclei or bound electrons. Collisions with bound electrons are considered non-elastic, whereas collisions with nuclei will be elastic - billiard ball like - for particles that are not sufficiently energetic to cause nuclear reactions.

Low energy electrons (< 1 MeV) colliding with a solid will lose their energy through ionizing collisions with bound electrons. In each event they can lose at most half their energy and they are subject to large scattering angles. Every produced free electron undergoes the same kind of reaction so a collision cascade forms. These collision cascades are of importance to understand e.g. scanning electron microscopy (SEM) images.

For ions colliding with a solid target the stopping mechanisms depend strongly on the ion energy. Both elastic ion-nucleus and non-elastic ion-electron collisions occur, and the *stopping power*[1] of

[1] The average amount of energy a colliding particle loses in a material per unit length, usually measured in MeV/cm.

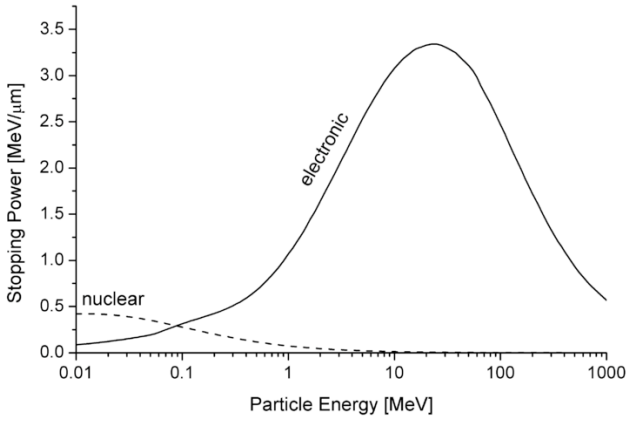

Figure 2.1: Stopping power of Al ions colliding with an Al target. The nuclear stopping power peaks typically at energies of 1 keV per nucleon, whereas the electronic stopping peaks above 100 keV per nucleon.

a certain target is the sum of both contributions. Fig. 2.1 represents the stopping power of Al ions colliding with an Al target in function of the ion energy. The nuclear stopping power peaks typically at energies of 1 keV per nucleon, whereas the electronic stopping peaks above 100 keV per nucleon. In most FIB systems the ion energy is typically in the range of 5 - 100 keV for medium mass elements so nuclear stopping is usually the dominant mechanism. This means that ions with these energies go through similar collision cascades as the low energy electrons used in SEM. Electrons only displace other electrons, whereas ions move the atoms of the target material. Some of these displaced target atoms might reach the surface with sufficiently high energy to overcome the surface energy barrier, and these atoms are ejected from the material causing the formation of a crater. Semi-empirical formulas for nuclear and electronic stopping powers of various ion species hitting different targets were determined by Sigmund [32].

The basic properties of an ion collision cascade are shown in Fig. 2.2. Energy loss will occur primarily due to the elastic collisions with target atoms, also named recoils in analogy to the terminology of Ref. [33], or can also result in the backscattering of the ions. Recoils that acquire sufficient momentum near the surface can escape

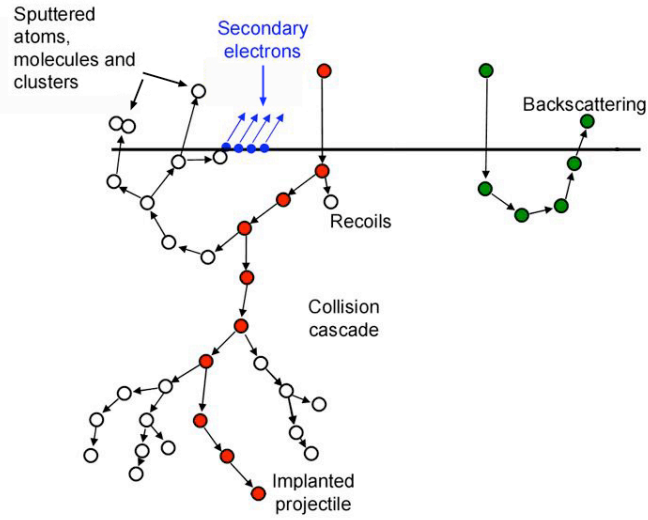

Figure 2.2: A generic ion collision cascade: the incident ion generates recoils by elastic collisions and secondary electrons by inelastic scattering.

the cascade. Inelastic collisions result in the formation of secondary electrons, X-rays and phonons.

2.1.2 Rigorous versus fast modeling

A rigorous method to calculate ion solid interactions is called molecular dynamics. All particles in the collision are part of a many-body problem interacting through a many-body potential. This function includes not only pairwise interaction of the particles, but also higher order terms. In practise however, this technique is computationally intensive and the potential function of many alloys and molecular solids is not well known. We refer to the end of this chapter for an example of a molecular dynamics calculation.

Another approach is the binary collision approximation (BCA), where the interaction is represented by a sequence of isolated collision events (Fig. 2.3). For each of these events the scattering angle is calculated from a simplified formula. This makes the method fast and convenient for simulations on a desktop computer [33]. The authors of Ref. [33] have written a freely available program: Stopping and range of ions in matter (SRIM), www.srim.org. However, the BCA only works well when the projectiles have sufficiently high energy (much higher than the binding energy of the lattice atoms) and

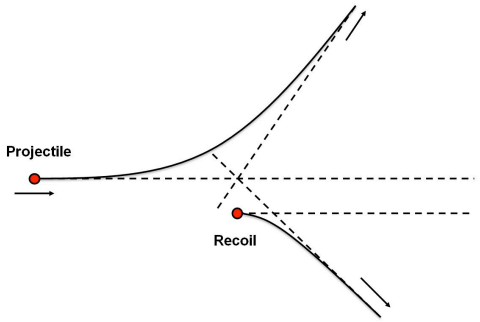

Figure 2.3: The binary collision approximation (BCA) represents the collision cascade as a sequence of isolated binary collision events.

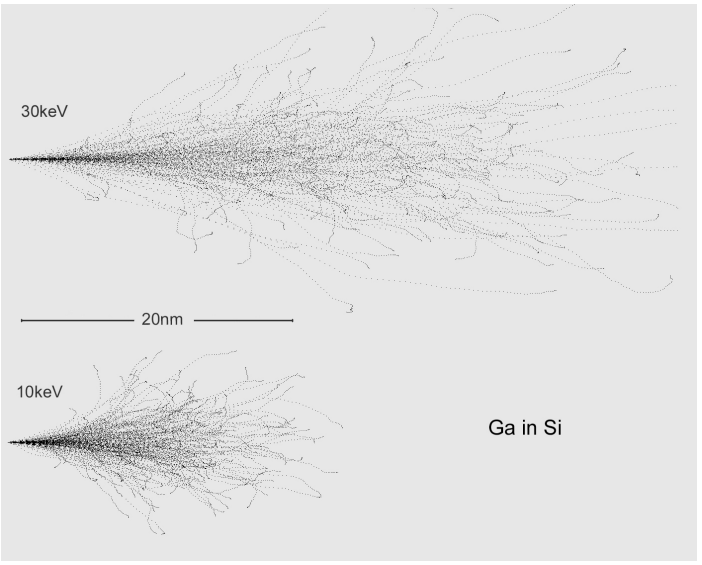

Figure 2.4: The trajectories of 10 and 30 keV gallium ions into silicon as calculated with SRIM.

when one is not interested in surface effects. Nonlinear effects such as chemical etch enhancement can not be simulated with the BCA. Fig. 2.4 shows the trajectories of gallium ions colliding with a silicon substrate calculated with SRIM.

2.1.3 Ion implantation

Ion implantation has since long been used to alter the electrical properties of semiconductors, which can be made more or less electri-

cally conductive by the incorporation of donor or acceptor dopants in the semiconductor crystal. Although this can also be achieved by diffusion of impurities into the semiconductor, implantation is a preferable approach since it allows more control over impurity depth profiles and concentrations, and it can easily be done in a selective way by using a mask layer. In practise implantation is performed by directing high energy ions (keV - MeV) onto the surface of a semiconductor. The ions are slowed down by collisions with substrate atoms and finally stopped. The depth at which the projectiles stop is called *projected range*, the traveled lateral distance is named *straggle*. Both depend on the energy of the impinging ion and on the atomic number of both projectile and target. However, this process of bombarding ions onto solids does not guarantee that the ions will act as electrical dopants in a semiconductor crystal. To achieve this, the crystal damage has to settle and the dopants need to chemically bind to their neighboring atoms. This can be obtained by high temperature annealing, where one has to take into account that impurities can diffuse in host substrates. To limit diffusion one often uses rapid thermal annealing (RTA) processes for electrical dopant activation. Nevertheless, defects often remain, especially near the end of the projected range. As depicted in Fig. 2.5, a crystal looks more transparent for certain angles of incidence. This is accompanied with deeper implantation due to ion *channeling*. In practise this effect is avoided by implanting at 7° away from the surface normal.

For semiconductor applications implantation is usually performed in wafer scale implanters that offer a variety of elements and projectile energies. Depth and dose profiles can be obtained from SRIM simulations. Typical doses are 10^{13} to 10^{16} ions/cm^2, which lead to typical impurity concentrations of 10^{17} to 10^{20} cm^{-3}.

More recently other applications of ion beam implantation have attracted much attention of the research community. High dose implantations, where the concentration of the implanted element reaches several at%, can lead to the formation of nanometer sized clusters inside the host matrix [35].

2.1.4 Sputtering

When an atom in a collision cascade reaches the surface of the target material with enough energy to overcome the surface binding energy it will move from the solid to the vapor phase. This effect is called sputtering, and is often used as material source for thin film deposition. In a typical implantation cascade only few of the

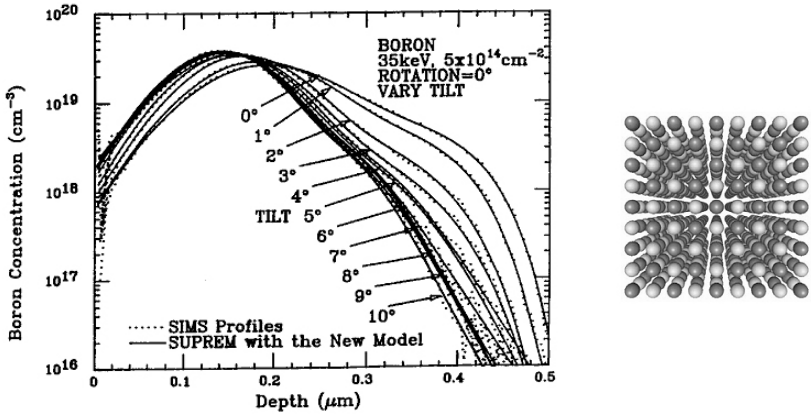

Figure 2.5: Measured and simulated depth profiles of B implanted in (100) Si (35 keV, 5 x 10^{14} cm^{-2}), where the implantation angle varies. At normal incidence the crystal seems more transparent due to crystal *channels*. Reprinted from Ref. [34].

displaced substrate atoms are sputtered, thus for low implantation doses (10^{13} to 10^{15} ions/cm^2) this effect is hardly noticeable. At higher doses the target material becomes amorphous due to an excess of material damage, and the sample swells due to the higher volume of the damaged material. At even higher doses sputtering becomes dominant and the material is noticeably sputtered. This is depicted in Fig. 2.6 for implantation with a localized beam.

The sputter yield (number of sputtered atoms per impinging ion) depends strongly on the angle of incidence of the ions. It is higher for off-normal incidence and peaks at around 80°. In this case the damage cascade spreads out near the surface and many recoils can be sputtered (Fig. 2.7). At higher incidence angles projectiles will reflect off the surface, and the sputter yield will drop consequently. The angle dependance of the sputter yield can cause the formation of roughness in certain etch conditions. For example when some initial roughness is present, the slopes will be etched faster than the valleys and plateaus, causing the formation of steeper slopes, as illustrated in Fig. 2.8. Another roughening effect is the varying sputter yields for different crystal orientations. An initially flat film with grains can show increased roughness after ion sputtering. These roughening effects are counterbalanced by redeposition, i.e. the deposition of sputtered material near the etch site, which often has a smoothening effect.

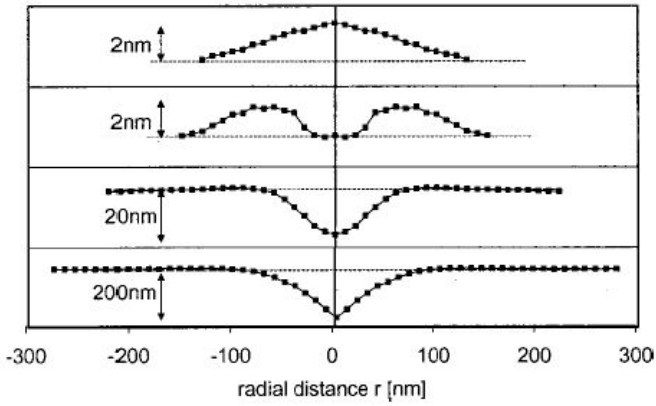

Figure 2.6: Surface of an implanted material, from medium dose (top, with a spot dose 0.025 pC 50 keV Ga ions) to high dose (bottom, with a spot dose 5 pC 50 keV Ga ions) implantation with a focused beam. First the material swells due to damage and amorphization, then sputtering becomes dominant. Reprinted from Ref. [36].

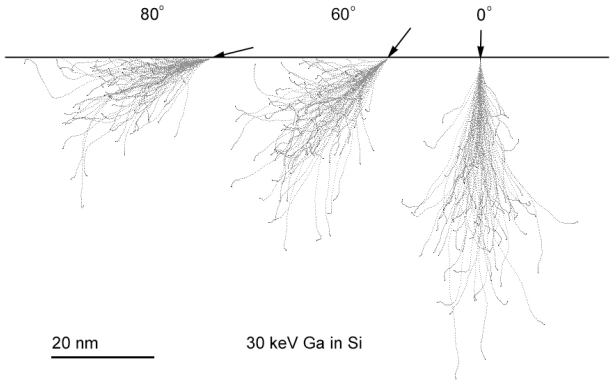

Figure 2.7: SRIM calculated trajectories of gallium ions in silicon at varying incidence angle. Grazing incidence cascades have more recoils that reach the surface with enough momentum to escape, thus a higher sputter yield.

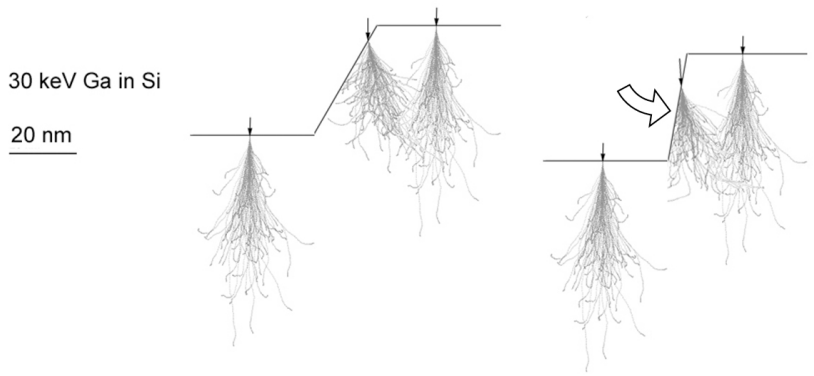

Figure 2.8: If some initial roughness is present, the slopes will erode faster than the valleys and plateaus, giving rise to steeper slopes and more roughness.

Just as the projected range and the straggle strongly depend on the atomic numbers of projectile and target, the sputter yield depends on it as well. Fig. 2.9 shows that the sputter yield for impinging 400 eV Ar ions varies more than one order of magnitude over the periodic table. More generally the sputter yield depends on the nuclear properties of projectile and target, on the binging energy of the target material, and on the energy of the impinging particle. These dependencies were summarized in semi-empirical formulas [37].

The effect of sputtering by ion bombardment causes removal of substrate and implanted atoms. At low dose implantation the concentration depth profile shows a peak inside the target material and a lower concentration near the surface. This means that the removal rate of implanted atoms initially rises as the dose increases and as the surface depression reaches this peak depth. Eventually a steady state will form where the rate of ion implantation equals the removal rate of the implanted species. The depth concentration in this case typically shows a peak at the surface and falls of over a distance comparable to the initial ion range. This steady state surface concentration can relatively easily be obtained.

The maximum concentration that can be reached by ion implantation depends greatly on the sputtering yield. Consider an ion species A that is implanted into target species B. Let us represent the volume concentrations of both species by N_A and N_B and the sputtered flux of both species by J_A and J_B. Then we have

$$J_B/J_A = r(N_B/N_A), \tag{2.1}$$

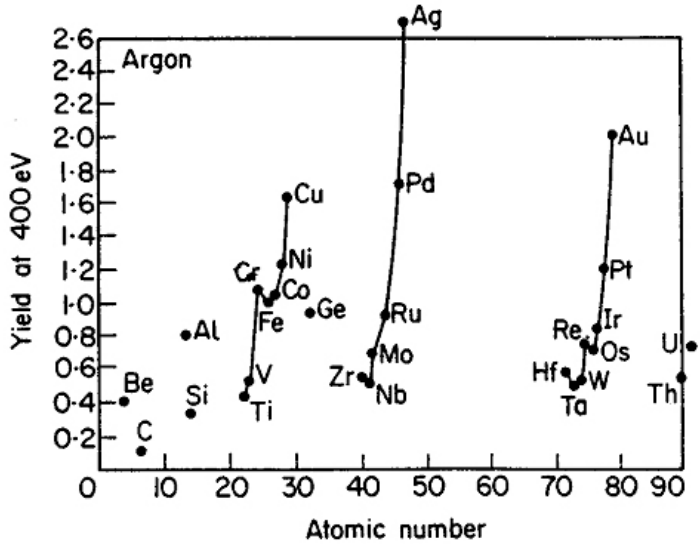

Figure 2.9: Sputter yield (i.e. number of ejected atoms per incident ion) for various targets by 400 eV Ar ions, reprinted from Ref. [38]. The sputter yield varies more than one order of magnitude over the periodic table.

where r is the ratio of the sputter yield for both species. Now define the flux of incident A ions as J_i and the total sputter yield as Y, the number of removed atoms per incident ion. We can then write

$$J_A + J_B = Y J_i. \tag{2.2}$$

When an equilibrium condition is reached (steady state) the rate of removal of A atoms equals the rate of replenishing, thus

$$J_A = J_i, \tag{2.3}$$

which yields

$$J_B = J_A(Y - 1). \tag{2.4}$$

By substitution using (2.1) we obtain

$$\frac{N_A}{N_B} = \frac{r}{Y - 1}. \tag{2.5}$$

This is the steady state surface composition. Note that the this is roughly inversely proportional to the total etch yield, which means that impurity concentrations are lower in rapidly sputtered targets.

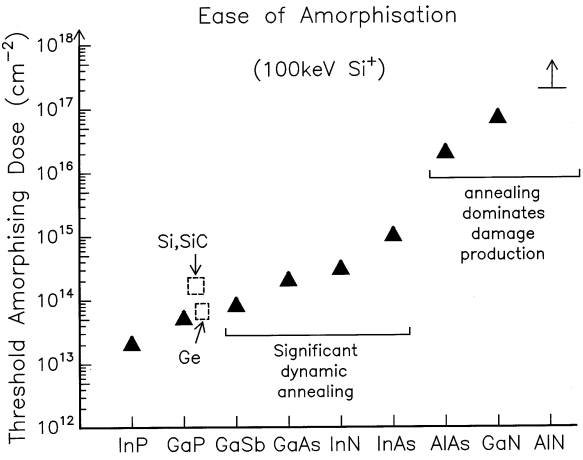

Figure 2.10: Estimation of the threshold dose for amorphization of various semiconductors, for 100 keV silicon implantation at room temperature. Reprinted from [39].

2.1.5 Damage

When an ion hits a solid a collision cascade forms, creating a track of damage through the material. This cascade takes place on a time scale of 10^{-11} s. After this period of time the cascade is said to be quenched, and, if the resulting defects are immobile and stable, the disorder will be quenched in. However, if defects such as vacancies and interstitials are mobile at the implantation temperature, then significant dynamic annealing and annihilation of damage can occur during implantation [39]. This dynamic annealing process is much more efficient at normal implantation temperatures in some semiconductors (e.g. GaN) than others such as silicon. Fig. 2.10 depicts the threshold amorphization dose for various group IV and III-V semiconductors by 100 keV silicon implantation at room temperature. A lower amorphization threshold indicates more damage accumulation in the material upon ion irradiation.

2.2 Ion beam imaging and milling

2.2.1 Beam size

FIB machines are nowadays sold as nano fabrication tools, thanks to beam sizes as low as 4 nm. This recent evolution was enabled by advances in science and technology of ion sources and particle optics.

An important evolution was the conception of the liquid metal ion source (LMIS). This is a tungsten needle, with a tip radius of typically 10 μm, that is covered with a thin layer of metal. This metal should have a high surface tension and a low vapor pressure at the melting point. The metal is heated to its melting point and spreads over the needle to form a thin film. When a high electric field is applied between the needle tip and an adjacent electrode (2-10 keV), the balance between surface tension and electrostatic tension will cause the liquid metal to be drawn into a conical shape with a narrow tip. The liquid tip is rapidly drawn into a radius so fine that the electric field causes ionization and evaporation of metal atoms. The radius of the liquid metal tip can be as small as 5 nm. In practise gallium is often used as a metal source because of its low melting temperature (30°C) that limits the need for heating of the source. Metal compounds with low melting temperatures can also be used, but these columns require mass separation to obtain a single element beam.

LMIS sources are bright and generate a reasonably large ion current (up to tens of nA), which makes them suited for focusing a reasonable current onto a tiny spot. This can be achieved by charged particle optics. However, the high current density near the source tip (exceeding 10^6 A/cm^2) causes perturbations of the ion trajectories due to the Coulomb force, which translates into abberations through the particle optics. Several methods were proposed for the measurement of the actual ion beam shape and diameter. In the most detailed reports it was observed that the beam can be approximated by a Gaussian core and exponential tails [40, 41, 42]. In practise it means that the tails of the beam reach further than for a purely Gaussian beam profile. When one mills a hole with FIB, which typically needs 10^{17} ions/cm^2, a large region surrounding the milled crater is not milled but suffers high dose implantation. This limits the use of FIB for applications where preservation of material quality is primordial.

2.2.2 Imaging

Imaging a sample in an optical microscope is done by illuminating it with a light source and projecting an image on a camera or into the eye by the use of lenses. However, the imaging mechanism used for scanning electron microscopy (SEM) or scanning ion microscopy (SIM) is completely different. Here the illuminating beam (electrons or ions) is focused into a small spot on the sample, and scanned

across the sample surface by scan coils. The interaction of the electrons or ions with the sample material causes the ejection of secondary electrons (these are defined as the ejected electron with energy below 50 eV) which are collected by a detector placed behind a positively biased grid. After amplification this signal is connected to a monitor (through a computer) that is scanned in exactly the same way. The brightness in each point on the screen is proportional to the number of secondary electrons (or ions) emitted at the equivalent location on the sample. When the magnification is increased (i.e. the image is zoomed in) the beam is scanned over a smaller area. Topography on the sample becomes visible because it gives rise to contrast in the secondary electron yield. As opposed to optical microscopy it is not the diffraction limit that determines the imaging resolution of SEM and SIM, instead it is the beam size and the sample interaction volume that determine the size of the smallest distinguishable feature. The sample interaction volume is the volume in which the collision cascades of the impinging particles extend and secondary electrons and ions are formed (along with other particles such as backscattered particles and X-ray photons). SEM images reach an imaging resolution of about 1 nm (for systems with a field effect source), SIM images 5 to 10 nm. When making SIM images one has to take into account that the sample surface is eroded by the impinging ions. In spite of the erosion and the lower resolution of SIM, the technique is attractive because the images often show an increased Z number contrast because of the large sputter yield differences. Furthermore, SIM shows a contrast for different crystal orientations due to ion channeling, which enables for example the imaging of grains in metals. It should be noted that SIM images, or ion microscopy images, can be made by detecting the secondary electrons or by detecting the secondary ions. However, secondary ion detection requires a specific detector; in the rest of this work SIM imaging refers to the imaging of secondary electron generated by ion impact.

2.2.3 Milling

Besides for imaging a focused beam of ions can be used for localized sputtering or milling. As shown in Fig. 2.6 the sample surface will first swell due to amorphization. For higher doses this will lead to the formation of a crater with swollen edges and sloped sidewalls due to the Gaussian-like ion beam shape. Table 2.1 summarizes the milling rate for various materials; the differences are mainly caused by the varying atomic number of the projectiles. An etch selectiv-

Material	Milling rate (μm^3/nC)	Material	Milling rate (μm^3/nC)
Al	0.30	Al_2O_3	0.08
Au	1.50	Fe_2O_3	0.25
C	0.18	GaAs	0.61
Cr	0.10	InP	1.20
Cu	0.25	MgO	0.15
Fe	0.29	Si_3N_4	0.20
Mo	0.12	SiO_2	0.24
Ni	0.14	TiN	0.15
Pt	0.23	TiO	0.15
Si	0.22		
Ta	0.32		
Ti	0.37		
W	0.12		

Table 2.1: Milling rate for various materials, by impact of a focused beam of 30 keV gallium ions. Taken from Ref. [43].

ity of more than 10 can be obtained by choosing particular material combinations.

2.2.4 Digital scanning algorithm

One can mill by ion irradiation of a spot or by scanning the ion beam continuously over an area. However, for a better control of the etch parameters and more pattern flexibility, modern FIB machines scan the ion beam in a digital way: the beam moves from point to point where ions are deposited during a given time, which we will call the dwell time. Note that this does not necessarily mean that the beam is blanked (shut off by moving away from the sample) during the movement between dwell points. However, to ensure proper digital scanning, beam movements between dwell points should be much faster than the dwell time, which is guaranteed by using electrostatic deflection lenses. The digital scanning method enables precise control of the dose and offers great flexibility of the milling sequence. However, to have a homogeneous dose spread over an area that is digitally scanned, one has to set the pitch (distance between the dwell points, also called step size) smaller than $1.5 \times \sigma$, where the beam is approximated as Gaussian with a full width at half max-

imum of $2.35 \times \sigma$ [44]. This condition translates the fact that two merging gaussian peaks feature a single peak from a certain point (but in two dimensions). Expressed in terms of beam size (defined by full width at half maximum) the condition for a homogeneous dose (merging gaussian peaks) for a digitally scanned area becomes

$$pitch < 0.64 \times beamsize. \tag{2.6}$$

However, the minimum pitch is limited by the address grid of the digital analog converter. If a machine is equipped with a 12 bit converter the field of view can be divided in 4096 pixels. This sets a lower limit to the magnifications that can be used for a given beam size. E.g. a magnification corresponding to a field of view of 100 μm yields a pixel size of about 24 nm; therefore etching with a beam current that corresponds to a size smaller than 38 nm is not possible with a homogeneous dose spread. Precise control of the pitch and the dwell time in function of the ion beam size and current makes it possible to have similar milling conditions (milling yield, shape of the crater) over a wide range of beam currents (10 pA - 10 nA).

2.2.5 Redeposition - Angle dependance

The most important reason for controlling the scanning algorithm is harnessing the three-dimensional shape of milled structures. Two major effects disturb the formation of an etch pit: redeposition and the angle dependance of the milling speed. Redeposition is the condensation of sputtered atoms close to the etch site; the angle dependance of the sputter yield was already pointed out. These detrimental effects are clearly visible when one etches a big rectangular pit in a single pass, meaning that the beam is scanned across the rectangle only once (see Fig. 2.11(a)). In that case the dwell time in each point is high, e.g. 1 s. The resulting pit is shallow where the etching started and deep where the beam was last scanned, caused by a combination of redeposition on the initially etched side and increasing milling rate as the sidewalls become steeper. This can be solved by scanning the rectangle many times and choosing a smaller dwell time, e.g. 1000 passes and 1 ms dwell time. In this case the equivalent total dose is deposited and about the same volume is sputtered, but the bottom of the well is flat (Fig. 2.11(b)). These effects were recently successfully incorporated in three dimensional simulations that calculate the shape of an etched structure in function of the utilized scanning algorithm, where it was pointed out

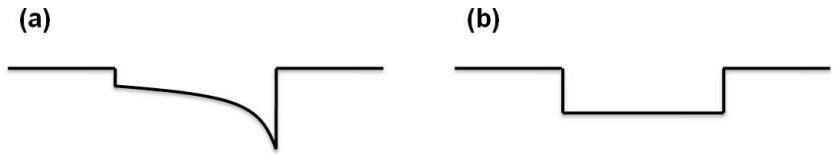

Figure 2.11: When etching a hole in a single pass (a) the bottom is not flat due to redeposition and the angle dependance of the sputter yield; spreading the same dose over many passes (b) yields a flat bottom.

that angle dependance of the sputter yield is the dominant effect in generating sloped hole bottoms [17].

2.2.6 Temperature issues

A question that often arises when deterioration of certain properties of materials is observed after FIB etching, is whether these are provoked by the temperature rise during FIB etching. The energy of the impinging ions and the ion current determine the amount of power deposited in a space that is about the size of the beam. Some of this power goes into the generation of secondary electrons, sputtered atoms, secondary ions, crystal damage, X-rays, etc. However, these fractions are all small as compared to the energy loss due to electronic and nuclear stopping, ultimately leading to heating. In this paragraph we present a simplified calculation of this temperature rise in several materials, for FIB irradiation of a bulk sample and a membrane sample (we refer to Ref. [45] for a more detailed calculation). In both cases we will look for the solutions of the general differential equation for heat conduction:

$$\frac{\partial T}{\partial t} = \kappa \nabla^2 T, \tag{2.7}$$

where κ is the thermal conductivity, t is time, and T the scalar field that represents the local temperature. We will look for steady state solutions of this equation. Our method involves some more assumptions: the ion beam is assumed stationary for a long time and heat loss due to thermal radiation is neglected. These assumptions make that our calculation will yield an upper limit of the expected temperature rise.

Bulk sample

When the ion beam impinges on a bulk material, the heat is transported through a half spherical shell. Therefore we will use spherical coordinates to rewrite (2.7) (assuming steady state) as

$$\frac{d}{dr}\left(r^2\frac{dT}{dr}\right) = 0. \tag{2.8}$$

Integration yields

$$\frac{dT}{dr} = \frac{m}{r^2}, \tag{2.9}$$

$$T = -\frac{m}{r} + n, \tag{2.10}$$

where m and n are constants to be determined from the boundary conditions. A first boundary condition can be derived from the assumption that the substrate background temperature (for $r \rightarrow \infty$) is 300 K, leading to $n = 300$ K. For the second boundary condition we will consider the source of the heat: the impinging ion beam. We consider the power (ion energy x ion current) deposited in a half sphere with radius ϕ. The boundary condition states that the deposited power dQ/dt is transported through a half spherical surface with area $2\pi\phi^2$ as heat flux. Consider the definition of thermal conductivity κ:

$$\overrightarrow{q} = -\kappa\nabla T, \tag{2.11}$$

where q is the heat flux in W/m^2. The boundary condition can be derived by integrating this equation over the half spherical surface with radius ϕ:

$$\frac{dQ}{dt} = -2\pi\kappa\phi^2\frac{dT}{dr}. \tag{2.12}$$

By taking (2.10) into account one derives

$$m = -\frac{1}{2\pi\kappa}\frac{dQ}{dt}. \tag{2.13}$$

By substitution the solution (2.10) becomes

$$T = \frac{dQ}{dt}\frac{1}{2\pi\kappa r} + 300; r \geq \phi, \tag{2.14}$$

valid outside of the region where the heat is generated. We will not consider the temperature inside the region of collision cascades. The highest temperature is reached, as expected, just outside this zone

$$T_{max} = \frac{dQ}{dt}\frac{1}{2\pi\kappa\phi} + 300; r = \phi, \tag{2.15}$$

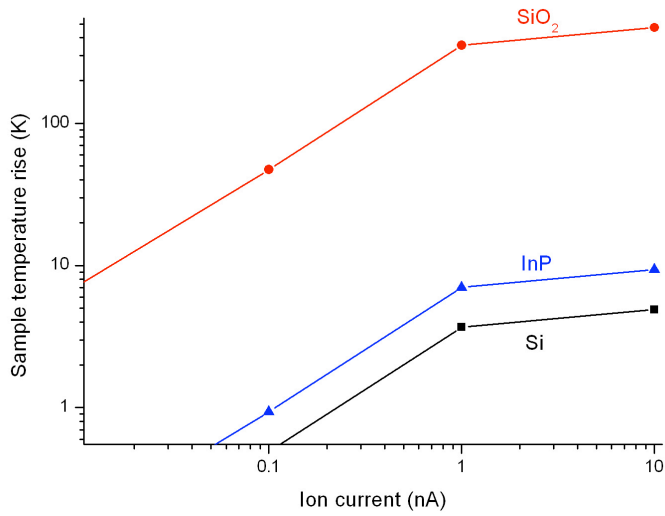

Figure 2.12: Maximum temperature rise of three bulk materials due to bombardement with 30 keV ions. The beam diameters are taken according to the calibration of the FEI machine: 10 nm @ 1 pA; 15 nm @ 10 pA; 20 nm @ 100 pA; 150 nm @ 20 nA.

and depends greatly on the beam size and current and the thermal conductivity of the material. Fig. 2.12 shows the upper limit (due to our assumptions) of the expected temperature rise (above 300 K) for Si, InP and SiO_2.

Membrane sample

In the case of a membrane sample the heat is conducted through a cylindrical shell. Transposition of (2.7) to cylindrical coordinates yields due to symmetry:

$$\frac{d}{dr}\left(r\frac{dT}{dr}\right) = 0. \tag{2.16}$$

Integration gives

$$\frac{dT}{dr} = \frac{m}{r}, \tag{2.17}$$

$$T = m \ln nr, \tag{2.18}$$

where m and n again represent the integration variables. This function leads to infinitely high temperatures which is clearly not physical. In practise the membrane will always be suspended at a cer-

tain distance; although each geometry will have to be studied separately it is clear that the theoretical temperature rise will be higher than for bulk samples. Ref. [45] gives an analytical solution for a circular membrane of a certain diameter surrounded by bulk. However, for higher temperatures the effects of thermal radiation become more prominent so more detailed calculations are desirable, as for instance presented in the following.

Silicon on insulator

In this work we are in particularly interested in a thin silicon membrane (220 nm thick) on a 2 μm oxide layer on top of a silicon substrate. As an example we have calculated the temperature in a small isolated silicon cylinder with a diameter of 500 nm, irradiated by 1 nA of 30 keV particles (the heat can only flow away through the 2 μm thick bottom oxide and the silicon substrate). This was done with a finite element solver[2], resulting in a 27 K temperature rise. As this geometry (a small isolated cylinder that is fully irradiated) would suffer more than a wire or a slab (where the ion beam covers only a small part of the silicon and more heat can leak away through the silicon membrane) we can safely conclude that temperature does not rise sufficiently to cause considerable effects.

Conclusion

We can thus conclude that for normal operation conditions (10 - 100 pA current; 30 keV) semiconductors do not undergo sufficient temperature rise for noticeable effects to take place, even not if used as a membrane on oxide. However, for suspended membranes more detailed calculations are desirable. Less thermally conductive materials such as SiO_2 and many polymers can undergo considerable heating when milled with an ion beam or imaged with an electron beam. Polymers have to be handled with extra care because they can melt or decompose at relatively low temperatures.

2.3 Ion beam deposition and enhanced etching

2.3.1 Deposition

FIB offers the possibility to deposit materials through the ion induced decomposition of a precursor gas. This process is also re-

[2]We refer to Appendix D for more details.

Material	Milling rate (μm^3/nC)	I_2 etch enh. fact.	Cl_2 etch enh. fact.	H_2O etch enh. fact.
InP	1.2	10 @ 300 K 66 @ 500 K	4.2	
Si	0.22	6.2	11.8	1/5
Diamond	0.090	1.2		2

Table 2.2: Milling rate and enhancement factor for various materials and gases in a 30 keV gallium FIB. Taken from own work and Refs. [49, 50, 51].

ferred to as ion beam induced deposition (IBID); it is a mask-less direct writing technique that allows deposition of conducting or insulating patterns. Precursor gas molecules containing the element to be deposited are injected in the vacuum chamber and adsorb on the sample surface. This is often done with a fine needle that is aligned closely (< 100 μm) to the ion impact spot and ejects a flow of precursor molecules (filling up the complete chamber would break the vacuum and disrupt the ion beam). The FIB is scanned digitally over the adsorbed layer, and decomposes the molecules. The non-volatile reaction product is deposited on the surface and the organic volatile fragments diffuse away and are pumped by the vacuum system.

A variety of metallic and ceramic materials can be deposited in this way: e.g. W, Au, Al, Pt and SiO_2 [46, 47]. However, the precursor gas is often produced by evaporation from a heated container (to avoid more complex externally fed flow systems), which limits the commercially available precursor materials. The deposited layer is always contaminated by incorporation of elements such as carbon and oxygen from the precursor gas and gallium from the ion beam. This explains why the resistivity of deposited metals is usually higher than the bulk values [48].

2.3.2 Enhanced etching

Similar to deposition by precursor decomposition, one can also use a gas that by bombardment with ions reacts with substrate atoms to form volatile species that are pumped away in the vacuum system. These gasses often do not spontaneously react with the substrate material. Table 2.2 gives an overview of some etch enhancement gases and the typical enhancement rates they induce for some materials.

However, the enhancement factor depends on several operating conditions. We will summarize a relevant kinetic model to illustrate this [52]. The yield of the chemical reaction - the ratio of removed atoms to incident ions - is proportional to the amount of adsorbed gas molecules:

$$yield = s\frac{N(t)}{N_0}, \tag{2.19}$$

where s denotes the maximum reaction yield, $N(t)$ the time dependent number of adsorbed molecules and N_0 the number of available adsorption sites. Using this approximation the density of adsorbed molecules is determined by the adsorption, desorption and consumption of molecules by ion impacts, which can be written in following differential equation:

$$\frac{dN(t)}{dt} = Fg\Big(1 - \frac{N}{N_0}\Big) - msJ(t)\frac{N}{N_0} - \frac{N}{\tau}. \tag{2.20}$$

The first term denotes the amount of adsorbed molecules, where F is the gas flux and g the sticking probability. The second term governs the consumption of adsorbates as set forth in (2.19), where m is the fraction of the molecules actually participating in the reaction, and $J(t)$ is the ion flux. The last term represents the thermal desorption of adsorbed molecules back into the gas phase. In the following this term is neglected, but it can become important if higher sample temperatures are used.

When using a digital scanning algorithm the ion beam will consume adsorbates while it dwells on a location. Since the ion flux $J(t)$ is larger than the gas flux the amount of adsorbed gas molecules will drop [52], as will the yield according to (2.19). The actual yield can be calculated by integrating the differential equation over the dwell period. The initial coverage of the dwell period $N(t = 0)$ is determined by how long the beam takes to come back to the same location and repeat the sequence. In practise the ion beam flux is not uniform and the distance between dwell point is smaller than the actual size, which means overlap has to be taken into account. The resulting model is a reliable representation of experimental conditions. This is shown in Fig. 2.13, where the calculated and experimentally determined yield are represented for a 480 pA beam with beam size of 160 nm in focus and 390 nm for a defocus voltage of 40 V. This graph shows that the yield of a chemically enhanced etch process is better for short dwell times ($<$ 200 ns). Long dwell times cause depletion of the etched region and a lower yield. It can also be seen

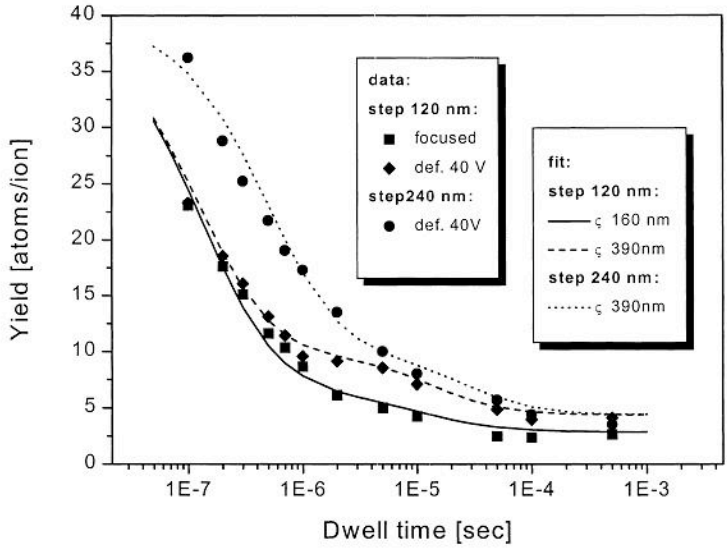

Figure 2.13: Dwell time dependance of the yield of I_2 etching of silicon for various beam size (480 pA, beam size in focus 160 nm and 390 nm for a defocus voltage of 40 V) and step size conditions. The model is validated by experimental data. Reprinted from Ref. [52].

in Fig. 2.13 that a somewhat larger step size yields a better enhancement. In practise it is observed that a homogeneous dose spread is no longer necessary to obtain flat etched interfaces. This is caused by a beam spreading effect of collisions between impinging ions and gas molecules, and by the fact that the etch enhancement is higher for the smaller ion current present in the beam tails. For iodine enhancement (see further) we will use a step size that is equal to the beam size instead of the condition pointed out in paragraph 2.2.4.

It is clear that the etch yield of a chemically enhanced process depends on the gas flux. Since the gas is usually supplied by a needle that is positioned close to the reaction site the flow profile is not symmetric, nor is the shape of etched structures. This can be overcome by using needles with a specific shape to improve an omnidirectional gas flow.

2.3.3 Electron beam deposition and etching

Similar processes are possible with an electron beam: electron beam induced deposition (EBID) is a similar technique to IBID, where

the impinging and secondary electrons decompose the precursor molecules. Most of the same precursors can be used, however, the process is often much slower than IBID. Nevertheless the process is of technological importance for cross-sectional inspection, as we will discuss later. Furthermore, deposited materials are usually less contaminated that their ion beam equivalents.

Milling with electrons is not possible - at least not at the operating conditions of a scanning electron microscope. Nevertheless it is possible to etch materials by electron beam induced chemical reactions: Ref. [53] demonstrates electron beam etching of silicon by adsorption of fluorine based gases. However, similar to EBID, electron beam etching is much slower that its ion equivalent. E.g. silicon electron beam etching with XeF_2 is 2 to 3 orders of magnitude slower than ion milling [53].

2.4 Commercially available FIB systems and applications

Small FIB machines are currently fabricated by three manufacturers: FEI Company, JEOL and Zeiss - SII NanoTechnology Inc. The machines have the size of an advanced SEM, and often feature both an electron and an ion column. The price range depends on the resolution of the columns, the size of the chamber, additional characterization equipment, etc. The system used in this work is a FEI Nova Nanolab 600. It features a high resolution field effect electron column (positioned vertically) and an ion column under an angle of 52°. The vacuum chamber is equipped with four gas injection needles: (methylcyclopentadienyl)-trimethyl-Pt for deposition of platinum, iodine for metal and semiconductor etch enhancement, trifluoroacetamide (TFA) for oxide etch enhancement and water vapor for etch enhancement of carbon containing compounds. The systems has a sample stage with high positioning accuracy (100 nm) that is compatible with 6 inch wafers. Accessory analysis techniques include energy dispersive X-ray spectroscopy (EDX) for element analysis and electron backscatter diffraction (EBSD) for crystal orientation analysis.[3] The machine is also provided with a micro manipulator needle for to pick up and move small amounts of material or for contacting. A Raith lithography system (typically used for electron beam lithography, the software specifically designed for

[3]We refer to Appendix C for more details on these

alignment and exposure tasks) with scan resolution of 16 bits can be operated with both ion and electron beam.

2.4.1 Ion Column

A schematic overview of the column in our FEI machine is shown in Fig. 2.14. The ion beam is extracted from the liquid metal ion source (LMIS) by applying a negative voltage to the extractor plate. The extraction current of typically 1-2 μA - needed for stable operation of the LMIS - limits the lifetime of a source to about 1500 hours. The beam current is reduced by the spray aperture and further down the column by a variable aperture strip. The strip determines the actual current and size of the beam. It can be shuttered by a deflection lens and aperture. When the beam is in a blanked position, it is directed into a Faraday cup that constantly measures the ion beam current. The lower octopole lens is used for scanning and steering of the beam.

Our FEI machine has both an ion and an electron beam, that are centered around the same position to enable simultaneous milling and imaging. The setup is presented in Fig. 2.15: the electron beam is positioned vertically, the ion beam is tilted at 52° from the normal position. Both beams are centered around the same point: the eucentric point, which is also the tilt center of the sample stage.

2.4.2 Applications

FIB machines with a single ion beam or with both ion and electron column are available for a wide variety of tasks. In this section we will give a short overview of some tasks relevant to this work.

Cross-section imaging

Cross-section imaging consists of the SEM inspection of a FIB etched crater wall. When a crater is formed with the FIB that is positioned 52° off-normal, one of the edges of the crater can be imaged in situ with the electron beam, that is positioned vertically. This process can be compared to the standard SEM inspection procedure of cleaving and vertical mounting of a sample. However, cross-section imaging can be done on specific locations and through layer stacks with different crystal orientations, which is hard to achieve with cleaving.

For fast cross-sectioning the initial crater is etched with a sloped bottom. Only the imaged side of the well has to be deep and the

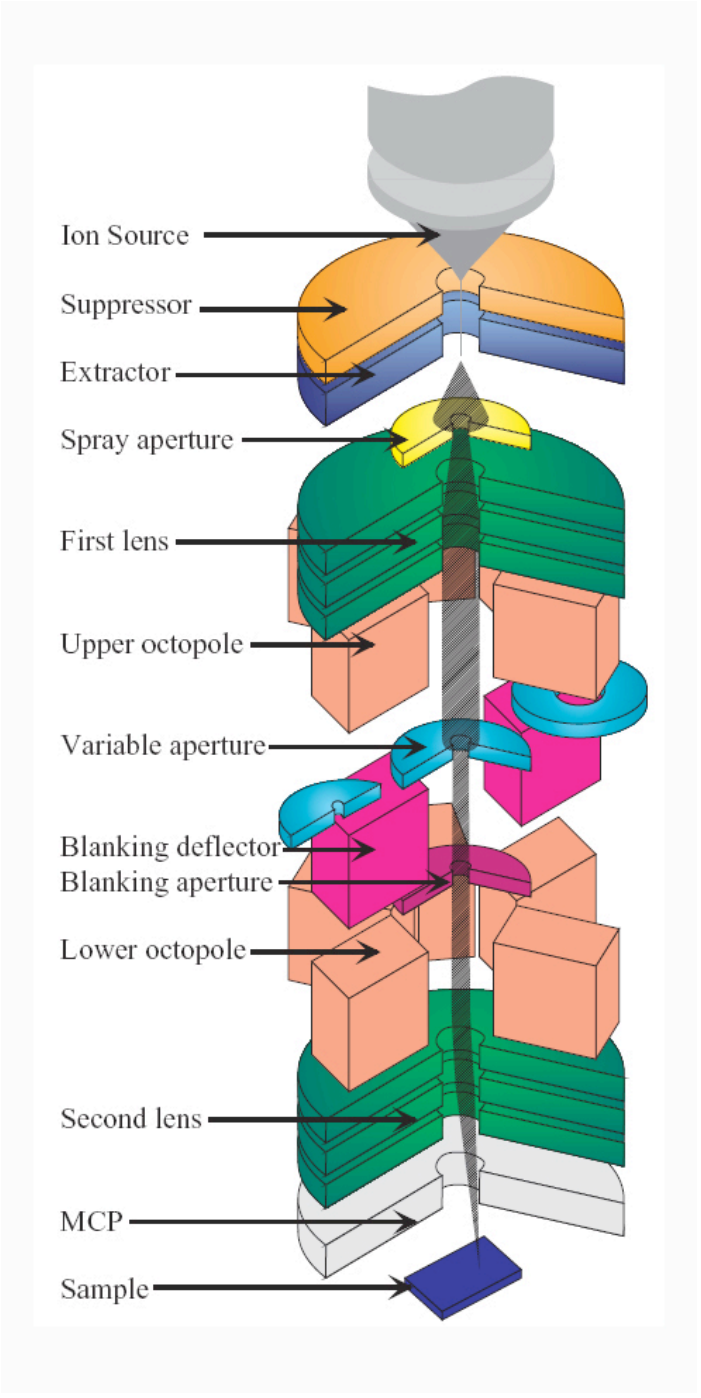

Figure 2.14: Schematic overview of the typical elements of a FIB column, reprinted from Ref. [47]. MCP stands for multichannel plate, used for the collection of secondary particles for imaging.

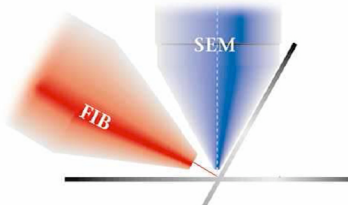

Figure 2.15: Our FEI system has a vertical electron beam and an ion beam tilted at 52°.

rest of the pit has to be sufficiently large not to shadow the interesting features. In this step high currents can be used for fast milling (1 - 10 nA), but they will result in a dirty cross-section face due to redeposited material. Therefore a second etch step - the cleaning step - is performed (at lower currents: 0.1 - 1 nA) to etch the facet line-by-line and remove redeposited material. Due to the Gaussian shape of the ion beam, the etching produces a hole with rounded edges, as displayed in Fig. 2.16(a). This would lead to inaccurate images when the interesting features are close to the sample surface. Therefore a protective layer has to be deposited on top of the region of interest before etching the sloped crater, for example ion beam deposited platinum. However, FIB deposition of platinum creates a thin damaged layer under the deposited material due to the ion impacts. Therefore, for delicate cross-sections, one first deposits a thin layer of platinum with electron beam deposition (in machines with two beams) before starting the (faster) ion beam deposition of the protective layer. The rounded edge of the crater will now form in the platinum layer (Fig. 2.16(b)) and the buried features appear as in a cleaved cross-section. In machines with both electron and ion beam the image can now be made in situ with SEM. Nevertheless, for a correct geometric representation of the buried features the image has to be stretched vertically to correct for the 52° projection angle.

The procedure of cross-section imaging is of key importance for fabrication process optimization, as depicted in Fig. 2.17. In this example a cross-section is made through a III-V microdisk laser, heterogeneously integrated on a silicon photonic circuit [7]. The cross-section can be made during a multi-step fabrication process to verify critical etch depths and alignments, which considerably increases the yield of a complex lithography fabrication process that is not yet tuned for high reliability manufacturing. In the micro-electronics industry the procedure of cross-section inspection is referred to as

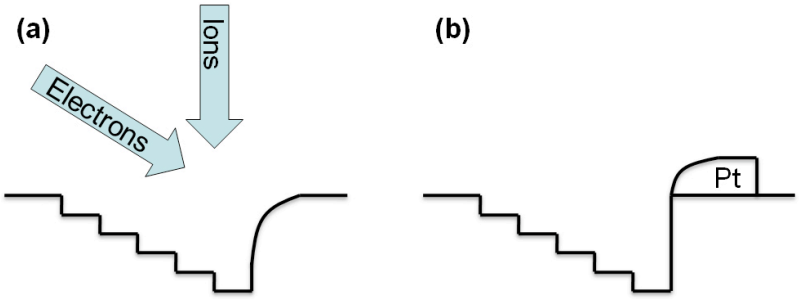

Figure 2.16: Schematic representation of cross-section imaging. (a) With no additional layer the features close to the surface are not represented correctly. (b) An additional platinum layer solves this problem.

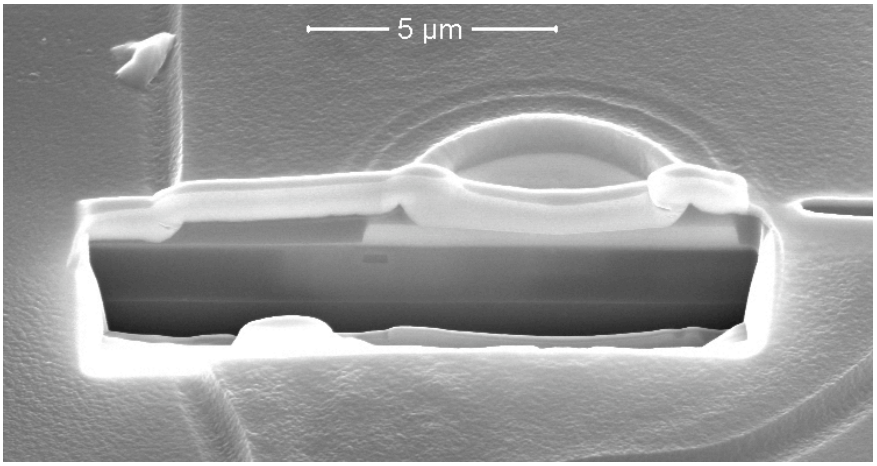

Figure 2.17: FIB cross-sectional imaging is of key importance for the optimization of complicated fabrication schemes, such as this microdisk laser integrated on a silicon chip [7].

failure analysis. FIB is the only technique that can accurately reveal buried defects in a complementary metal oxide semiconductor (CMOS) chip.

An effect often observed in the cross-sectioning of thin slits is the creation of voids. They are created when during the platinum deposition the top of the slit closes up before it is completely filled, as shown in Fig. 2.18. This has to be taken into account when interpreting cross-section micrographs.

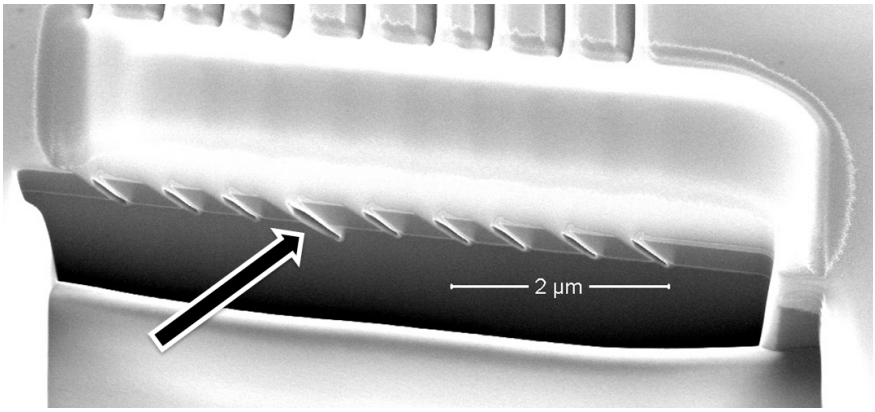

Figure 2.18: FIB cross-sectioning of thin slits can produce voids that complicate interpretation.

Transmission microscopy slice preparation

A similar technique can be applied to prepare transmission electron microscopy (TEM) samples. [4] By etching two adjacent craters with sloped bottom one can erode a thin slice of material (see Fig. 2.19). Similarly it is covered by a platinum layer before the craters are milled with a high current. In a subsequent step the slice has to be transported to a grid for mounting into the TEM. First a micromanipulator is attached to the slice by local platinum deposition, then the bottom and edges of the lamella are cut by FIB milling, and finally the slice is transported to the grid and welded by platinum deposition. In a final step the slice is cleaned and thinned down to as low as 60 nm before it is ready for TEM inspection. This lift-out technique enables site-specific TEM inspection and is therefore important for various research areas such as micro-electronics, materials science, etc.

Circuit edit

A different type of specialized tools is available for editing microelectronic devices, i.e. rerouting the electrical connections in the metallization layers on CMOS chips. These machines usually feature a single-beam FIB with a vertically positioned ion column and a variety of gas injectors. Since it is often needed to mill or deposit in deep craters it is preferable to have a gas injection system with omnidirectional gas flow, which is feasible by using a needle with a

[4] See Appendix C for more details.

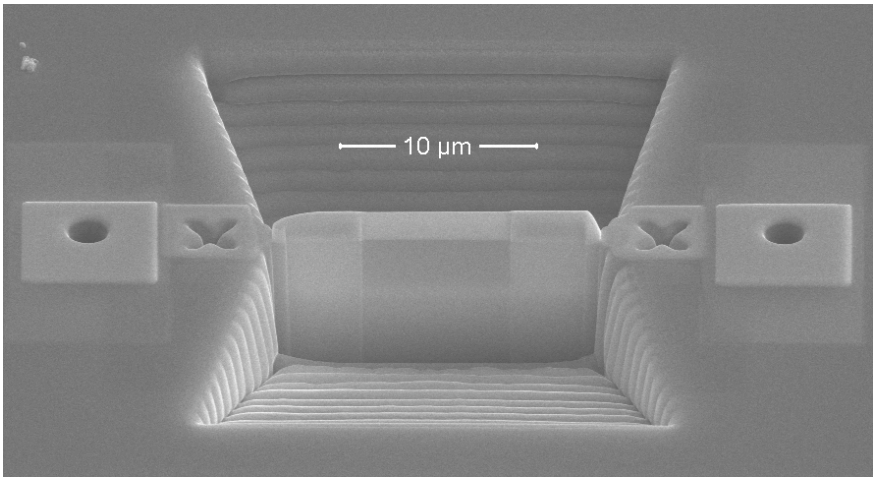

Figure 2.19: FIB allows preparation of transmission electron microscopy (TEM) samples of localized features on a chip.

donut-shaped extension at the tip. Alignment of the sample to the mask design files is often difficult by SIM because chemical mechanical polishing (CMP) between the metallization layers smooths away the topography contrast; therefore an optical microscope image is often used for alignment. Buried structures are revealed by FIB etching and monitoring of the current through the sample. When a buried layer is reached one often observes a sudden change in sample current, as well as a change of the signal on the secondary electron detector. Once a metallization layer is revealed, the connections can be cut by milling or enhanced etching; and new ones can be made by metal deposition. Afterwards the circuit can be sealed by oxide deposition. The procedure of circuit edit greatly decreases the time for design correction and verification of CMOS devices.

2.5 Ion clusters

Current FIB machines mostly have a gallium or an indium source, but other elements are available as well when alloy liquid metal sources are used in combination with mass separation columns. However, the ions always carry a single charge, and the complete energy (of around 30 keV) is delivered on the sample by one particle. This leads to relatively deep implantation and damage cascades, and is not optimal when milling is the primary objective. It was recently demonstrated that more efficient milling can be obtained with a clus-

ter ion beam [54]. In such a beam the impinging particles carry the same amount of energy and also have the elementary charge. But the particle consists of many atoms, which limits the amount of energy per atom. Fig. 2.20 shows a molecular dynamics simulation of the impact of a 15 keV gallium ion and a 15 keV C_{60} cluster. It is clear that the damage in the case of the cluster impact is much shallower and more of the energy is actually used for sputtering. It was also calculated that on average 53 of the 60 impinging C atoms are removed per C_{60} impact, whereas only 6% of the gallium impacts leads to ejection of a gallium projectile atom. This means that cluster bombardment inherently leads to lower degrees of impurities. However, the technology of cluster ion sources is still in a preliminary phase and they will not be commercially available for some years.

2.6 Conclusions

In this chapter we have discussed the basic ion-solid interactions that govern FIB technology. The basic interaction is a collision between the impinging ion and the solid target atoms that leads to momentum loss and stopping of the projectile. It also leads to movement of target atoms and eventually to sputtering of atoms from the target material. Focusing the ion beam into a nanometer sized spot and scanning it enables milling of sub-micrometer structures into nearly any material; and has led to a wide variety of applications. Techniques such as preparation of site-specific samples for TEM inspection and failure analysis of electronic chips would not be possible without FIB.

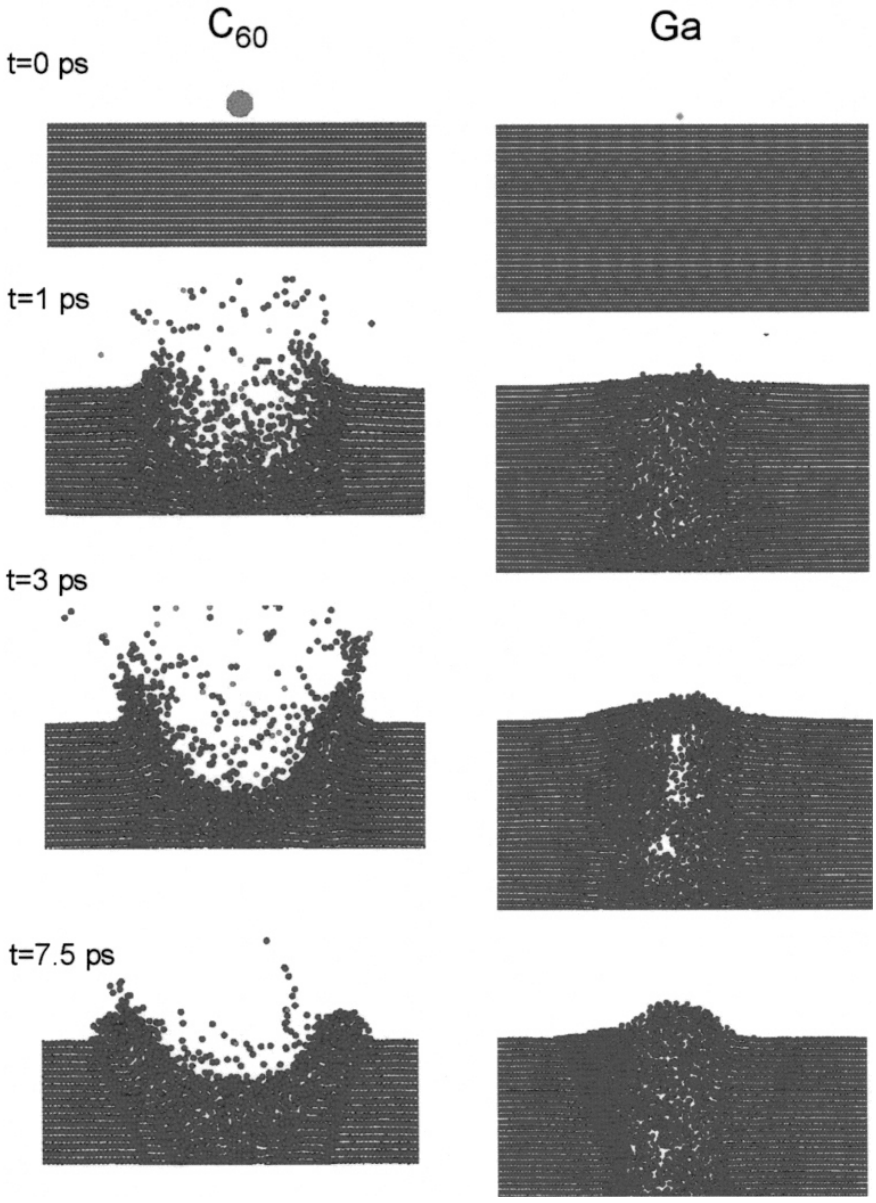

Figure 2.20: Temporal view of the molecular dynamics simulation of a typical impact of a 15 keV C_{60} cluster compared to a 15 keV gallium ion. Due to the smaller energy per particle the C atoms are efficiently ejected and a crater with a shallow damaged layer is formed. Reprinted from Ref. [54].

Chapter 3

Reducing the losses of FIB etched silicon

Thanks to the small dimensions of the ion beam in current FIB systems it is possible to etch structures in silicon photonic devices that are smaller than what can be achieved with optical lithography, even at deep-UV wavelengths as small as 193 nm. This makes FIB an attractive and flexible direct etch technique for the fabrication of device prototypes and for high-resolution device modifications. However, direct FIB milling of optical devices makes them extremely lossy and therefore not practicable.

In this chapter we present several approaches for the reduction of the optical losses. First we present a survey of literature on gallium implanted silicon, explain the general outline of the experiments, and discuss the extremely high losses in directly milled silicon. In the next section we present a preventive technique for optical loss reduction: chemical gas enhancement. Finally we elaborate on two regenerative techniques that we have investigated in collaboration with MESA+ Institute in the Netherlands: high temperature annealing and removal of the damaged layer.

3.1 Literature survey

The purpose of this section is to gain insight into the properties of gallium implantation and doping of silicon substrates. We will address implantation induced amorphization of silicon and crystal regrowth, as well as electrical activation and deactivation of the gal-

lium dopants. These mechanisms are important to understand the effect of gallium impurities in silicon at elevated temperatures, more specifically the optical properties.

Gallium is a p dopant in silicon. However, in practise it is not often used for actual doping due to the low solid solubility of gallium in silicon (4×10^{19} cm^{-3}) [55, 56] and due to the high diffusivity in SiO_2 [57]. Nevertheless, it is possible to achieve electrical activation higher than the solid solubility if the dopant is projected into amorphous material that is later recrystallized by annealing. This recrystallization process is also referred to as crystal regrowth and occurs through the mechanism of solid phase epitaxy. During this rapid process (typically several minutes at 500-600 °C) the implanted impurities can be incorporated into the newly formed crystal lattice. Furthermore, the temperature is often too low for substantial diffusion and the time is too short for a solid solubility equilibrium to form. For gallium implantation in silicon a dose of 2.5×10^{14} cm^{-2} is enough to generate an amorphous layer [57][1]. This is low compared to for example boron implantation, where the silicon lattice becomes amorphous for implantation doses above 2×10^{16} cm^{-2}. If one wants to achieve implantation above the solid solubility in this case, a pre-amorphization step with for example Si^+ can be applied.

Annealing at 600°C completely recrystallizes the amorphous layer, and yields a maximum electrical activation of the gallium dopants [57, 61]. Recrystallization starts at about 550°C, where the $\{001\}$ and $\{110\}$ crystal planes grow faster than others; thus spherical implantation zones become cubic-shaped before disappearing completely [58]. For implantations beyond the solid solubility limit, annealing at temperatures above 600°C will cause the electrical deactivation of gallium dopants by the formation of precipitates or clusters that are electrically inactive [57, 61]. A competing effect at high temperatures is the diffusion of the gallium impurities out of the silicon. To achieve a sufficiently long diffusion path temperatures as high as 1000°C are necessary. Another important effect at elevated temperatures is evaporation of gallium. We will elaborate on this later.

No specific reports were found on the effects of gallium implantation on the optical properties of silicon. However, it is likely that an electrical activation of gallium dopants leads to free carrier absorption; and that precipitation of gallium clusters is detrimental

[1]This value is for 200 keV gallium ions. Literature also reports on a critical dose of 5×10^{14} cm^{-2} for 100 keV [58], 1.5×10^{14} cm^{-2} for 59 keV [59] and 8×10^{13} cm^{-2} for 50 keV [60] gallium ions

for the optical transmission as well. The goal in this chapter is to study the optical losses induced by high dose gallium implantation and sputtering, and to investigate three mechanisms to reduce the losses. A first mechanism is the use of iodine etch enhancement, a second one is high temperature annealing, and a third technique is removal of the damaged layer by wet or dry etching techniques.

3.2 General experimental setup

3.2.1 Implanting/etching waveguides

To assess the losses induced in silicon by etching with a focused gallium ion beam, we have chosen to etch predefined waveguides on silicon on insulator wafers. The fabrication process of these waveguides consists of 248 nm optical lithography and inductively coupled plasma (ICP) etching in an HBr/Cl atmosphere; we refer to Refs. [62, 63] for more details. This process defines 10 μm wide multi-mode and 500 nm wide single-mode waveguides as well as shallow grating couplers in a 220 nm thick crystalline silicon layer (slightly p-doped $\sim 10^{15}$ cm^{-3}) on top of a 2 μm thick oxide layer, on a 750 μm thick silicon substrate.

By scanning the ion beam across the top surface of these waveguides they are implanted and sputtered. Whether the silicon is actually etched depends on the dose of the incident ions. The experiments in this work are conducted with a FEI Nova Nanolab 600, equipped with a 30 keV gallium beam with minimal spot size of 7 nm, and a 30 keV electron beam for in situ inspection and ion beam alignment. To enhance the etch process by iodine chemistry, our system is equipped with a gas nozzle that can be positioned near the etch site (at a distance of about 100 μm). The nozzle contains a crucible with solid I_2 that is heated to about 42°C, causing the iodine to sublimate and adsorb to the silicon surface. The beam placement accuracy is limited by the 12 bit digital analog convertor of the scan generator and can be calculated as one 4096th of the field of view.

The ion beam is scanned over the waveguide, with a digital scanning algorithm, across a rectangular area. The length of the rectangle is varied and the width of the rectangle is chosen slightly larger than the etched waveguide to simplify alignment. Because even a single scan with the ion beam damages the silicon waveguides, SIM can not be used for alignment of the etched rectangles on the waveguides. Therefore, alignment was performed by first carefully align-

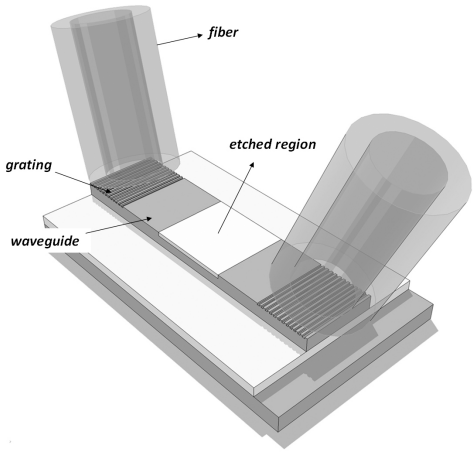

Figure 3.1: The experimental setup: measurement of the transmitted optical power through implanted and etched silicon waveguides.

ing the electron and ion beam and the sample. Nevertheless, when the sample is moved, this alignment deteriorates because it is difficult to mount the sample perfectly horizontally. Therefore, proper alignment is only possible when the initial alignment of both beams and the sample is done close to the etch site (< 100 μm).

3.2.2 Loss measurements

The 500 nm wide single-mode waveguides (also referred to as wire waveguides) are tapered to broad 10 μm waveguides by adiabatic tapers. These are provided with grating couplers to couple light from a single mode fiber to the chip and back (see Fig. 3.1). 10mW of light at a wavelength around 1.55 μm, produced by a super luminescent light emitting diode (LED) is polarization controlled and coupled into the waveguide. The grating couplers will couple only the TE fraction of the light into the waveguides. When the fibers are carefully aligned on top of the grating couplers the optical power is coupled only into the ground mode of the broad waveguides and no optical loss is observed when they are tapered to single-mode waveguides. The transmitted spectrum has a Gaussian shape [64] and is measured by a spectrum analyzer with a resolution of 60 pm. The transmitted power is extracted from these spectra by taking the peak transmission. We have observed no change in the Gaussian shape of the spectrum and therefore we suppose that the observed

loss is independent of the wavelength (for the approximate range of 1500-1600 nm). To measure the losses in the implanted or etched waveguides we use a method similar to the cut back method: waveguides are implanted with the same dose over varying lengths. Linear regression analysis of the optical losses in function of the implanted length yields the excess losses per unit length and the standard error of this quantity. Each grating coupler has a loss of about 7 dB (slightly variable on different samples due to different exposure parameters or alignment issues), so the expected loss of an unimplanted waveguide is about 14 dB. The sample length is 7 or 12 mm and the length of the single-mode sections never exceeds 5 mm, which makes the waveguide losses of about 0.1 dB/cm for broad waveguides and about 2 dB/cm for single-mode waveguides negligible. Furthermore, since we use the cut-back method that involves only relative measurements, absolute losses that are equal for all waveguides are of no importance.

3.3 Direct milling of silicon

3.3.1 Experimental details

For these experiments we have used a FIB beam current of 300pA. To have a homogeneous dose spread in the etched region, the pitch should be chosen smaller than 0.65 times the beam width [44]; in this experiment we have chosen pitch = (0.5 $\times$ beam width). Due to the limited pixel size this leads to digital analog converter problems when a large field of view is used with a small beam diameter (when the pitch becomes smaller than the address grid of the digital analog converter, i.e. 12 bit used for these experiments). So we have used extra blur by defocusing, to reach an actual beam diameter of 105 nm, in contrast to the normal size of 33 nm for a 300pA beam. For a 10 μm $\times$ 10 μm area and a 1 μs dwell time, a dose of 5×10^{15} Ga/cm^2 is delivered in 74 passes of 36.1 ms (2.67 s in total).

3.3.2 Results and discussion

Dose Choice

It is known from SRIM [33] that a large number of gallium atoms are implanted into silicon per sputtered substrate atom, causing amorphization and implantation of silicon. This process also induces optical losses. To investigate these optical losses we have implanted

10 μm wide waveguides over different length sections to estimate the excess losses per unit length. We have chosen an implantation dose of 5×10^{15} Ga^+/cm^2 for two reasons. Firstly, we have aimed for a sufficiently high dose to have amorphization. From literature we have estimated that at 30 keV a dose of 1×10^{14} Ga^+/cm^2 is sufficient to make an amorphous silicon layer [57, 58, 59, 60]. Secondly, we may not etch away too large a fraction from the silicon waveguide not to encounter mode mismatch losses. It was reported in Ref. [36, 65] that silicon swells at low dose implantations (typically $< 5 \times 10^{15}$) due to material damage, and an etch crater will form at higher doses. So we expect no net etching in our experiment, which was confirmed by measuring the depth profile afterwards.

Fig. 3.2 represents the depth profile of 30 keV gallium ions implanted in silicon. The depicted quantity is the ratio of impurity concentration (in cm^{-3}) to implanted dose (in cm^{-2}), in function of the target depth. The peak of the profile is at about 30 nm depth with about 4×10^5 cm^{-3}/cm^{-2}. This means that if one implants the threshold dose for amorphization (1×10^{14} Ga^+/cm^2), the peak concentration is 4×10^{19} Ga^+/cm^3. If we assume that this is the threshold concentration for amorphization, we can estimate the amorphization depth for higher dose implantations from the same graph in Fig. 3.2. For the implantation dose of 5×10^{15} Ga^+/cm^2 the threshold amorphization concentration is reached where the ratio of concentration to dose reaches $4 \times 10^5/50$: at a depth between 50 and 60 nm. This depth was confirmed by Ref. [66]. However, this simple estimation does not hold for the region closer to the surface. In fact not only the depth profile of gallium impurities but also the crystal damage they leave behind along the collision track.

The peak concentration in our experiment is expected to be about 1.8×10^{21} Ga^+/cm^3, or 3.6 at% (The experimental verification will be discussed later).[2] This is far above the solid solubility of gallium in silicon at room temperature (10^{19} Ga^+/cm^3 [55]). However, due to the low diffusivity of gallium in silicon, this configuration is stable at room temperature.

Optical losses

The results are plotted in Fig. 3.3. We have measured a loss of 3520 $\pm$ 90 dB/cm for directly etched waveguides.

[2] The silicon density is 5×10^{22} atoms/cm^3.

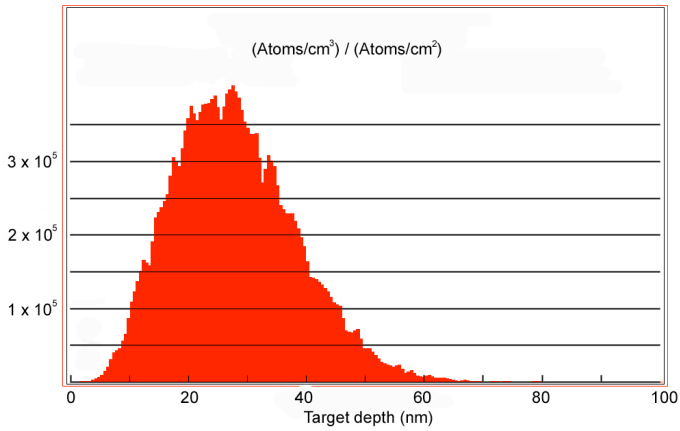

Figure 3.2: Depth profile of 30 keV gallium atoms inplanted in silicon, as calculated with SRIM.

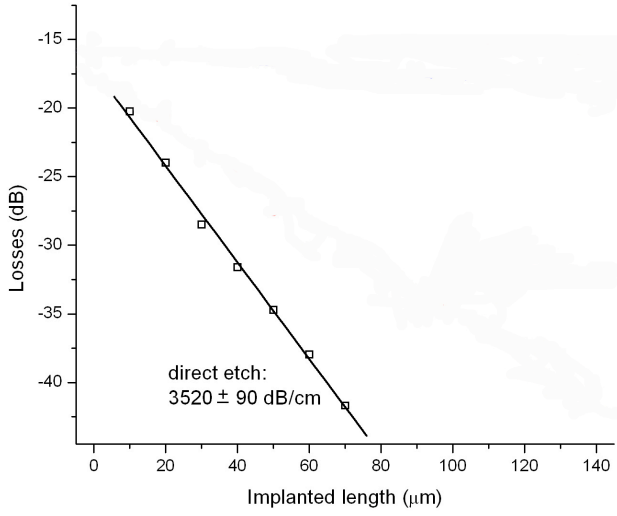

Figure 3.3: The optical losses in directly etched silicon are too high for practical use.

To investigate the nature of these losses we will first look at carrier absorption, assuming a complete electrical activation of all gallium atoms (which is unlikely without any annealing). For this purpose we will assume a homogeneous dose of 1×10^{21} Ga^+/cm^3 in the top 50 nm layer of the waveguide. According to ref. [67] this leads to a free carrier absorption due to the p-type carriers of $\alpha = 6000$ cm^{-1}. However, considering that the lossy region of the 220 nm thick waveguide is located in the top 50 nm, the actual modal losses are lower. We have computed the losses of the fundamental mode in this case with a mode expansion software CAMFR[3]: about 2500 dB/cm. This proves that, even if all gallium atoms are electrically active, the losses we have measured can not only be explained by carrier absorption.

Another simplified model consists in calculating the optical losses from the bulk metallic gallium absorption, as proposed in Ref. [25]. The optical loss in this case can be estimated by assuming a linear model: taking into account the fraction of gallium atoms in the silicon. In our case we again postulate a homogeneous concentration of 2 at% of gallium in the top 50 nm of the waveguide. This assumes that all gallium atoms are clustered in metallic particles, and interact with 2% of the light. With the metallic gallium bulk absorption value of 4.2×10^6 cm^{-1} for 1.55 μm light this leads to a material absorption in the lossy region of 84000 cm^{-1}. If the mode overlap is be taken into account this leads to a loss that is still about an order of magnitude higher than what was measured. So this simplified model greatly overestimates the losses.

It is not well known what the exact origin of the optical losses in high dose gallium implanted silicon is. It is larger that what can be explained by carrier absorption, but still much lower than the loss one expects if metallic gallium clusters are formed. The first simplified model assumes a semiconductor with impurities; the second model assumes purely metallic behavior. We think it is safer to say - at the considered impurity levels of several at% - that a supersaturated gallium-silicon alloy forms with specific electromagnetic properties. More work is needed to fully characterize this material.

From a technological point of view it is clear that losses of about 3500 dB/cm are too high to make useful devices where the optical mode is confined near the etched region, such as photonic crystals or grating couplers. This will be under discussion in Chapter 4. It can

[3]We refer to Appendix D for more details on simulation techniques.

be expected that these losses are lower for lower energy particles; this will also be discussed in Chapter 4.

Channeling

It was mentioned in Chapter 2 that the implantation depth can be deeper due to ion channeling. However, due to the low silicon amorphization dose for gallium implantation, and considering the high implantation doses that will be used in our experiments, we do not expect a significant effect of tilting the sample to 7°. To verify this statement an experiment was conducted with implantation dose of 1.5×10^{16} Ga^+/cm^2 for tilt angles of 0°, 3.5° and 7°. The optical losses were measured by comparing the optical transmission through a reference structure and through the three implanted waveguides. No cut back was used for this measurement. The results are presented in Table 3.1: considering the error bars that have to be taken into account (see later) there is no significant effect of implanting at an angle. This is confirmed by secondary ion mass spectroscopy (SIMS)[4] measurements in Ref. [57]. For the remainder of this work all implantation and etch experiments are conducted at normal incidence if not specified otherwise.

Implantation tilt (°)	Length (μm)	Loss (dB)	Loss (dB/μm)
0	20	17.12	0.86
3.5	20	17.23	0.86
7	20	17.97	0.90

Table 3.1: Optical losses in three waveguides implanted at different tilt angles: no significant effect is observed.

3.4 Loss reduction by chemically enhanced etching

3.4.1 Rationale and preview

As mentioned in Chapter 2, iodine etch enhancement is known to increase the etch rate of silicon and several other semiconductors and metals. As an increased etch rate means a lower overall dose

[4]We refer to Appendix C for more details on some sample characterization techniques.

for the same amount of removed material, the damage and optical losses are expected to be lower.

The rationale for investigating this technique, as an alternative to high-temperature annealing, is the anticipation of post-processing of opto-electronic devices. Such devices often feature metal pads, polymer, or integrated III-V material, which makes annealing at temperatures in excess of 400°C impossible.

In this section we discuss the etching of pre-fabricated silicon waveguides with iodine enhancement; in this case the losses decrease as compared to direct milling. Furthermore, we have found that baking at 300°C after the FIB etching minimizes the losses even further. First some specific experimental details are presented. In the next paragraph we will elaborate on the measurement results and discuss the elemental and chemical analysis. Finally an experiment to extract the material loss of iodine enhanced FIB etched silicon is presented.

3.4.2 Experimental details

In these experiments a beam energy of 30 keV was used. We will discuss some experiments with lower beam energy in Chapter 4. For the iodine enhanced etching a dwell time of 400 ns was chosen to avoid depletion of the adsorbed molecules [52]. [5] The pitch was chosen equal to the beam size. Although this leads to a non-homogeneous dose spread over the rectangular area - according to Ref. [44] - etched craters still have a flat and smooth bottom. This can be explained by the model for absorption and consumption of absorbed molecules (Chapter 2): a smaller ion current in the Gaussian beam tails gives rise to less depletion and a higher etch enhancement. This means that the constraint of pitch $<$ (0.65 $\times$ beam width) can be relaxed for enhanced etching. Similar to the previous experiment we have used an ion beam current of 300 pA and a defocused beam size of 105 nm, in this case with a pitch equal to the beam size. Finally this leads to a scanning algorithm with 831 passes of about 3.2 ms to deposit a dose of 5×10^{15} Ga/cm^2 to an area of 10 μm $\times$ 10 μm.

[5] Our machine has a lower limit of 100 ns, but values lower than 400 ns are not desirable to avoid problems due to the limited beam steering speed. This is because the beam is not shuttered between dwell points and the movements between dwell points are not infinitely fast (typically 50ns); the ratio of dwell time to beam movement time has to be sufficiently high to avoid significant etching between the dwell points.

The samples for surface and ion profile analysis were prepared on a silicon wafer with 20 nA on a 500 μm $\times$ 500 μm area with a beam width of 1.6 μm. The larger area and current were necessary for successful X-ray photoelectron spectroscopy (XPS)[6] and secondary ion mass spectroscopy (SIMS) analysis. Nevertheless, the current density is of the same order of magnitude as for the small-area implantation.

3.4.3 Results and Discussion

Iodine enhanced etching

To enhance the etch rate a thin needle is injected into the vacuum chamber and a container with solid I_2 is heated up so the molecules are sublimated and ejected onto the silicon sample. On impact near the etch site, the iodine atoms adsorb to the silicon surface [68, 69, 70, 71] creating SiI_x bonds. The species formed in this reaction are not volatile at room temperature, so the silicon surface will not be etched without additional heating. However, when gallium atoms impact on the surface and disturb the thermodynamic equilibrium, the silicon-iodine molecules can desorb and are pumped away in the vacuum system, so the surface is etched. This process greatly enhances the etch rate, as was also reported for other adsorbed halogens [50].

Fig. 3.4 (data points marked as $\circ$) shows the measured excess losses in waveguides etched with the same dose as previously (5×10^{15} Ga^+/cm^2), but with iodine atoms adsorbed to the surface. From the measurements we have extracted an excess loss of 1690 $\pm$ 90 dB/cm. This is the first proof of less optical absorption in halogen enhanced focused-ion-beam etched silicon. Similar results were reported for the photoluminescence of GaAs in the case of chlorine etch enhancement [72, 73, 74].

Gallium depth profile

SIMS was performed (with a 500 eV O ion beam and final crater depth of 200 to 300 nm) to investigate the depth profile of gallium in the case of direct etching and iodine enhanced etching. The results are depicted in Fig. 3.5. The gallium profile is the sum of both stable isotopes that were measured separately. A first observation is the peak dose for the direct etch: from SRIM calculations we had

[6] We refer to Appendix C for more details

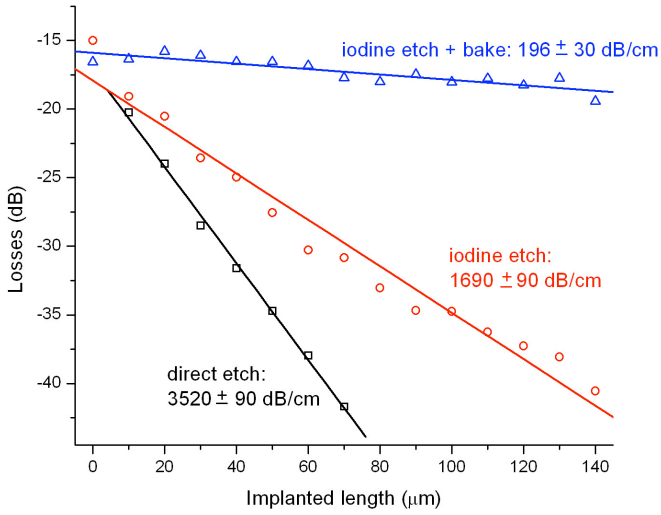

Figure 3.4: Loss measurements for iodine enhanced etched silicon waveguides before (○) and after (△) thermal treatment (see later). The losses decrease considerably as compared to direct milling (□).

expected a dose of 1.8×10^{21} Ga^+/cm^3, whereas the graph shows only 1.0×10^{21} Ga^+/cm^3. By integrating over the entire depth range we have calculated a real area dose of 2.99×10^{15} Ga^+/cm^2, instead of the exposed 5×10^{15} Ga^+/cm^2. In the case of iodine enhancement this discrepancy is even bigger with a real area dose of 1.98×10^{15} Ga^+/cm^2. Although we don't have an explanation for this discrepancy, the doses are still sufficiently high to amorphize silicon and our further conclusions will not be altered.

It is also clear from the graph that the silicon density is lower in the regions where the gallium dose is high, which we expect due to amorphization and swelling. The silicon profile for the enhanced etches suggests a higher silicon density near the surface, however, this might only seemingly be so due to the higher ionization rate in the SIMS measurement due to the presence of iodine near the surface.

Another observation is the shallower implantation depth in the case of iodine enhanced etch: the peak dose has shifted from 28 nm to 11 nm when iodine enhancement is applied. A bake step at 300°C (see further) does not noticeably alter the depth profile. This shallower depth profile can be explained by the higher sputter yield in the case of iodine etch enhancement. We have mentioned in para-

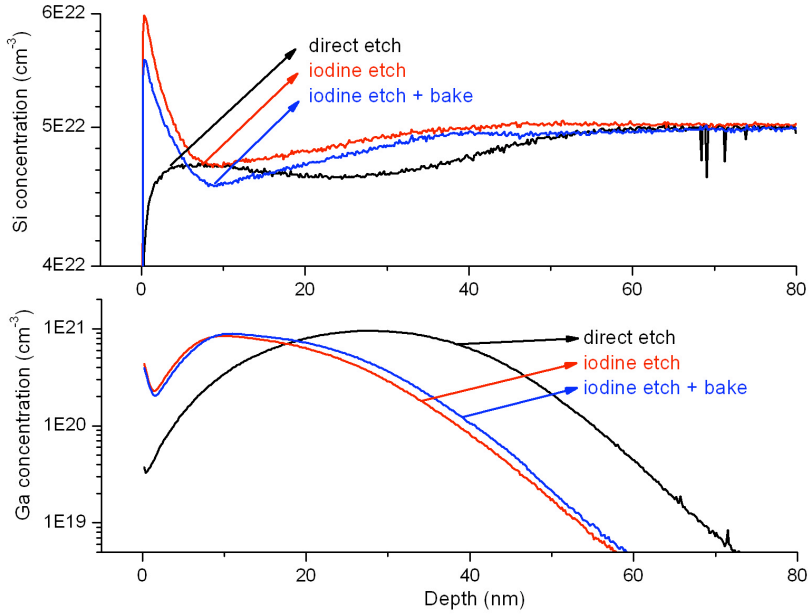

Figure 3.5: Depth profile of the silicon and gallium concentrations as obtained by SIMS. The implantation depth in the case of iodine enhancement is significantly lower, and baking for 2 hours at 300°C only slightly alters the profile.

graph 2.1.4 that for high dose implantations a steady state concentration appears. The initial depth profile is altered due to material removal and depression of the material interface. This can be simulated with the software package *Profile Code*[7] that uses semi-empirical formulas instead of Monte Carlo simulations to calculate the depth profile of implanted ions. The program takes into account the surface depression by sputtering and clearly shows steady state behavior for high implantation doses. We have performed a simulation for gallium implantation of silicon with two different sputter yields. One for a sputter yield of 1.8, which is the amount of removed silicon atoms per incident 30 keV gallium ion as indicated by the program, and another one for a yield of 11, which is the expected yield for iodine enhanced etching according to Table 2.2. Fig. 3.6 presents the gallium concentration profiles for different implanted

[7]The simulations were done at the University of Michigan (Ann Arbor, United States) in the group of Rachel Goldman. For more information on this program we refer to http://www.coresystems.com.

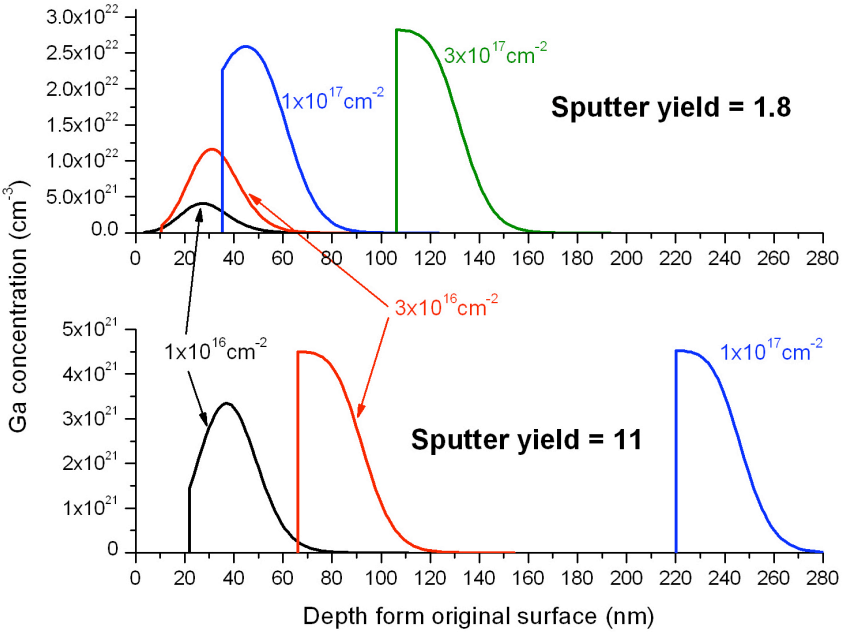

Figure 3.6: Profile Code simulations for high dose implantation of silicon with gallium (sputter yield 1.8) and for iodine enhanced etching (sputter yield 11).

doses, where a Gaussian approximation is used. The origin of the horizontal axis represents the position of the initial target surface. It can be seen that the sample surface erodes faster when the sputter yield is higher, and that the steady state dose is reached faster. The steady state concentration is roughly inversely proportional to the yield, as was put forth in the calculation in paragraph 2.1.4, which means that it is about a factor of 6 lower for enhanced etching that for direct milling.

The lower steady state concentration and the shallower concentration depth profile support the lower optical losses due to the lower amount of impurities and the lower overlap with the optical mode.

Iodine desorption by thermal treatment

Most of the iodine-silicon bonds created by the ion bombardment are not volatile at room temperature, and possibly remain on the surface. Therefore, we have baked the samples for two hours on a hot plate at 300°C in N_2. The optical measurements of samples implanted with equal dose (5×10^{15} Ga^+/cm^2) with iodine and ther-

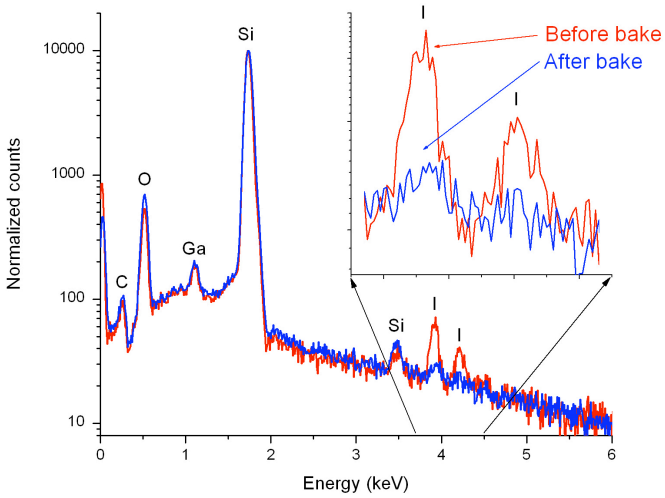

Figure 3.7: Graph of the energy dispersive X-ray spectroscopy (EDX) analysis before and after thermal treatment at 300°C. The inset zooms in on the iodine peaks, and shows that the iodine content of the sample surface noticeably decreases during the treatment.

mal treatment show a remarkable decrease in excess optical losses, as shown in Fig. 3.4 (data points marked as △). We have measured a loss of 196 ± 30 dB/cm.

To verify the chemical and elemental composition of the etched and (or) baked surface we have performed energy dispersive X-ray spectroscopy (EDX) and X-ray photoelectron spectroscopy (XPS) analysis. [8] The EDX (see Fig. 3.7) analysis was done at grazing incidence with 10 keV electrons to give as much information as possible about the composition of the surface. However, a Monte-Carlo simulation has taught us that the depth of the typical interaction volume in this analysis is still at least 500 nm. So this analysis will mainly probe the silicon bulk. From the graph in Fig. 3.7 we can clearly see that the amount of iodine decreases after baking, whereas the gallium content remains constant. This is as expected since the diffusion of gallium in silicon is slow - even at 300°C - and is also supported by the SIMS measurement in Fig. 3.5.

To gain more insight in the surface composition of the samples we have conducted an XPS analysis.[9] X-ray generated photo-electrons

[8] See Appendix C
[9] See Appendix C

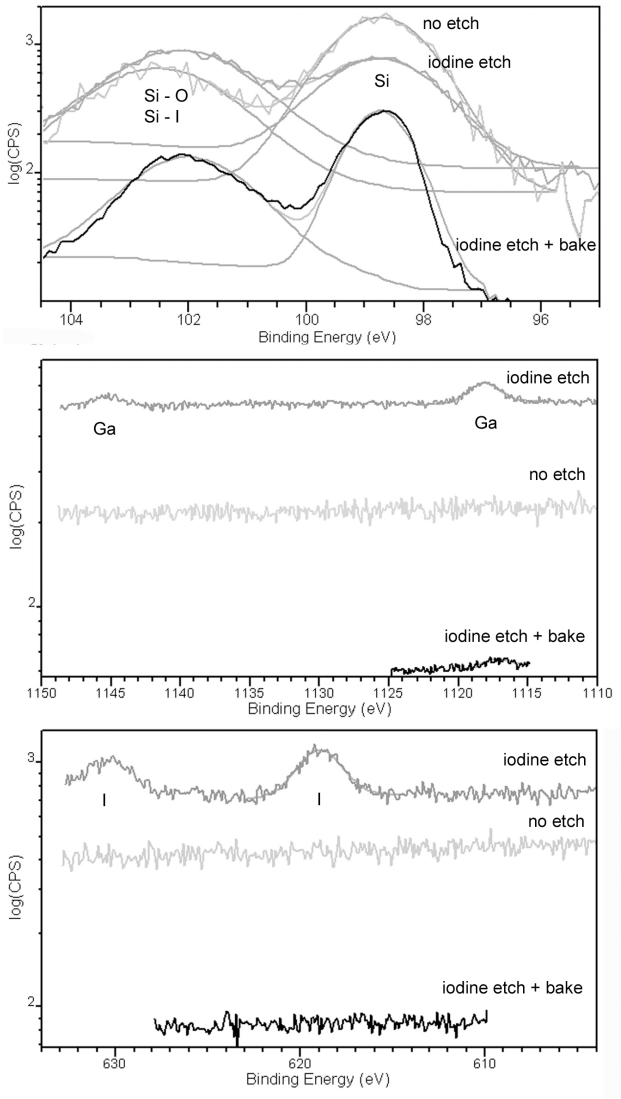

Figure 3.8: XPS of silicon before etching, etched with iodine enhancement and etched with iodine and baked at 300°C. After baking there is an obvious decrease of iodine and gallium content at the surface.

give information about the occupied energy levels of the surface atoms, from which we can deduce the element and its chemical state. The photoemission spectra are presented in Fig. 3.8. To eliminate any charging effects that change the Fermi level in the bulk silicon, we have calibrated all measurements by shifting the silicon bulk component to 98.74 eV [71]. We have measured three samples: a non-etched silicon sample without native oxide removal; an iodine etched sample; and an iodine etched and baked sample. The latter was measured with somewhat higher energy resolution. Although this gives rise to a lower count rate and narrower peaks, we can still draw useful qualitative conclusions. The non-etched sample shows no presence of gallium nor iodine, as expected. Furthermore the peak around 102 eV shows the presence of native oxide. It was reported in Ref. [69] that upon iodine adsorption extra silicon peaks appear about 1 eV higher than the bulk component. These are due to the adsorption of iodine and saturation of dangling bonds, followed by the formation of the Si^{+} and Si^{2+} oxidation states at higher iodine saturation. These experiments were conducted with synchrotron-based photoelectron spectroscopy and visualize small energy shifts that are impossible to resolve in our commercial XPS system. However, we can still draw some useful conclusions from the spectra. After iodine enhanced etching the SiO_2 peak becomes more significant and slightly shifts to the right, whereas an iodine peak appears near 620 eV, suggesting the presence of silicon-iodine bonds. There is also a noticeable amount of gallium in the sample. After baking for two hours at 300°C, the SiO_2 peak weakens again, but a small shift to lower binding energy remains. Furthermore the iodine peak disappears and the gallium peak weakens. This suggest that much of the SiI_x bonds have disappeared during baking, while the chemical nature of the resulting silicon surface layer is slightly altered. The reduction of the gallium component suggests that part of the implanted ions are captured in a surface layer during etching, and desorb with the SiI_x bonds. This result is not in conflict with the SIMS measurements (showing no significant decrease in gallium concentration before and after baking) that are not sensitive to changes in the top surface layer.

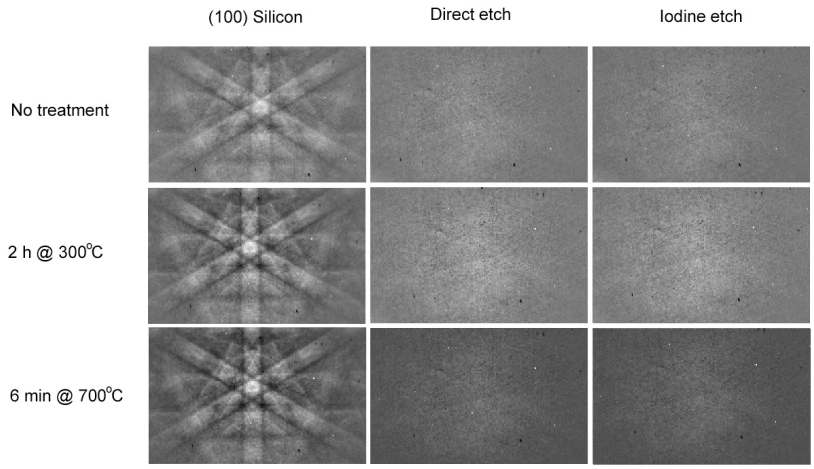

Figure 3.9: EBSD micrographs showing the amorphization after etching. The surface is not recrystallized after a 6 min anneal at 700°C, in contradiction with what we expect from literature.

Amorphization

To verify the crystallinity after etching we have performed electron backscatter diffraction (EBSD)[10] with 5 keV electrons at 70° incidence. As displayed in Fig. 3.9, the diffraction of electrons on lattice plains shows a clear pattern for non-etched crystalline silicon. The same analysis was carried out on directly etched and iodine etched samples, yielding amorphization in both cases. Baking for two hours at 300°C nor a 6 min anneal at 700°C succeed in recrystallizing the etched surface. This is in contradiction with what was previously reported for recrystallization of gallium implanted silicon [57, 58, 61, 75]. However, previous work has not reached implanted concentrations as high as several at%. This high degree of contaminants in the silicon likely inhibits the recrystallization process. However, even though iodine enhanced etched silicon remains amorphous after baking at 300°C the optical losses are reasonably low. Therefore we argue that amorphization is not the dominant effect of optical losses in FIB etched silicon.

[10] See Appendix C

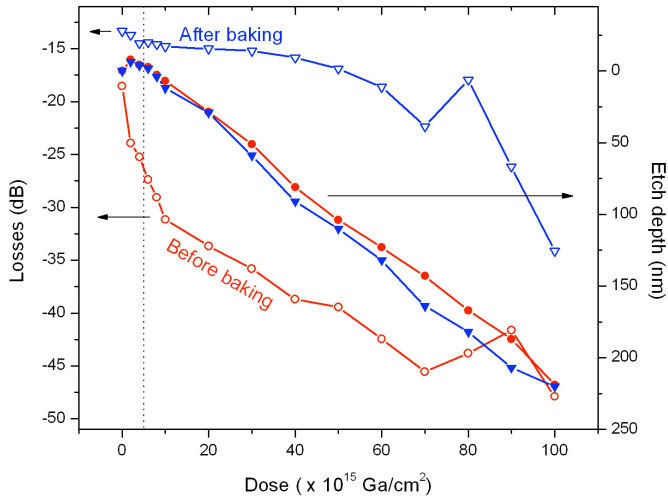

Figure 3.10: The optical losses of the iodine etched sample before (○) and after (▽) baking at 300°C, and the etch depth before (●) and after (▼) baking. The dotted vertical line indicates the dose used in previous experiments.

3.4.4 Calculation of material loss after iodine desorption

Up to now we have used a dose of 5×10^{15} Ga^+/cm^2. Waveguides that are exposed to this dose do not undergo substantial etching. So to investigate the optical losses of more realistic structures etched with iodine enhancement, we have etched the waveguides with higher doses but on sections with an equal length (25 μm). The maximum dose, 1×10^{17} Ga^+/cm^2, etches away the complete 220 nm silicon layer. As lowest dose we have chosen 2×10^{15} Ga^+/cm^2. For each dose we have measured the excess optical losses as well as the depth of the etched region before and after a 2 hour bake at 300°C. The etch depth was measured with an optical profilometer (Veeco Wyko NT3000) after depositing 100 nm of gold. The results are displayed in Fig. 3.10, where the experimental uncertainty for the measurements is illustrated by the size of the data points.

The depth measurement shows that the samples swell at low dose implantation under iodine atmosphere, similar to swelling by direct gallium implantation [36, 65]. However, we expect possible extra swelling due to the formation of adsorbed SiI_x species on the sample surface. The overall etch depth after baking is significantly deeper, which also supports that SiI_x is desorbed from the silicon surface. The reduction of the optical losses in the etched structure

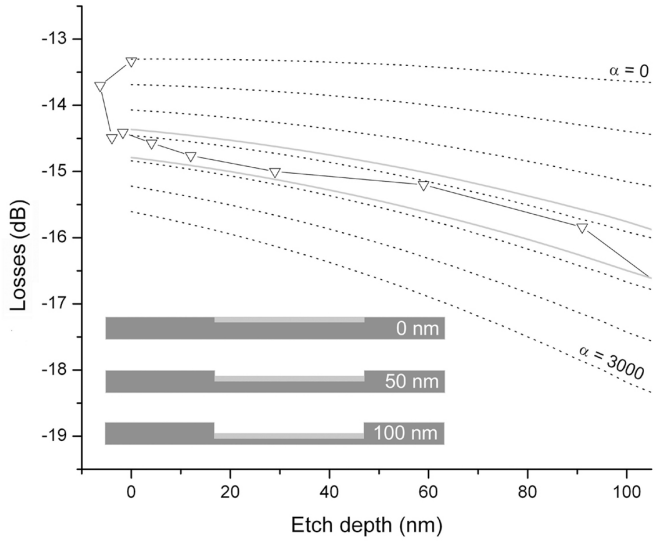

Figure 3.11: Losses as a function of the measured etch depth (▽). The dotted lines represent the simulated losses for a layer with 40 nm thickness and different loss coefficients. A schematic representation of the model is shown in the inset.

by desorbing iodine bonds is obvious. The optical losses after baking remain constant up to an etch depth of about 100 nm.

In Fig. 3.11 the data points from Fig. 3.10 are replotted, but as a function of the measured etch depth instead of the exposed dose. The negative depths are due to swelling at low doses.

We want to extract the average material losses in the implanted section and for that purpose use the following model. From the SIMS data we have estimated the depth of the amorphous silicon layer to be 40 nm. We have assumed that this layer has a refractive index of 3.7, with a variable imaginary part to fit the material losses to the experimental data points. The power transmitted through a 25 μm etched waveguide region, as displayed in the inset of Fig. 3.11, is calculated in a 2D simulation with CAMFR. This was done at a fixed wavelength of 1.55 μm, taking into account 50 modes in the vertical direction. Also displayed are the simulated losses for material loss varying from 0 to 3000 cm^{-1} in steps of 500 cm^{-1}. An offset of -13.3 dB (the zero dose data point from Fig. 3.10) was applied to account for the losses in the fiber couplers. The top dotted line (for $\alpha = 0$) represents the losses only due to mode mismatch between the etched and non-etched region. By fitting we have estimated a

loss coefficient of 1650 $\pm$ 250 cm^{-1} in the amorphized silicon layer. The grey lines represent the simulated losses for a layer with a loss of 1650 cm^{-1} and a thickness of 35 nm and 45 nm.

3.4.5 Conclusion

We have demonstrated that the losses of FIB etched silicon can greatly be reduced by etching with iodine gas enhancement and baking at 300°C. A possible conclusion is that this is caused by removal of silicon iodide species from the surface, and possibly also the removal of some gallium. The loss was reduced from about 3500 dB/cm to 200 dB/cm. The length of practical FIB fabricated devices will usually not exceed 100 μm. The process presented in this section reduces the loss in such typical device from 35 to 2 dB. This result opens many opportunities for the post-processing and prototyping of silicon photonic devices without the necessity of a high temperature treatment.

3.5 Loss reduction by high temperature annealing

The work in this section was done in collaboration with MESA+ Institute in the Netherlands, in the framework of the European Network of Excellence ePIXnet.

3.5.1 Introduction

Another approach the reduce the optical loss of FIB etched silicon is the removal of gallium impurities afterwards. However, this regenerative method requires temperatures above 600°C, which makes them unusable for post-processing of devices. Nevertheless it is a promising technique for prototyping of devices such as photonic crystals.

In this section we present the reduction of the optical losses for annealing temperatures from 400°C to 1000°C. For the highest annealing temperatures losses lower than 100 dB/cm were obtained. Before discussing the results we will first present some specific experimental details. Finally we present a discussion on the effects that dominate gallium depletion during high temperature annealing.

3.5.2 Experimental details

The results in this section were obtained by implantation and etching of both 10 μm wide multi-mode waveguides and 500 nm wide single-mode wire waveguides. The broad waveguides were implanted with a dose of 5×10^{15} Ga^+/cm^{-2} with the same FIB parameters as explained in paragraph 3.3.1. For the etching of the wire waveguides we have used an ion beam current of 48 pA, a dwell time of 1 μs and a pitch of half the beam size. Two different doses were used: 1×10^{16} and 1×10^{17} Ga^+/cm^{-2}, the latter considerably reduces the height and the width of the wire waveguides. By SEM inspection a reduction of 80 nm both in width and in height was observed. The losses were deduced from transmission measurements of wires etched over 6 different length sections (1, 2, 5, 10, 15 and 20 μm). Alignment was done by taking a single SIM image. Annealing was done in a quartz tube furnace in vacuum, for two hours, at a temperature of 400°C, 600°C, 800°C and 1000°C.

3.5.3 Results

	Losses (dB/cm)		
	5×10^{15}cm^{-2} broad waveguide	1×10^{16}cm^{-2} wire	1×10^{17}cm^{-2} wire
not annealed	3520± 90	4110± 180	n.m.
2 h @ 400°C	n.m.	2220± 80	20700± 3500
2 h @ 600°C	n.m.	6190± 70	4740± 1720
2 h @ 800°C	460± 14	160± 70	17670± 1970
2 h @ 1000°C	n.m.	0± 60	-650± 900

Table 3.2: Results for loss reduction by high temperature annealing. Losses drop below 100 dB/cm for 1000°C annealing. (n.m. stands for not measured)

The results are presented in Table 3.2 and in Fig. 3.12. The values for the optical losses in dB/cm were obtained from linear regression analysis of the measurements for different length sections. The broad waveguides were only annealed at 800°C. A clear similarity with the lowest dose wire implantations can be observed when no annealing is applied; wire losses are slightly higher due to the higher dose and because there is a higher mode overlap due to sidewall implantation. The loss in the highest dose implantation before anneal-

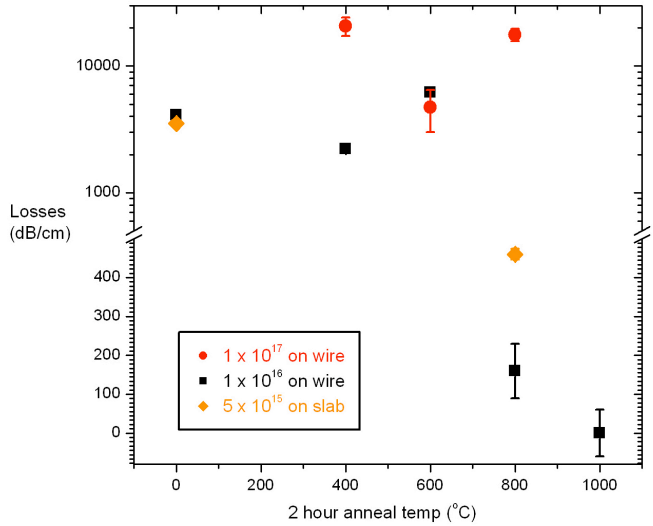

Figure 3.12: Graphical representation of the reduction of optical loss by high temperature annealing.

ing was too high for a reliable measurement. The last column shows large uncertainties, caused by variations of the measured losses between various etch lengths (that were short in this case). Due to the large etch doses these waveguides are etched considerably; therefore modal loss causes a large part of the losses. The negative value in the last row was deduced from linear regression. Although this value is not physical, it demonstrates the loss reduction by high temperature annealing.

An interesting effect can be observed for different annealing temperatures of the same implantation dose. For the lower dose wire implantation a decrease of the loss was observed for 400°C annealing, whereas the loss increases when the sample is annealed at 600°C. A similar effect is apparent in the data for the highest dose implantation, however, the local maximum appears at a higher temperature. A mechanism that can explain both observations is (partial) recrystallization of the silicon and (partial) electrical activation of gallium dopants.

3.5.4 Discussion

A first effect that is likely to cause depletion of gallium impurities from the etched region upon high temperature annealing is diffu-

sion. As mentioned the diffusion of gallium proceeds much faster in SiO_2 than in silicon [55]. This implies that the bottom oxide cladding functions as drain for the gallium atoms from the 220 nm silicon membrane. However, because most gallium atoms are implanted at a depth lower than 60 nm, they must diffuse through the remaining silicon layer before reaching the oxide. Thus deposition of a thin oxide layer on top of the etched structure before annealing would amplify the annealing effect. Therefore we have performed an experiment with broad waveguides, implanted as in paragraph 3.3.1. Two samples were implanted, one was covered with 100 nm of oxide by electron beam evaporation. Both samples were then annealed together for 2 hours at 800°C. This experiment was done twice for verification of the measurements. The results are presented in Table 3.3. We remark that these experiments were performed in a different tube furnace as all the previous ones; the temperature control of this furnace is not absolute, but since both samples with and without oxide are annealed together this does not change our conclusions.

	Losses (dB/cm)	
	$5 \times 10^{15}\text{cm}^{-2}$ broad waveguide without oxide	$5 \times 10^{15}\text{cm}^{-2}$ broad waveguide with 100 nm oxide
2 h @ 800°C run 1	124 ± 27	184 ± 39
2 h @ 800°C run 2	180 ± 55	290 ± 80

Table 3.3: Experiment to investigate the influence of an extra oxide: it inhibits the regenerative effect, thus gallium diffusion in oxide is not the dominant effect.

Both experiments show a significant reduction of the material regeneration when an extra oxide layer is applied. However, it was calculated with a finite element solver that diffusion out of the etched region would be three times more efficient when a 100 nm layer of oxide is applied. Thus it is clear that the extra oxide layer has a inhibiting role in the annealing process. Therefore we are led to believe that the dominant mechanism for gallium removal from the etched region is evaporation into the vacuum. Following line of thought underpins this statement. Due to the low melting point of gallium (29.8°C) the vapor pressure reaches 1 Pa at a temperature of about 1000°C. This pressure is the typical vapor pressure used in the operation of thermal vacuum evaporators for deposition of thin films. For comparison: gold reaches the same vapor pressure at a temper-

ature of 1400°C. In a thermal evaporator the evaporated molecules travel from the heated crucible through the vacuum to the cold walls of the vacuum chamber where they condensate. However, in a tube furnace sample and walls are both hot and the gallium atoms diffuse out of the hot chamber due to pressure differential from the vacuum pump. They finally condensate on the cold region of the quartz tube. A complementary effect that is possibly beneficial for the regeneration of the optical properties is recrystallization and removal of crystal defects.

3.5.5 Conclusion

We have performed high temperature annealing for regeneration of silicon after gallium FIB etching. Annealing at 1000°C reduces the optical losses to below 100 dB/cm. Practically this means that a typical 100 μm device would absorb only 1 dB of light, which is acceptable for prototyping of various devices in silicon. The regeneration is caused by crystal restoration and removal of gallium impurities by evaporation.

3.6 Removal of the FIB damaged layer

As third and final approach to reduce the losses we will discuss the removal of the damaged layer. This should be done in an isotropic, and preferably selective way. The work in this section was also done in collaboration with MESA+ Institute, in the framework of ePIXnet.

Wet etching in concentrated HF is a first alternative. Some tests were performed with etch doses between 1×10^{14} Ga^+/cm^2 and 1×10^{16} Ga^+/cm^2. The samples were submerged in a 40:60 mix of HF:H_2O at room temperature for 15 minutes. By cross-sectioning and SEM inspection we observed that indeed (part of) the damaged layer is removed, however, only for low dose implantations. At higher doses a remaining central region was observed, surrounded by a removed halo due to the beam tails (See Fig. 3.13). In all cases the silicon became very rough after wet etching, which is why this approach was abandoned. A similar technique was reported in Ref. [76] where the FIB etched sample is immersed in ethanol at 78°C for 20 h. It is reported that this technique reduces the optical losses and SEM micrographs do not show an increase of roughness. However, no quantitative loss measurements were presented so comparison with our work is difficult.

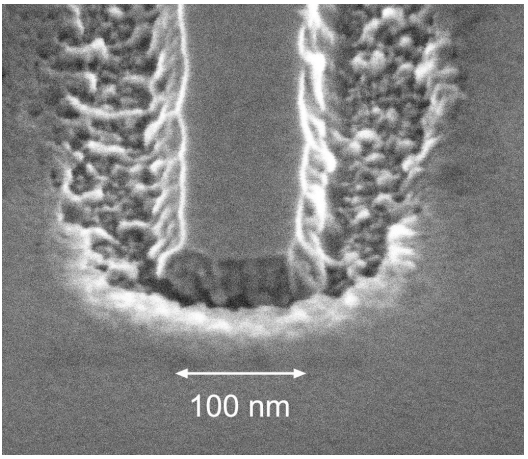

Figure 3.13: FIB implanted line after damage removal in HF: the higher dose implanted central region does not etch; only the region implanted by the beam tails is etched and becomes rough.

A second approach is dry etching in a plasma. This was performed on the wire waveguide samples with implantation dose of 1×10^{16} Ga^{+}/cm^{2}. Two samples were etched in a reactive ion etch plasma of CHF_3/O_2 (flow 25/5 sccm, 10°C, 480 V bias, 60 W) to remove 30 nm of silicon from one sample and 50 nm from the other. The optical losses are displayed in Table 3.4. The losses have somewhat decreased, but even after removal of 50 nm a relatively high loss remains.

	Losses (dB/cm)
	$1 \times 10^{16} cm^{-2}$ wire waveguide
before removal	4110 ± 187
30 nm etch	3380 ± 211
50 nm etch	1070 ± 200

Table 3.4: Optical losses after plasma etch removal of the damaged layer. Relatively high losses remain.

Both presented methods for removal of the damaged silicon layer after FIB etching yield moderate results, thus these techniques are not optimal for prototyping or post-processing.

3.7 Conclusions

In this chapter we have summarized the work performed on the reduction of the optical losses of FIB etched silicon. The first technique is a preventive technique: chemical etch enhancement using iodine gas. It was found that the loss in a typical 100 μm device can be reduced to 2 dB by annealing the samples at a relatively low temperature. This makes the technique suitable for post-processing of silicon photonic devices that feature bonded III-V material or metal contact pads. FIB is the only technique capable of etching sub 100 nm features in a fully processed device. Our work enables low optical losses in these post-processed devices.

The other techniques that we have proposed are regenerative: the structure is directly milled in silicon and damage and impurities are removed afterwards. The most successful regenerative technique is high temperature annealing. We have demonstrated that the optical losses can be reduced to lower than 1 dB for a typical 100 μm long device, which makes the technique appropriate for prototyping of purely passive silicon photonic structures such as photonic crystals with 3D geometry.

The work in this chapter was the subject of one publication in scientific literature (Appendix A.2 #6).

Chapter 4

Fabrication of silicon photonic devices

After introducing techniques to reduce the optical losses in FIB etched silicon, in the previous chapter, this chapter will present fabrication strategies and fabricated devices. First we discuss two fabrication approaches: FIB patterning by iodine enhanced etching with alumina hardmask, and FIB lithography that exploits the combination of FIB and plasma etchig. Then we present fabrication and design of various grating couplers, and we elaborate on FIB etched slot structures in waveguides and racetrack resonators. The fabrication of standard shallow grating couplers was done to evaluate our fabrication technology, whereas the fabrication of other devices was done for prototyping purposes.

4.1 Fabrication strategies

4.1.1 Iodine enhanced FIB patterning with hard mask

It was already mentioned that the size of a focused ion beam can be smaller than 10 nm, which makes FIB etching an interesting technique for direct patterning of nanostructures. However, these low beam sizes are only attainable for low ion beam currents that are often not practicle because material removal is slow and imaging with reasonably low noise is difficult. Higher ion beam currents will give rise to a larger beam size. This, in combination with the Gaussian beam shape, complicates the fabrication of sharp edges

and straight sidewalls, especially when etching of sub-micron features is envisaged. The effects of the beam tails become even more pronounced when iodine enhancement is used to reduce the optical losses, because the enhancement rate is higher for lower beam currents. Therefore we propose the use of a hard etch mask, as explained in the following paragraphs.

Hard etch mask / Protective layer

A first reason for using an extra layer is protection of the underlying silicon during alignment. Since silicon is easily damaged by impinging gallium ions it is not recommended to use ion microscopy for the imaging and alignment on sensitive parts of a sample when no protective layer is applied. A possible way to circumvent this without mask is to use the non-destructive electron beam for imaging and alignment, and use the ion beam only for the etching. This requires careful alignment of the coincidence point of ion and electron beam on the sample surface. Both beams (at an angle of 52°) have to coincide in the eucentric point (the tilt center of the stage). In practise this is done by making an ion and electron beam image of a feature and using beam deflections and sample height corrections to bring the feature in the center of the field of view. Because ion imaging is involved in this procedure, it has to be conducted on a non-sensitive part of the sample, for instance away from the waveguides and grating couplers. However, the eucentric point alignment is not preserved by horizontal translations because the sample surface is never perfectly horizontal. This makes that the alignment procedure without protective layer has a precision that is typically > 1 μm. More precise alignment requires ion imaging of the sensitive parts of the sample, and therefore requires a protective layer. When appropriate alignment techniques are used, the precision is only limited by the ion imaging resolution, which is smaller that 10 nm.

A second reason for using an extra layer is to have a hard etch mask that can help to reduce the effects of the Gaussian-like beam shape, which makes the etching of small holes with vertical sidewalls difficult unless a membrane approach is used [77]. Similar to what is done for plasma etching, the sidewall of etched trenches can be made more vertical by using a top material layer that etches slower than the substrate material and that can selectively be removed afterwards.

Both requirements - protection and low etch yield - are met by a 50 nm alumina layer (i.e. amorphous Al_2O_3) that can be deposited by electron beam evaporation of alumina in an oxygen atmosphere. Alumina has a low etch yield for 30 keV gallium bombardment (0.08 μm^3/nC as compared to 0.22 μm^3/nC for silicon); the selectivity is further increased when iodine enhancement is used. Furthermore the projected range of impinging 30 keV gallium ions in alumina is about 15 nm; therefore a 50 nm layer is sufficient to stop the bombarding ions up to considerably high doses. Fig. 4.1 shows the propagation loss in 10 μm wide silicon waveguides that were implanted and etched with 10 keV and 30 keV gallium atoms, as compared to 30 keV gallium implantation in a waveguide covered with a 50 nm protective layer of alumina. No significant losses were measured in this experiment, even though the alumina layer was not removed. Two conclusions can be drawn from this experiment. Firstly that a 50 nm alumina layer on silicon offers adequate protection for gallium implantation and sputtering. Secondly that damaged and gallium implanted alumina does not significantly absorb light at 1.55 μm. We will come back to these conclusions in Chapter 5, where we discuss FIB trimming.

Because of these results, and because it was observed that the thin alumina layer hardly changes the propagation losses of silicon waveguides, nor the coupling efficiency of grating couplers (see later), the alumina layer was not removed for most of the experiments in this work. However, for some components it may be necessary to remove the protective layer: e.g. slot ring resonators for biological sensing applications might need a silicon surface treatment for adequate bonding of bio molecules. Therefore we have developed a selective alumina removal technique that does not etch silicon nor oxide: a wet chemical etch bath of Cr_2O_3 and H_3PO_4 (4 g of Cr_2O_3 in 20 ml of H_3PO_4). At room temperature the etching is slow, but by heating the green viscous liquid up to a temperature of 70°C the 50 nm layer can be completely removed in a couple of minutes.

Another important advantage of alumina as hard mask is its amorphous nature. Most other etch mask candidates, such as Cr or Ni, are metallic and will form grains in the thin deposited layer. Because upon gallium impact the sputter yield depends on crystal orientation these layers become rough. Thus if one wants to do a shallow silicon etch with vertical sidewalls (such as for a shallow grating coupler, see later) a polycrystalline etch mask will yield a rough trench bottom, which is undesirable. Therefore, in spite of

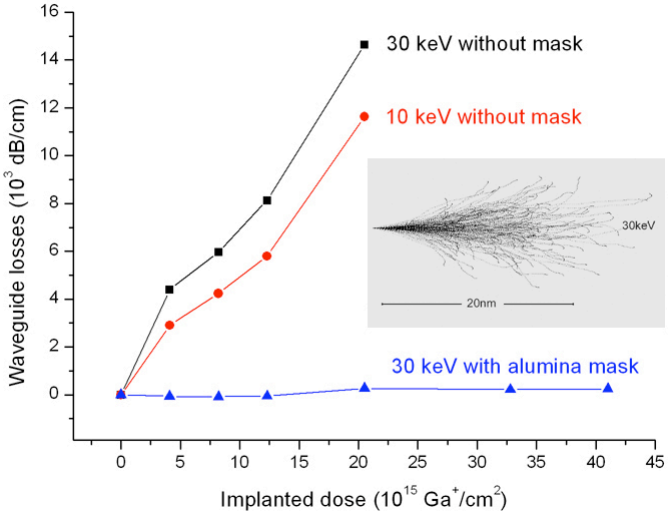

Figure 4.1: A 50 nm alumina layer offers adequate protection against gallium damage, as no significant propagation losses were measured up to relatively high doses. The inset shows the trajectories of gallium atoms in alumina; none of the 500 displayed trajectories penetrate deeper than 30 nm.

moderate charging of the non-conductive alumina layer, it is to be preferred over metallic hard mask layers. Furthermore, because of its ease of deposition and selective removal combined with the excellent protective capacity, alumina was identified as a suitable material for FIB etching of photonic devices.

One- versus two-step etch process

Two different strategies can be used for the FIB etching of silicon with the help of the alumina hard mask. If one is interested in etching through the entire (220 nm thick) silicon film, the importance of trench bottom flatness is usually negligible. Therefore a one-step etch process can be used, either by direct or iodine enhanced FIB milling followed by furnace annealing or hotplate baking (Fig. 4.2(a)).

However, if one wants to etch a relatively wide and shallow trench or hole (e.g. for a shallow grating coupler, see later), flatness of the bottom is difficult to control if a homogeneous surface dose is applied (Fig. 4.2(b)). This is caused by the gaussian beam tails, sputter yield dependance on the angle of incidence, and be-

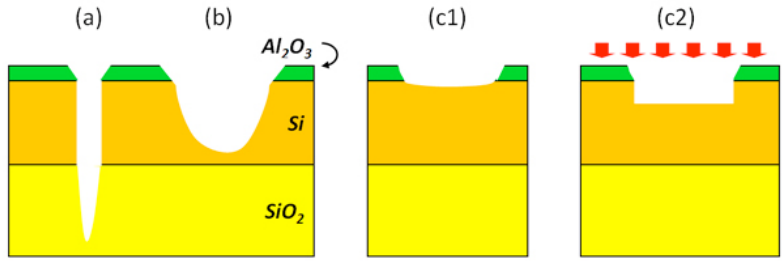

Figure 4.2: Schematic representation of one- and two-step etching. (a) A one-step etch procedure is adequate for etching through the entire silicon layer, (b) but not for shallow trenches. (c) A two-step procedure is more appropriate for shallow trenches: (c1) selective mask etch, (c2) broad-area etch.

cause of the large difference in sputter yield between the hard mask and the substrate (especially in the case of iodine etch enhancement). Therefore a two-step etch procedure is more desirable: the first etch step to selectively remove the hard etch mask in a given area (Fig. 4.2(c1)); the second step to etch the silicon in the opened regions (Fig. 4.2(c2)). In this work the selective mask opening was done with trifluoroacetamide (TFA) gas enhanced FIB etching. The second etch step can in principle be performed with any broad-area etch technique such as plasma etching (see next section on ion lithography), but can just as well be done with FIB etching on an area that is larger that the opened mask area. This procedure was used to etch shallow grating couplers, as explained later in this chapter.

Alignment accuracy

Some of the devices presented in this chapter do not require precise alignment. E.g. the etching of grating coupler slits (see further) on broad waveguides requires only a correct relative placement of the slits to ensure the correct grating period. If all grating lines are etched simultaneously their placement is precise to one 4096th part of the writing field (if the 12 bit FEI pattern generator is used); for a typical field of 15 μm wide this leads to a slit placement accuracy of about 4 nm. Higher relative placement accuracies can be obtained by using a 16 bit patterning board (e.g. Raith). The absolute placement

accuracy of the grating slits on the broad waveguide is not stringent if their length is chosen greater than the width of the waveguide.

Other applications such as the etching of a slot in a pre-fabricated waveguide or stitching of several writing fields require more precision. Thanks to the protective alumina mask one can make an ion microscopy image on which the structures can be aligned visually or by image recognition. A 50 pA, 15 μm wide ion image of alumina on silicon yields a overlay placement accuracy of better than 50 nm for visual placement by an operator with moderate experience level. By using image recognition techniques (available in the Raith lithography extension) this can be improved. Because one can make images on pre-fabricated structures without inducing any optical loss, the overlay placement accuracy is only limited by image quality. Therefore overlay placement errors of less than 10 nm can be achieved.

Limitations

It was already mentioned that a small ion beam diameter requires a small ion beam current. This brings about a trade-off between the high-resolution patterning potential and fabrication speed of FIB patterning. The highest ion beam current available in the FEI ion column at 30 keV is 20 nA, which typically etches one cubic micron per second, regardless of whether iodine enhancement is used or not. However, due to a beam size of about 200 nm the patterning resolution is very low. The smallest beam current that was used in this work is 10 pA, corresponding to a beam size of about 10 nm. The thinnest slits obtained in this work are displayed in Fig. 4.3: 40 nm wide slits etched in a silicon ring resonator with iodine etch enhancement without alumina etch mask. The iodine gas needle in this process was positioned left of the etch site, which caused the asymmetry of the slits. This stresses the importance of gas flow control for the exploration of the ultimate patterning potential with iodine gas enhancement.

4.1.2 FIB lithography

Another approach is the patterning of a sacrificial layer by FIB milling (without gas enhancement) and pattern transfer into the silicon with a conventional etching technique such as plasma etching. This approach combines elements from direct FIB patterning from the previous paragraph and electron or ion beam lithography by use of a resist layer. The advantage over using a resist is that the patterned sac-

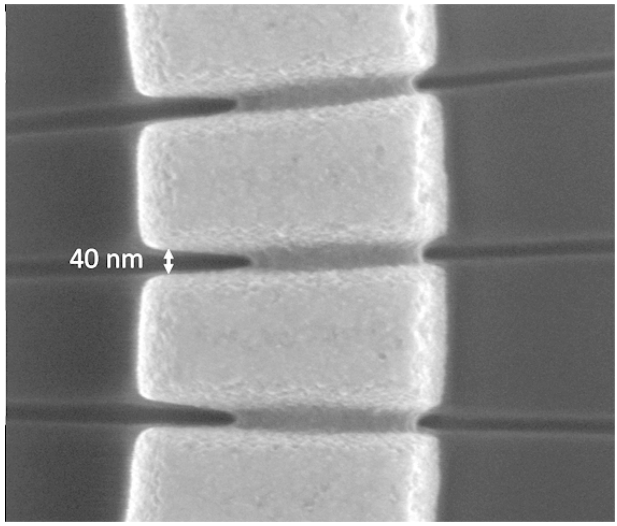

Figure 4.3: The smallest structures obtained with iodine etch enhancement are 40 nm wide slits in a ring resonator.

rificial layer can be deposited by evaporation techniques and therefore preserves topography. Therefore one can easily align on prefabricated structures and define patterns close to existing structures such as ridge waveguides, which is not possible with spun-on layers such as most resist materials.

This fabrication strategy was developed for the fabrication of grating couplers in a silicon waveguide, as described later. For this application the shape of the slit bottom is crucial, and we aimed at avoiding the residual losses of the iodine enhanced etching approach.

Fig. 4.4 shows the proposed process flow with a ceramic-metallic layer stack. In a first step the thin Ti layer is patterned by direct FIB milling; the second step opens the alumina protective mask by wet etching; and in the final step the pattern is transferred into the silicon by plasma etching. This process is difficult to perform with a single sacrificial layer because in that case some silicon is damaged by the impinging gallium atoms, which makes plasma etching difficult. Therefore a 50 nm alumina layer is deposited as a protective intermediate layer to protect the silicon. The alumina can be opened by wet etching in a mix of 4 g of Cr_2O_3 in 20 ml of H_3PO_4 at 70°C for 20 to 30 seconds.

The process was optimized both for the etching of grating couplers and slots in waveguides and rings. Etching through the Ti

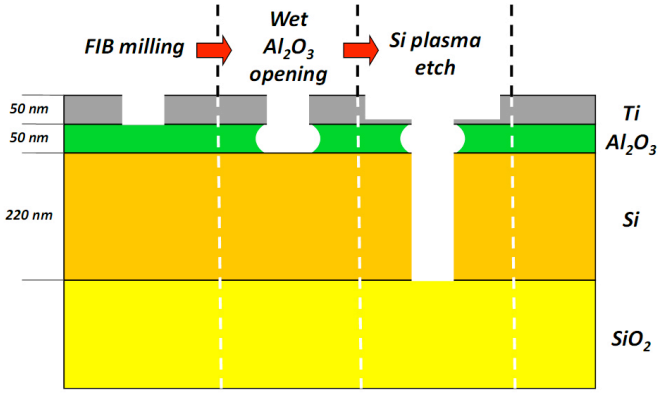

Figure 4.4: Process flow for the developed FIB lithography technique: milling of Ti, wet etching of alumina, and plasma etching of the silicon.

layer was performed with the Raith lithography system because of its superior calibration and alignment capabilities. The etch process is conducted with only a limited number of loops to avoid excessive writing times.[1] Usually a low number of loops would lead to trenches with angled bottoms. However, because the sputter yield of alumina is 4.5 times lower than titanium the alumina acts as etch stop layer and this does not occur. Furthermore, optimization of the dose needed to open the titanium layer is straightforward because the difference in secondary electron yield gives a clear contrast; alumina appears bright in the SEM image once the titanium layer is perforated. Depending on the desired trench width and the ion current the 50 nm titanium layer is etched with a ion dose of 1.25-12.5$\times 10^{17}$ Ga^+/cm^2, spread over 10 loops.

Fig. 4.5 shows a cross-section of a grating slit etched with the presented process. The resulting sidewalls are nearly vertical and the bottom is flat. The plasma etching was performed by inductively coupled plasma (ICP) etching with SF_6 and O_2 gas with a flow a 20 and 10 sccm respectively, a pressure of 5 mTorr, RF power of 100 W and ICP power of 5 W, and a sample stage temperature of 15°C.

A similar process was optimized for the etching of slots in prefabricated waveguides and ring resonators, as explained later. Fig. 4.6 depicts three slots etched in a silicon slab for dose optimization.

[1]The Raith system has problems to cope with many loops because it was designed as an electron beam tool that deposits the complete dose in a single loop.

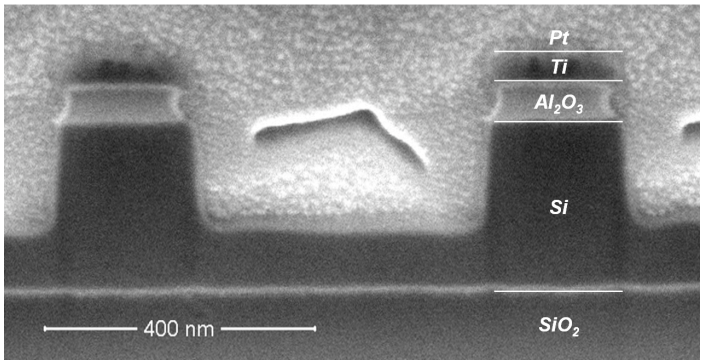

Figure 4.5: Cross-section of a trench etched with FIB lithography. The trench bottom is flat and the sidewalls are nearly vertical and smooth.

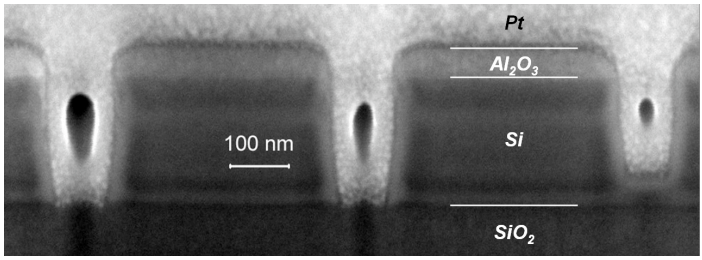

Figure 4.6: Cross-section of three slots in a silicon slab, etched with FIB lithography. The titanium layer is completely removed during the plasma etching.

The ICP process used in this case has 200 W RF power (all other parameters are identical). In this case the titanium layer is completely removed during the plasma etching.

4.1.3 FIB prototyping versus volume production

Similar to electron beam writing, FIB is a serial writing technique and therefore inherently slow and not adequate for high volume manufacturing of devices. However, for reasons of speed and flexibility, serial techniques are attractive for prototyping. Both presented approaches of FIB fabrication of silicon photonic devices offer superior flexibility over resist-based technologies such as electron beam lithography because they can be used to alter existing devices, which opens opportunities for device modifications and trimming. If FIB is used to modify deep-UV pre-fabricated devices one could even imagine a medium volume manufacturing scheme. In combi-

nation with direct FIB patterning this fabrication scheme enables the fabrication of angled trenches and slits, and structures with more complex 3D geometries, which is not possible with conventional planar fabrication technologies such as optical lithography. Furthermore, since temperatures in excess of 300° are not required for the presented iodine enhanced etching technique, this fabrication strategy can be adopted for small changes to finished devices that potentially contain metals, polymers and III-V semiconductors.

4.2 Grating couplers

One of the problems of a high index contrast platform for integrated circuits such as silicon on insulator (SOI) is the difficulty of coupling between the tightly confined silicon optical mode (with typical dimensions of 200 nm $\times$ 500 nm) and the relatively large mode in a standard single mode optical fiber (typically 10 μm $\times$ 10 μm). Several in-plane approaches with low losses were proposed such as inverted tapers and three dimensional tapers. However, out-of-plane coupling with diffractive gratings is attractive because the optical mode can be accessed anywhere on the wafer; furthermore they make facet polishing unnecessary. Due to the high index contrast in the silicon on insulator (SOI) platform, gratings can be made reasonably efficient and compact [64]. As depicted in Fig. 4.7 it is advantageous to use a nearly second order grating to avoid reflections but still exploit out-of-plane diffraction. The conventional grating design consists of shallowly etched rectangular trenches in a broad silicon waveguide. However, due to diffraction into the substrate and mode mismatch the experimental fiber-to-waveguide coupling efficiency is limited to about 25%. Furthermore this design requires a long adiabatic tapering section from the single mode (500 nm wide) silicon waveguide to a 10 μm wide waveguide. Most of these hurdles were recently addressed: curved grating slits make the adiabatic taper obsolete [78]; and better design of the grating slits greatly increases the efficiency of upward diffraction. The latter will be discussed in more detail in this paragraph. Various grating concepts were fabricated with FIB for prototyping purposes. This rapid design verification approach is important because adoption of new fabrication strategies for volume production technologies is expensive and slow. Therefore it is primordial to test the feasibility of new concepts with a rapid and flexible fabrication technology such as FIB. Furthermore in situ FIB fabrication of grating couplers is also attrac-

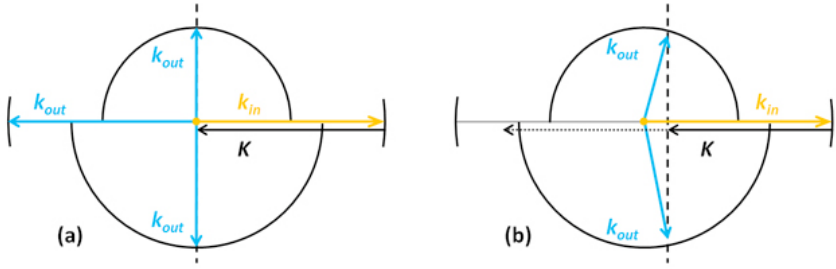

Figure 4.7: Bragg diffraction diagrams for incoming light with k-vector k_{in} and grating with reciprocal period K: (a) for a second order grating there is reflection in the waveguide; (b) by choosing e.g. a slightly longer grating period the second order reflection is avoided but the out-of-plane diffraction remains.

tive as failure analysis technique: it can be used to make grating couplers on any waveguide on an integrated circuit to access the optical signal.

In this section we present the fabrication of a shallow grating coupler both by FIB patterning and by FIB lithography for technology evaluation purposes; we discuss the design and prototyping of a slanted grating coupler with experimentally measured efficiency of 46%; we present the prototyping of a gold grating coupler; and we discuss the fabrication of gratings on a silicon overlay structure.

4.2.1 Shallow grating coupler

In previous work shallow grating couplers were fabricated with 248 nm and 193 nm deep-UV lithography and inductively coupled plasma (ICP) etching and optimized the parameters for optimal coupling efficiency (25% and more [2]) and 1550nm operation [64]. These gratings consist of 70 nm deep and 315 nm wide trenches with a period of 630 nm. To evaluate the potential of the proposed fabrication strategies we have tested whether this grating structure can be duplicated without efficiency penalty.

In this paragraph we will compare different FIB etching schemes and optimize for lowest ion damage and best coupling efficiency. First grating couplers were etched directly into silicon waveguides using different acceleration voltages, with and without gas enhancement. The efficiencies of these couplers are low, which supports the need for a hard mask as explained previously. The etching scheme

with alumina hard mask was used in combination with two etch steps, as well as the FIB lithography approach in combination with ICP etching. Both fabrication approaches have yielded devices with comparable fiber-to-waveguide coupling efficiency as the deep-UV fabricated couplers, which supports that reasonably low losses were obtained.

Experimental details

To determine the coupling efficiency we use a fibre-to-fibre transmission measurement for TE-polarized light from a tunable laser. The structure consists of an input coupler, a 10μm wide waveguide and an output coupler. We assume that both FIB fabricated couplers are identical. The bottom oxide cladding was 1 μm thick for the mask-less and alumina mask experiments, and 2 μm for the FIB lithography experiment.

Fabrication without hard mask

A first approach is to use FIB to directly etch the grating in Si. This was done with 10 keV and 30 keV Ga^+ ions, with and without iodine as selective etchant. The results are presented in Fig. 4.8. Each curve in the graph is the most efficient from a set with different etch doses. The dose variation ranged from 4×10^{16} to 42×10^{16} Ga^+/cm^2 in the case of direct etching and 0.6×10^{16} to 3.7×10^{16} for the iodine etching process. The 30 keV etches were performed with a beam current of 50pA, the 10 keV etches with a current of 120 pA for the etching without gas, and 50 pA for iodine etching. By making cross-sections we verified that the expected optimal grating profile was covered in this dose range. We strived for the optimized gratings of previous work: 25 lines with a width of 315 nm, a spacing of 315 nm, and an etch depth of 70 nm. But investigation of the cross-sections showed that the structures are more 'rounded' than the gratings fabricated with conventional techniques. This is caused by the gaussian [36] profile of the beam. We have performed finite difference time domain (FDTD)[2] simulations with ellipse-like grating slits rather than square ones, and showed that there is little effect on the maximum obtainable efficiency if etch depth and filling factor are optimized. Fig. 4.8 shows that the gratings fabricated without iodine are inefficient, although they have cross-sections that look more or less like the optimal ones.

[2]We refer to Appendix D for more information on simulation techniques.

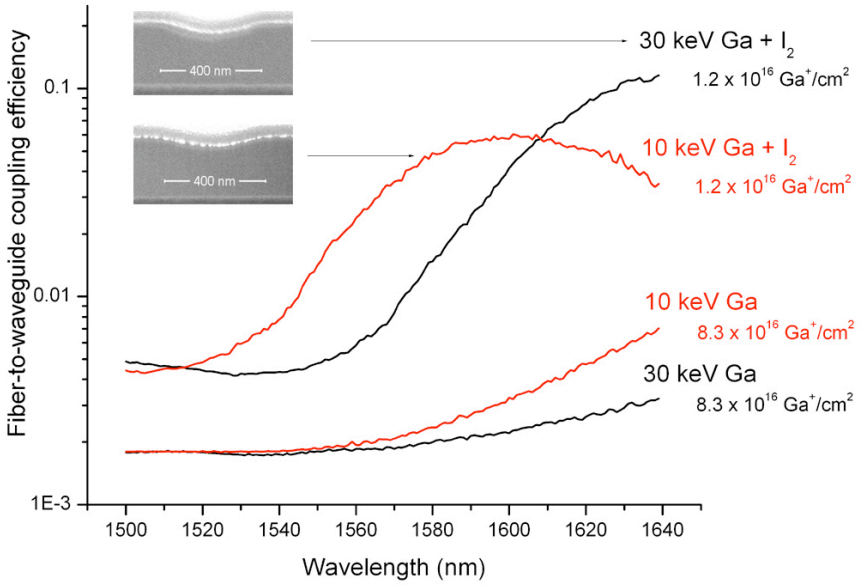

Figure 4.8: Shallow grating couplers etched with FIB in SOI waveguides, without using a hard mask. By using iodine as etch enhancement gas the coupling efficiency is improved. However, they are still 2 to 3 times less efficient than deep-UV fabricated gratings. The top left inset shows FIB cross-sections through grating slits etched with iodine, with 10 and 30 keV ions.

This low efficiency of directly etched gratings was already noticed [27] and is caused by the ion induced damage in the material. This is also clear form Fig.4.9 where the transmitted and upwards diffracted power fraction is measured for gratings etched with different doses. This was done by direct FIB milling of a grating between two existing standard gratings. Light was coupled into a standard grating and the optical power coupled out of the FIB fabricated coupler and the standard coupler behind the FIB coupler was measured (we have assumed zero reflection from the FIB fabricated coupler). The detrimental effect of material damage and implantation is pronounced in gratings since the damaged material near the bottom of the slits has a large overlap with the traveling optical wave. It is therefore unlikely that the presented spectra of directly milled

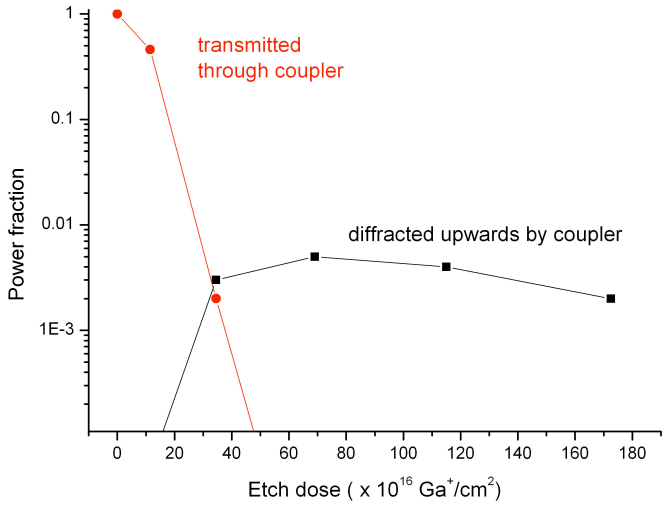

Figure 4.9: Measured optical power that is transmitted through and coupled up by directly milled gratings for various etch doses. The efficiency is never more than 1%.

gratings in Fig. 4.8 show a peak outside the wavelength range of the measurements.

Fig. 4.8 also shows that the gratings etched with iodine are much more efficient (about a factor of 20), although the cross-section does not look less 'rounded' (see inset Fig. 4.8). We have measured a maximum fiber-to-waveguide coupling efficiency of about 11%. This is still far below the efficiency of gratings made with classical etching techniques (about 25% [2]). The reason for this is the non-optimal dimensions of the gratings. The inconvenience of the enhanced etching process is the loss of dimensional control: one cannot etch 90° sidewalls nor easily control the width of a hole. This is why we chose to work with a hard etch mask rather than to further optimize the direct etching with iodine.

Fabrication with hard mask and iodine enhanced FIB etching

Fig. 4.10 shows the coupling spectra for various fabricated couplers. As mentioned before (paragraph 4.1.1) the best results for shallow trench etching are obtained with a two step etch strategy. In a first step rectangular grooves are etched with TFA gas enhancement to open rectangular regions in the alumina mask. Alignment is not crucial because the rectangles are longer than the waveguides. Af-

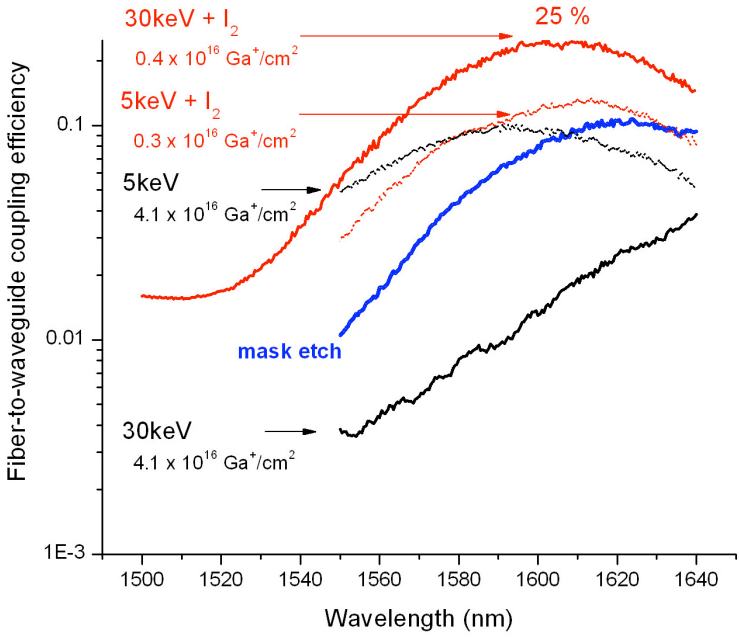

Figure 4.10: Gratings fabricated with alumina mask, using a two step etch process. The thick curve shows the coupling efficiency of a grating etched by only the first mask-etch step. The second step was varied (5 keV and 30 keV, with and without iodine), and the most efficient gratings were produced with 30 keV ions and iodine etch gas.

terwards one can use classical etching techniques, such as reactive ion etching, to etch the silicon, but for process simplicity and speed we chose to do the second step also with FIB. The thick line in Fig. 4.10 shows the coupling efficiency that was measured after performing only the first mask-opening etch step. It is clear that this already couples a reasonable amount of light into the fiber. This can be explained by making a cross- section through the structures, as displayed in Fig. 4.11(a): part of the silicon is etched. The reason for this is the limited etch selectivity between alumina and silicon, which is about 1:1 for TFA gas enhancement (considering that alumina etches about 3 times slower than silicon without gas enhancement this is a substantial improvement). Furthermore it was observed during dose optimization of the first etch step that for somewhat lower doses (but sufficient to etch through the alumina) an apparently hard surface layer remains on the silicon. This was noticed

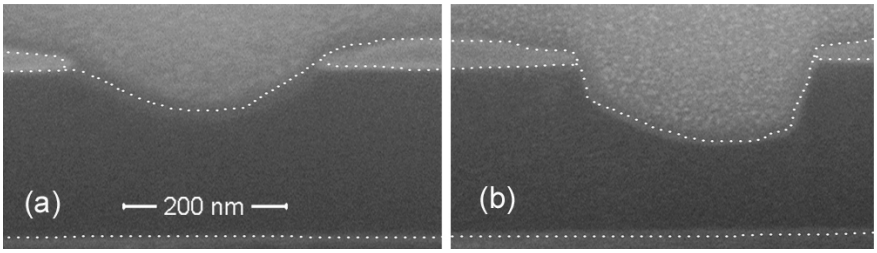

Figure 4.11: A cross-section through two slits of a grating etched (a) with TFA gas for mask breakthrough, and (b) followed by a second etch step with iodine gas and 30 keV ions (0.9×10^{16} Ga^+/cm^2). White dotted lines were added to increase the contrast.

because no silicon etching occurred in the second etching step. Increasing the dose of the mask etch step to 12×10^{16} Ga^+/cm^2 solves this problem (30 keV, 50 pA).

For the second etch step one big rectangle is defined over the etched grating lines with the help of a single ion microscopy alignment scan. Some of the unprotected silicon is hereby damaged, but this causes no problems since the damaged region is removed in the subsequent etch step. Fig. 4.10 shows four different processes for the second etch step: 30keV and 5keV, with and without iodine. Direct etching with 30 keV ions and no gas gas (4.1×10^{16} Ga^+/cm^2; 300 pA) produced a non-efficient coupler as expected. Because of the lower damage depth of the 5 keV etching without gas (4.1×10^{16} Ga^+/cm^2; 70 pA), the produced gratings were more efficient than the 30 keV etch without gas, but we could not reach much higher efficiencies by adding iodine to this process (0.3×10^{16} Ga^+/cm^2; 70 pA). This might be caused by lower chemical enhancement at lower acceleration voltages. The best results were obtained by using iodine and 30 keV etching; the best fabricated couplers ($0.4\times$ 10^{16} Ga^+/cm^2; 50 pA) have a coupling efficiency of 25%. This result was obtained from an optimization of the etch dose of the second etch step. The measured coupling efficiencies and peak wavelengths of this optimization process (with six fabricated coupler pares) are presented in Fig. 4.12 as a function of etch dose. Except for the two gratings with highest dose one can notice a trend of the peak wavelength moving to shorter wavelengths as the etch depth increases, which is in accordance to Bragg diffraction (Fig. 4.7). Deeper etched slits correspond to a lower effective index of the propagating mode and thus a lower wavelength to maintain the same k-vector. The two gratings

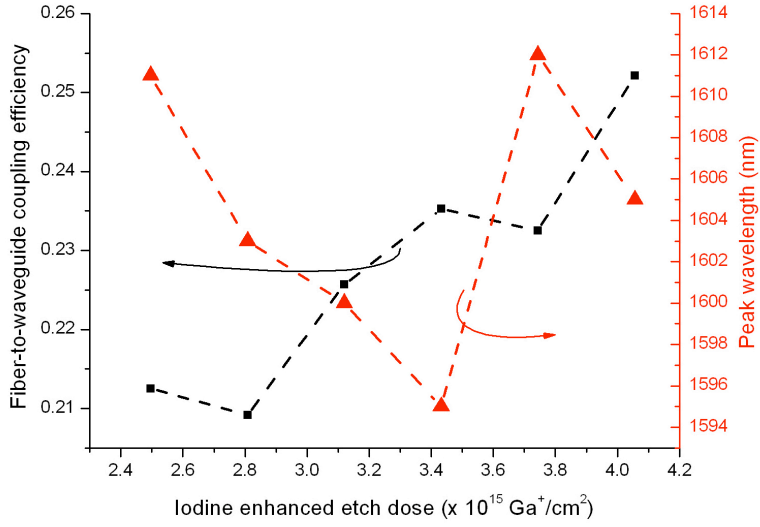

Figure 4.12: Dose optimization of the second etch step yields varying coupling efficiencies and peak wavelengths. The large jump in the curve for the peak wavelength corresponds to a different sample.

with highest dose were etched and measured in a different experimental run; possibly with slightly different alumina thickness or fiber tilt angle. The maximum obtained efficiency of 25% is equivalent to what was previously obtained with conventional techniques. The total etch time for one grating coupler is about 5 minutes.

Fig. 4.11(b) shows a cross-section of a grating that was etched with 30 keV ions and iodine, with a dose of 0.9×10^{16} Ga^+/cm^2. The asymmetry of the etched trench could not be removed by changing the scanning direction of the ion beam, so it is likely to be caused by the directional gas injection of our system.

Fabrication with FIB lithography

The same grating couplers were also fabricated with FIB lithography, with a process flow as described in Fig. 4.4. 50 nm of alumina and 50 nm of titanium were deposited by electron beam evaporation. Then the titanium layer was etched with FIB. 25 rectangles of 325 nm were etched with a beam current of 150 pA (30 keV) and a dose of 2.25×10^{17} Ga^+/cm^2 spread over 10 loops, using the Raith lithography software. Alignment of the rectangles on the pre-

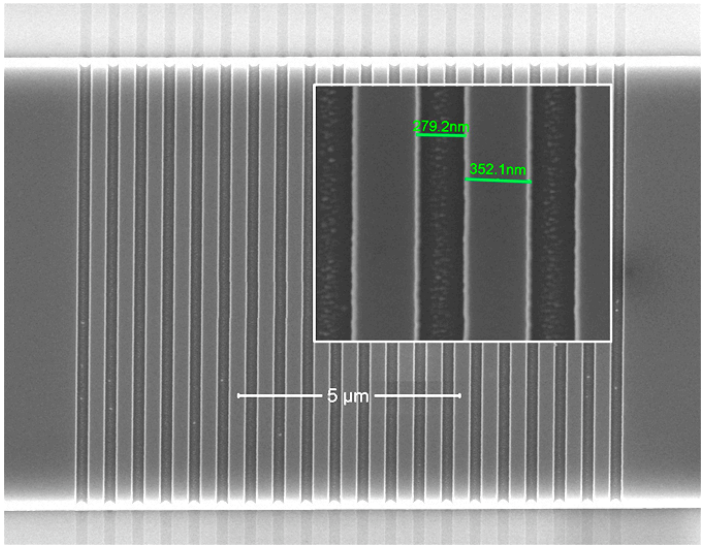

Figure 4.13: Shallow grating coupler etched by FIB lithography in a pre-fabricated waveguide. The inset shows a higher magnification image of the same coupler. The etched slits are 35 nm too narrow. The roughness is higher than deep-UV fabricated or directly FIB etched gratings due to the non-optimized ICP etch process. Nevertheless, this does not noticeably contribute to the coupling efficiency.

fabricated waveguides was done by imaging with the ion beam, which is safe due to the protecting alumina layer. After this titanium opening etch the alumina stopping layer was opened by etching for 20 s in a mix of 4 g of Cr_2O_3 in 20 ml of H_3PO_4 at 70°C. Then the silicon trenches were etched by ICP etching with SF_6 and O_2 gas with a flow of 20 and 10 sccm respectively, a pressure of 5 mTorr, RF power of 100 W and ICP power of 5 W, and a sample stage at 15°C. The etching time for 70 nm deep slits was 15 s. Finally the remaining titanium was removed in a piranha etch bath at 120°C (1:3 mix of peroxide and sulfuric acid) and the alumina layer was removed in the same mix as previously. The resulting grating is shown in Fig. 4.13 where the inset zooms in on some grating lines. The etched trenches are narrower than the aimed value of 315 nm, which can be corrected by applying an offset in the first etch step and by increasing the time of the wet alumina opening.

The coupling efficiency of these grating couplers (two identical ones on a waveguide) was measured with polarized light from a tunable laser and compared to the efficiency of deep-UV fabricated

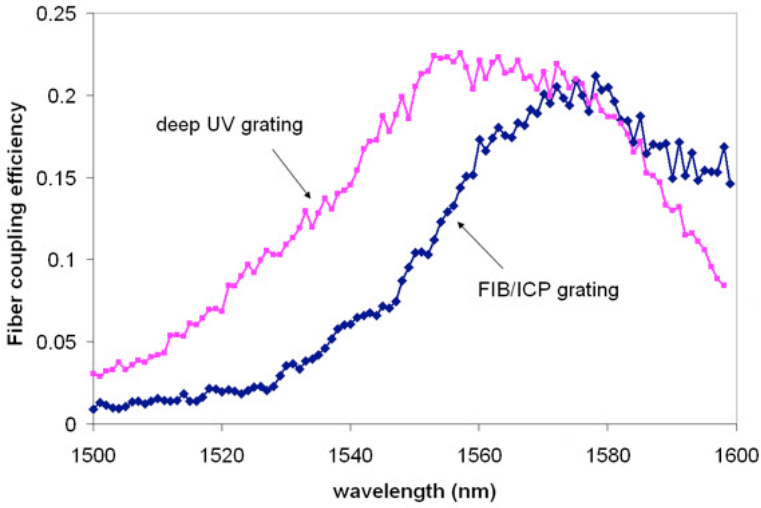

Figure 4.14: Measured coupling efficiency of a deep-UV and FIB lithography fabricated shallow grating coupler. The wavelength shift can be attributed to the narrow slits.

couplers, as depicted in Fig. 4.14. Although the center wavelength is slightly shifted (due to the trench width deviation) this measurement shows a comparable coupling efficiency.

Conclusion

Conventional shallow grating couplers were successfully fabricated with both iodine enhanced etching and FIB lithography. Both techniques produce grating couplers with comparable efficiency as the deep-UV fabricated equivalents, which demonstrates their potential for fabricating silicon photonic components with reasonably low losses.

4.2.2 Slanted grating coupler

Rationale

In previous paragraph it was shown that shallow grating couplers can be etched with FIB. However, these couplers have a moderate coupling efficiency of 25%, and do not exploit the full potential of FIB writing to etch small structures with three dimensional features. An approach to boost the efficiency is the use of slanted slits that are etched entirely through the waveguide layer, an approach that

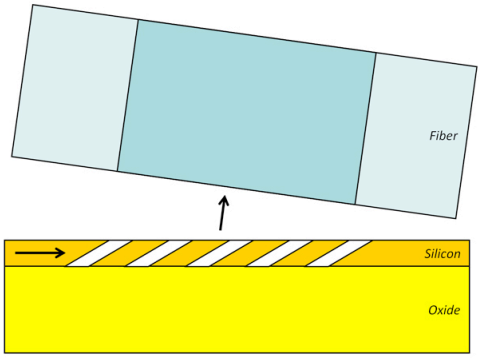

Figure 4.15: Schematic representation of the slanted fiber coupler.

was proposed in Ref. [79], and is depicted in Fig. 4.15. A similar approach was also used for the vertical coupling out of low vertical index contrast InP based integrated circuits [80]. In this paragraph we present the design and fabrication of a slanted grating coupler, combining the flexibility of FIB with the higher efficiency of slanted grating couplers. In the first part we discuss the design of a slanted fiber coupler, then we report on the fabrication with FIB, and in the final part we discuss the measurement results.

Simulation

Regular shallow gratings in SOI are limited in efficiency due to diffraction of the first order into the substrate. This limit can be circumvented by a bottom DBR mirror [64], or by a bottom gold mirror [81]. However, these greatly complicate the fabrication of integrated circuits in SOI. Another method to enhance the coupling to the upward first order is the use of slanted facets, in analogy to a blazed grating. Because it is difficult to control the depth of the slanted slits with FIB we have chosen to design a slanted grating with slits through the entire top silicon layer. We use SOI wafers with 220 nm top silicon and 2 μm buried oxide. The gratings were simulated with the finite difference time domain (FDTD) method in Omnisim[3] (Fig. 4.16). The optimization was done by first scanning the complete parameter space, followed by a local quasi Newton optimization. Although one can in principle couple light upwards by total internal reflection on a single slanted facet, there will be little overlap with

[3] see Appendix D

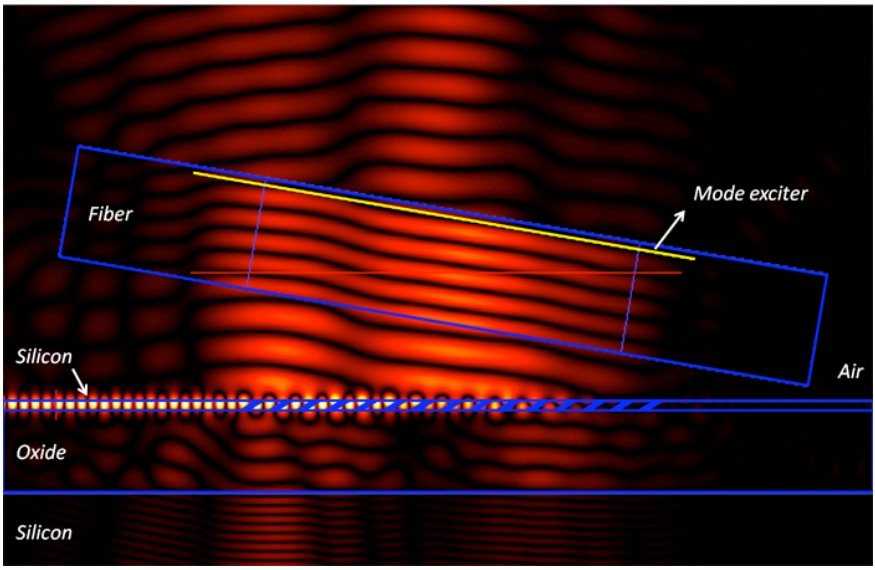

Figure 4.16: FDTD simulation of the optimal grating with 64% efficiency. The plot shows the field pattern at a wavelength of 1550 nm. The mode exciter is located in the fiber, the mode sensor in the SOI waveguide.

the mode in the fiber in that case. To ensure more overlap with the large fiber mode one needs to couple light upwards in a distributed way. This is feasible with - FIB fabricated - sub 100 nm slanted slits that allow tunneling of the evanescent field.

The optimum grating for 10° off-normal coupling has 87.5 nm wide slits at an angle of 58.4° to the surface normal and a grating period of 675 nm. The fiber is mounted at an off-normal angle of 10° to ensure a low second order reflection in the waveguide. Our simulations were performed on a 25 μm$\times$14 μm base, and converged with a 10 nm mesh. A plot of the calculated field pattern at a wavelength of 1550 nm is shown in Fig. 4.16. The slanted grating coupler has a fiber-to-chip coupling efficiency of 64% and a 3 dB bandwidth of 100 nm. Fig. 4.17 shows the calculated power fractions that are diffracted upwards; coupled into the fiber; and reflected in the waveguide. Since total internal reflection on the slanted air slit helps to redirect the light out of the waveguide plane we expected the reflected second order power to be relatively low, even for a perfectly second order grating. But this is not the case, as can be seen from the reflection peak around 1650 nm in Fig. 4.17. Therefore this grating was also designed for coupling to a nearly-vertical fiber position (10°

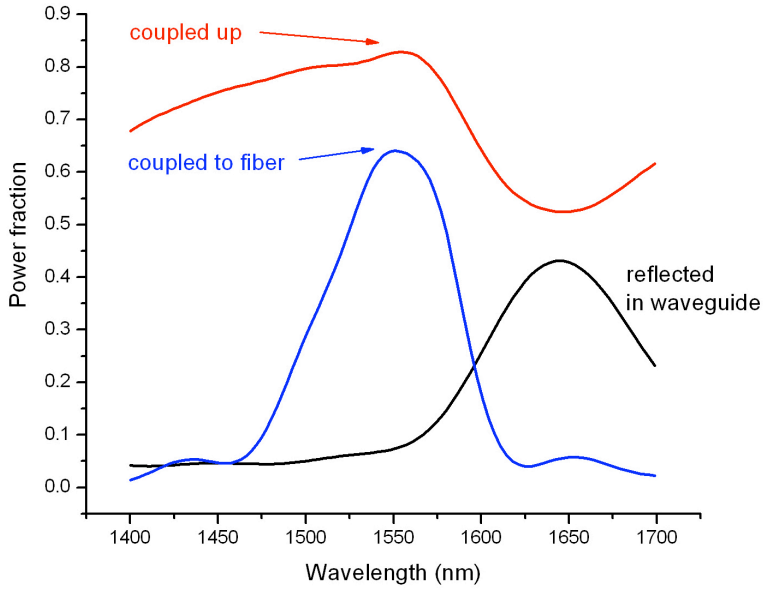

Figure 4.17: Result of the slanted coupler optimization with a FDTD simulation. The curves present the power fractions coupled upwards, coupled into the fiber mounted at 10°, and reflected back into the waveguide.

off-normal). The maximum amount of power diffracted out of plane is 83% at 1550 nm. Only part of this upward power is coupled into the fiber due to mode mismatch for a periodic grating. This can be circumvented by designing gratings with varying slit widths. However, due to fabrication complexity of varying slit widths, we have chosen only to design and fabricate uniform slanted grating structures.

Fabrication with iodine enhanced FIB etching

The angled slits were fabricated with iodine enhanced FIB etching in one step. To ensure that the slits would be thin and have parallel sidewalls a 50 nm alumina layer was first deposited with electron beam evaporation. The sample was then mounted at an angle of 58.4° with respect to the impinging ion beam, with the help of an angled sample holder. Both hard mask and silicon are then etched in the same run. The milling algorithm consists of parallel lines with a pith of 675 nm$\times$ cos(58.4°) = 353.7 nm. These lines are scanned digitally with a dwell time of 400 ns and a pitch of 30 nm. Narrow slits

are formed due to the large etch rate difference between alumina and silicon. The etch dose was optimized to etch down to the oxide buffer layer. We have noticed that the slit width depends strongly on the beam size. The applied beam current was 50 pA, which corresponds to a minimum beam size of 30 nm. However, when the beam is not carefully focused and corrected for stigma errors the beam size and shape alter, and the width and depth of the resulting slits are not reproducible. It appears that etching of slanted slits is more sensitive to these beam size errors than perpendicularly etched structures, which is a complication that can not be neglected. This explains why no continuous optimization in function of etch dose was obtained (as in Fig. 4.12 for the shallow couplers). However, the use of an automated focus and stigma correction approach can improve reproducibility and alleviate this problem.

A cross-section of two grating slits and a top view of a slanted grating coupler are shown in Fig. 4.18. Alignment of the etched lines on the waveguide was done by making an ion microscopy image. As opposed to the shallow grating couplers from the previous paragraph only one slanted grating coupler was etched per prefabricated waveguide. For an etch dose of 1.1×10^{13} Ga^{+}/cm [4] the slits are etched down to the oxide buffer layer and the slit width of about 90 nm roughly corresponds to the simulations. The etch time for 15 slits that are 10 μm long is about 8 minutes. After fabrication the sample was baked for two hours on a hotplate at 300°C in a nitrogen atmosphere. The hard mask layer was not removed.

Measurement and discussion

To determine the coupling efficiency of the fabricated coupling structure we have used a fiber-to-fiber transmission measurement for TE polarized light from a super luminescent LED. The structure consisted of a regular shallow input coupler fabricated with optical lithography, a broad 10μm waveguide, and a slanted output coupler fabricated in situ with FIB. The spectrum from the source as well as the coupling spectrum of the shallow couplers were measured in a separate setup. The coupling efficiency of the slanted grating coupler is depicted in Fig. 4.19. It is calculated by subtracting - on a logarithmic scale - source spectrum and shallow coupler spectrum from the measured spectrum. We have extracted a maximum fiber-to-waveguide coupling efficiency of 46% and a 3 dB bandwidth of

[4] As the etched structure here is a line, the etch dose is mentioned in particles per unit length instead of unit area.

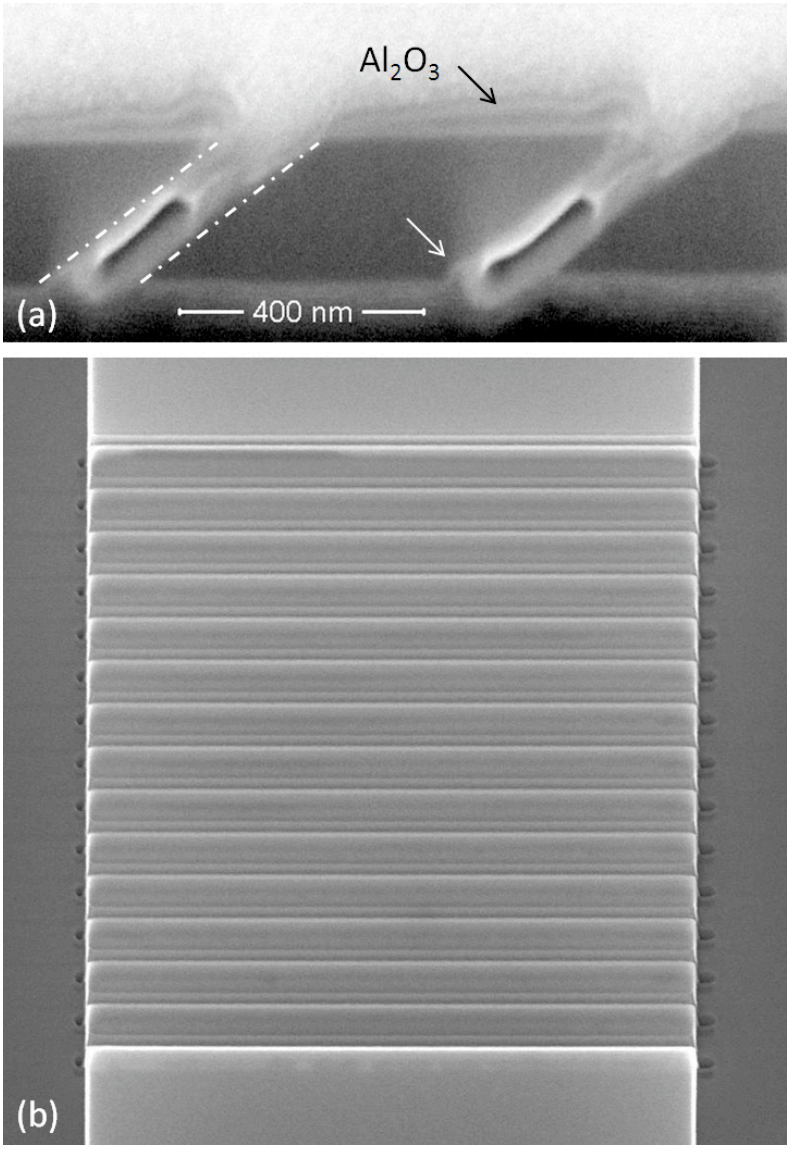

Figure 4.18: (a) Cross-section of two slits of a slanted grating coupler. The dash-dotted lines highlight the edges of the 90 nm wide slits that are etched under an angle of 58-59° with respect to the surface normal. The white arrow highlights a small bulge near the bottom of the slits (see text). (b) A top view of a slanted grating coupler on a 10 μm wide waveguide.

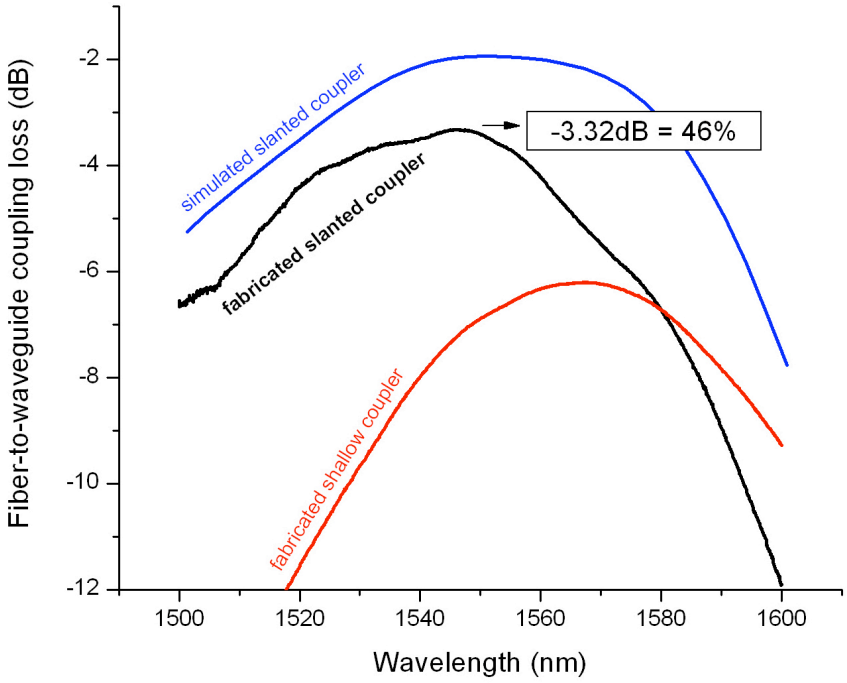

Figure 4.19: Coupling spectra of simulated and fabricated slanted fiber coupler, as compared to a shallow grating coupler fabricated with optical lithography.

about 80 nm for the slanted fiber coupler fabricated with FIB. A single slanted coupler was etched per waveguide due to the reproducibility problems as mentioned.

To evaluate the discrepancy between simulated (64%) and measured (46%) coupling efficiency we have investigated the fabrication tolerances of the slanted coupler through simulations. When period, slant angle, and slot width were varied within the fabrication errors the observed drop in efficiency was below 5%. Therefore bad grating parameters can not fully explain the discrepancy between simulated and measured coupling efficiency. However, as mentioned in Chapter 3, a damaged silicon layer is left behind after iodine enhanced FIB etching followed by baking. After iodine enhanced etching of waveguides from the top (followed by baking), a 40 nm thick damaged layer with a material loss of about 1650 cm^{-1} is left behind. When slits are etched, the incidence angle of the ions bombarding the slit sidewalls is close to grazing instead of normal and the implantation depth decreases. According to a SRIM calculation with

30 keV impinging gallium atoms at a grazing incidence of 89°, the projected range peaks at 8 nm. Therefore an approximate damaged layer thickness of about 10 nm can be assumed. We have performed a simulation to verify the effect of such a thin damaged layer on the edge of each slit of the coupler. For a 10 nm thick damaged layer (1650 cm^{-1}) the theoretical coupling efficiency is still more than 60%; therefore this effect can not fully account for the observed discrepancy. However, upon close inspection of cross-sectional micrographs of the fabricated slanted grating it can be observed that the bottom of each slit shows a small bulge (white arrow in Fig. 4.18(a)). This is likely to be caused by ions that are backscattered off the bottom oxide and etch the silicon in an upward direction. This location is well hidden from the gas needle that supplies the iodine molecules, which causes iodine depletion and ineffective etch enhancement. Furthermore the gallium ions impinge perpendicularly; thus a damaged silicon layer of considerable thickness forms. Optical absorption in this damaged region near the slit bottoms can explain the discrepancy between the measured efficiency of 46% and the theoretically expected value of 64%.

Conclusion

A uniform slanted grating coupler was designed with a theoretical coupling efficiency to a near-vertical single mode fiber of 64%. The grating was fabricated with iodine enhanced FIB etching and shows a coupling efficiency of 46%. It features 90 nm slits at an angle of 60° relative to the surface normal and therefore demonstrates the potential of FIB to fabricate silicon photonic devices with superior flexibility over other fabrication technologies.

4.2.3 Silicon overlay coupler

Rationale

Another approach to increase the efficiency of a grating coupler is the use of a silicon overlay, as presented in Fig. 4.20 taken from [82]. Thanks to the thicker silicon membrane and deeper trenches there is constructive interference between upwards traveling waves originating from the top and bottom of each grating tooth. This makes that diffraction to the upward first order is more efficient than the first order going down into the substrate. As a result, efficiencies higher than 60% can be obtained for uniform gratings, and even

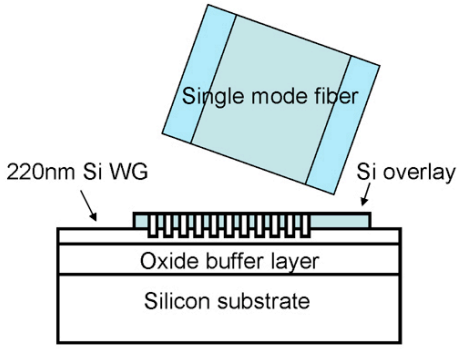

Figure 4.20: Schematic representation of a silicon overlay coupler, from [82].

higher ones if the width and placement of the trenches is varied across the grating. In this paragraph we discuss the fabrication of a uniform overlay grating with iodine enhanced etching in two steps and with FIB lithography and ICP etching.

Fabrication with iodine enhanced FIB etching

Although this coupler can in principle entirely be fabricated with CMOS compatible techniques such as silicon overgrowth and chemical mechanical polishing, a first prototype was fabricated with FIB.[5] For this prototype a 150 nm thick amorphous silicon layer was deposited with electron beam evaporation, followed by a lift-off technique for defining the overlay rectangle. Afterwards a 50 nm alumina layer was deposited also with electron beam evaporation, and 220 nm deep trenches were etched in the silicon stack with the same two-step etch process as applied for the shallow grating couplers (but with higher dose in the second step). We aimed for a grating period of 610 nm and trench width of 305 nm. A micrograph of the fabricated device and the measured spectrum are shown in Fig. 4.21, as well as the experimentally determined coupling efficiency of a deep-UV fabricated shallow grating coupler (period 630 nm; trench width 315 nm and depth 70 nm). The expected theoretical coupling efficiency for this coupler was 66% (-1.7 dB). Although the experimentally achieved efficiency of 32% (-5 dB) is about a 2 dB improvement over the regular shallow grating design, it is lower than the expected value. This is likely to be caused by absorption in

[5] In collaboration with G. Roelkens, who originally proposed this structure.

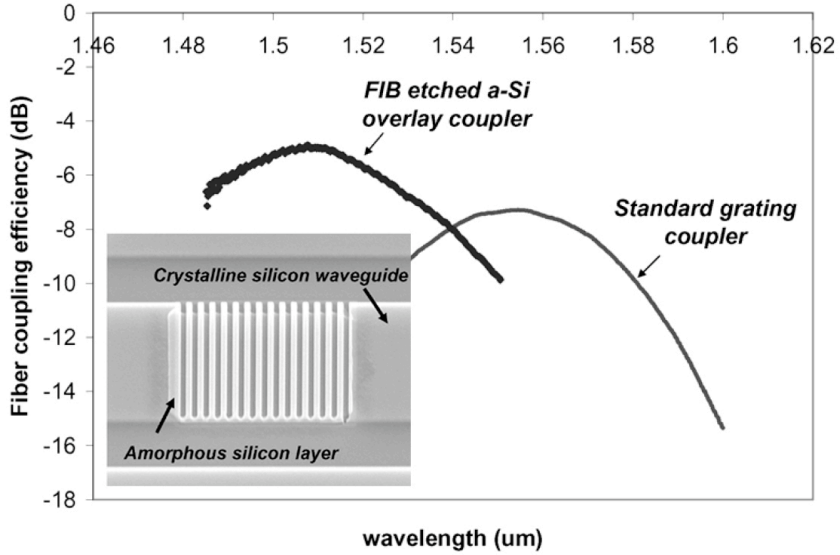

Figure 4.21: Measured efficiency of the first fabricated overlay grating prototype, which shows a 2 dB coupling loss improvement over the standard shallow coupler. The inset shows a micrograph of the fabricated device.

the deposited amorphous silicon and by residual material damage caused by FIB etching.

Although FIB prototyping was successfully used to demonstrate a proof of concept of higher efficiencies by adding a silicon overlay, the intended fabrication technology was deep-UV lithography. This was therefore the pursued approach for later prototypes, and has recently led to an experimentally demonstrated coupling efficiency of 55% [83].

4.2.4 Metal grating coupler

A completely different approach to couple light out of a silicon waveguide is by using a metal grating, as proposed in Ref. [84]. It is generally known that metals absorb light, and that therefore they are not a good material to use in combination with passive photonic components. However, the imaginary part of the refractive index of various metals (Au, Ag, Al) is so large that only a small amount is needed to create the necessary refractive index contrast that makes up a diffractive grating, thus not absorbing much of the

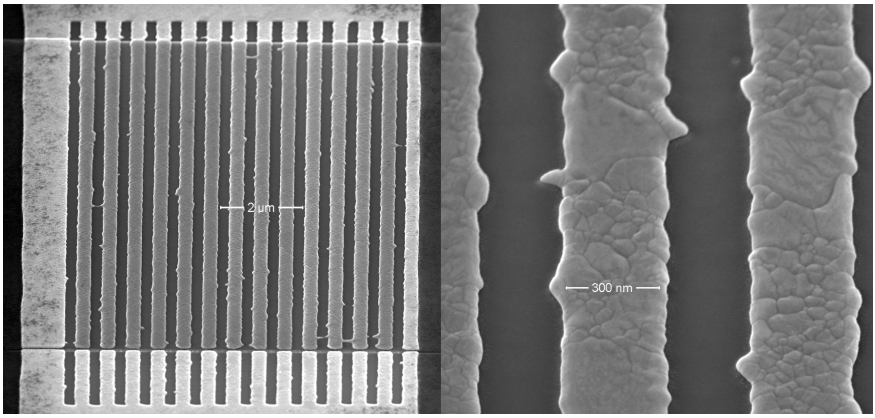

Figure 4.22: Micrographs of a FIB fabricated gold grating coupler prototype. A 50 nm alumina layer under the gold acts as etch stop layer and protects the underlying silicon from ion damage. The roughness is caused by the sputter yield dependency on crystal orientation and could not be avoided. Nevertheless, it has only a limited effect on the coupling efficiency.

optical power. A typical metal grating coupler therefore consists of thin (typically 40 nm) metal stripes on a silicon waveguide, and a theoretical coupling efficiency of 60% has been demonstrated by optimizing the parameters [85]. This type of grating couplers is of interest because the waveguides do not need to be etched. Therefore these gratings can be used in a probing setup where the grating is attached to a fiber and pressed onto the waveguide [86] for non-destructive in situ probing of the optical power inside a waveguide. Furthermore the focussing capacity of curved grating lines has been demonstrated [78].

To validate this coupler concept a first prototype device was fabricated with FIB (see Fig. 4.22). The designed gratings with highest efficiency consist of metal stripes in direct contact with the silicon. However, when these stripes are defined with FIB by etching a metal layer, the underlying silicon is damaged, which reduces grating efficiency. Therefore the design had to be altered to incorporate a protective layer under the metal (gold in this case). We have chosen to deposit a 50 nm alumina layer on the silicon prior to gold deposition. However, this intermediate layer reduces the maximum coupling efficiency to about 14% for the fabricated design.

Fig. 4.22 shows the FIB fabricated coupler. After deposition of the alumina layer a 40 nm thick and 10 μm wide gold stripe was deposited by thermal evaporation and lift-off. Then the gold grating

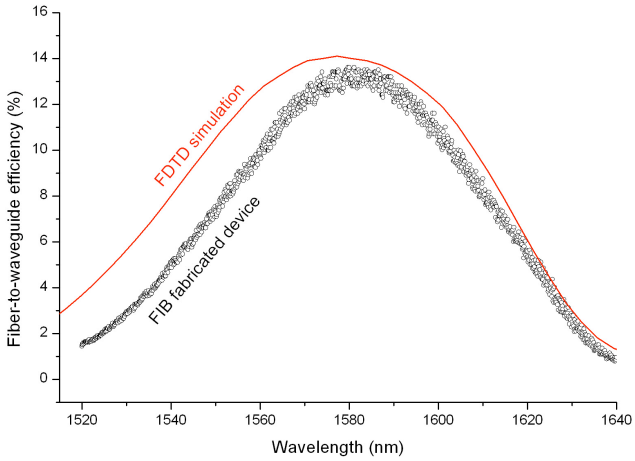

Figure 4.23: There is an excellent agreement between experimental and simulated coupling efficiencies of the FIB fabricated prototype of a gold grating coupler.

was etched by direct FIB milling (50 pA) without gas enhancement, where the alumina layer acted as etch stop layer and protected the underlying silicon. Since metals are naturally lossy for near infrared light, ion damage and implantation cause little effect. This is also why FIB is an interesting prototyping technology for plasmonic devices [10, 11, 22]. The simulated and measured coupling efficiencies for a gold coupler with 620 nm period and a filling factor of 40% are depicted in Fig. 4.23. The experimental results are in excellent agreement with simulations.[6]

4.3 Slot structures

Rationale

Slot waveguide structures have recently attracted much attention because of their ability to tightly confine light in a material with low refractive index [87, 88]. As opposed to resonant confinement schemes, introducing a slot in a high index waveguide, such as a silicon waveguide, enables broadband confinement in a low index material. Slot structures amplify the interaction between tightly confined optical modes and low index contrast materials, which is of

[6]The simulations and measurements were performed by S. Scheerlinck in the framework of his PhD, see Ref. [84].

great interest for various devices such as sensors, modulators, etc. The SOI platform is attractive for the fabrication of these devices. However, the typical size of a slot in a silicon waveguide is of the order of 100 nm, which is a challenge for current optical lithography techniques such as 193 nm and 248 nm optical lithography [89]. Therefore, most of the demonstrated prototype slot structures were fabricated by electron beam lithography and dry etching [88, 90].

An alternative prototyping approach is FIB etching of existing waveguides, which is difficult with resist based methods such as electron beam lithography. This approach is interesting because it narrows the area fabricated with a serial - and therefore slow - technique to only the slot. More specifically in combination with deep-UV pre-fabricated waveguide structures this prototyping approach is faster and more cost effective than electron beam lithography, where writing of access waveguides and coupling structures takes up most of the patterning time. Furthermore FIB offers superior flexibility since slanted structures and more complex geometries can be incorporated as well.

In this paragraph we will demonstrate the potential of FIB prototyping by fabricating slots in existing wire waveguides and racetrack resonators. We first discuss the optimization of the slot width by simulation, then we present the FIB fabrication of slots both by FIB pattering with iodine etch enhancement and by FIB lithography, and finally we demonstrate a measured propagation loss of 100 dB/cm for a straight slot waveguide and a Q value of 850 for a slot ring resonator with slot widths of respectively 90 and 120 nm.

Simulation

An SOI substrate with 220 nm silicon membrane on top of a 2 μm oxide buffer layer was used; and simulations were performed in CAMFR[7]. All simulations were performed with water as top cladding, targeting sensing applications.[8] First we have determined the substrate leakage losses as a function of slot width and total waveguide width. The results are presented in Figure 4.24 (left vertical axis). For 500 nm waveguides the losses increase dramatically for slot widths in excess of 100 nm because the mode size increases; in 600 nm waveguides the losses are more than one order of magnitude lower. Nevertheless, these substrate leakage losses are far lower than the mea-

[7]We refer to Appendix D for more details.

[8]These simulations were performed by J. Van Lysebettens in the framework of a MSc. thesis.

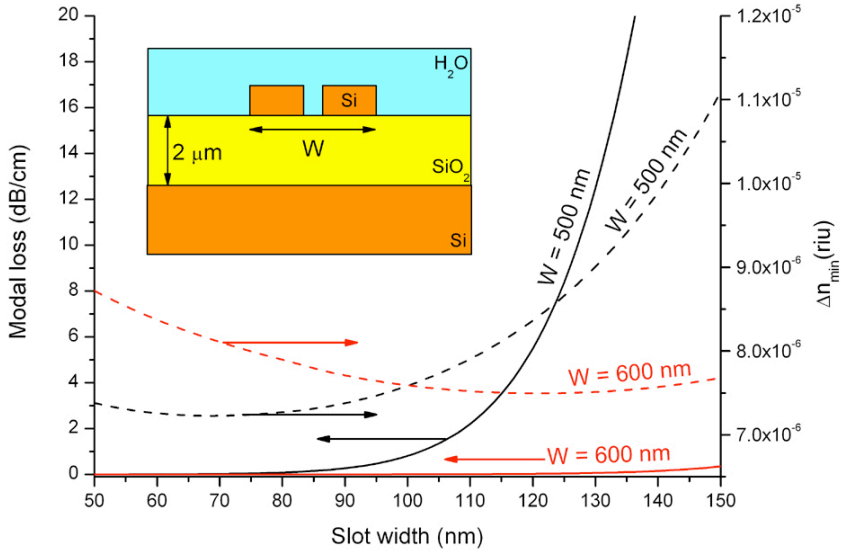

Figure 4.24: (Left axis) Simulated modal loss due to substrate leakage through the 2 μm bottom oxide cladding, in function of slot width for 500 and 600 nm wide wires. (Right axis) Minimally detectable change in refractive index of the top water cladding.

sured material absorption losses (see later). Another important optimization parameter is the mode overlap with the top cladding material, i.e. the aqueous region shown in the inset of Fig. 4.24, which determines the sensitivity of resonance wavelength shifts on changes of refractive index in this material. The results of this simulation are presented on the right vertical axis in Figure 4.24, supposing that the minimally detectable resonance wavelength shift is 5 pm, at a wavelength of 1550 nm. For 600 nm wires the optimum slot width is around 120 nm, for 500 nm it is about 70 nm.

Fabrication with iodine enhanced FIB etching

The slots were fabricated with a beam current of 50 pA and acceleration voltage of 30 keV, corresponding to a beam size of about 30 nm. We have used the single step etch process using iodine explained earlier in this chapter, and therefore deposited a 50 nm alumina layer on the deep-UV fabricated waveguides. After FIB etching the sample was baked on a hotplate in N_2 for 2 hours at 300°C to remove the non-volatile silicon-iodide layer. Alignment of the etched slot on the

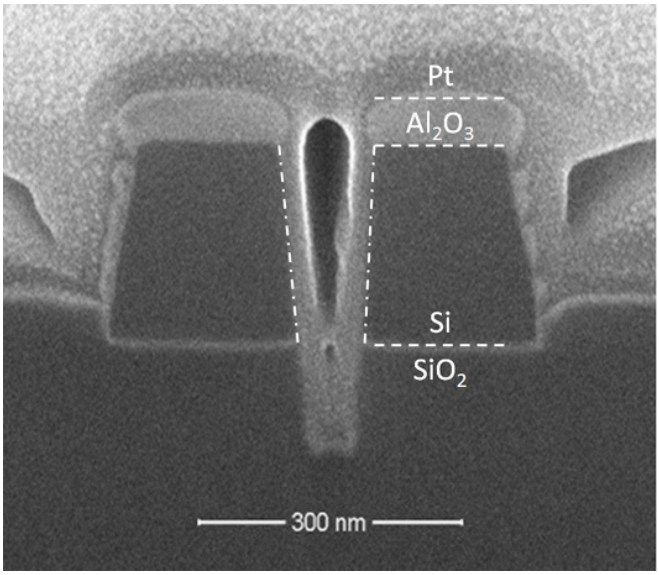

Figure 4.25: Cross-sectional micrograph (after Pt deposition) of a FIB etched 90 nm wide slot in a 500nm wide waveguide. The dash dotted lines highlight the slot edges.

existing waveguides and rings was performed by making ion microscopy images and visually overlaying the slots. The precision of this technique was limited by the 12 bit digital scan generator in the FEI software.[9] A higher magnification increases the alignment accuracy; but to be able to etch a slot in a racetrack resonator (with bend radius of 6 μm and straight sections of 3 μm) without stitching, a field of view of 25.6 μm was chosen. The patterns were defined with a digital scan algorithm, with a dwell time of 400 ns and a pitch of 30 nm, using the *stream file* format of FEI. To etch straight slots with a length of 30, 40 and 50 μm a single stitch was used. Fig. 4.25 shows a cross-sectional micrograph of a 90 nm slot in a 500 nm wide waveguide (Pt was deposited in situ before cross-sectioning). This slot was etched in the presence of adsorbed iodine on the surface, in 170000 passes, where each point is etched for 400 ns per pass. This corresponds to an etch dose of 6.9×10^{12} Ga^+/cm. 90 nm was the thinnest slot we could etch with a beam current of 50 pA and beam size of 30 nm.

The same process was used to etch a slot in a 600 nm wide racetrack resonator. However, in this case the number of passes was

[9]The Raith system has a 16 bit scan generator but could not be used for gas enhanced etching due to the short dwell time (400 ns) that is required.

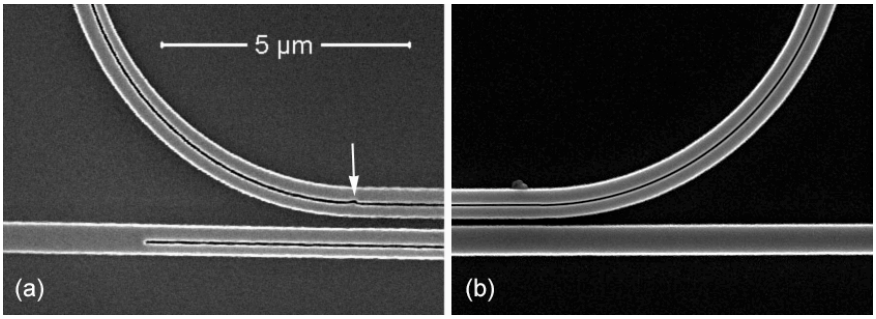

Figure 4.26: Top view micrograph of part of a FIB etched slot in an access waveguide and racetrack resonator etched by way of (a) FEI stream file and (b) Raith pattern. The latter allows more complex alignment strategies (three point alignment here) and more correct pattern reproduction, cfr. white arrow in (a). However, our Raith system does not support iodine enhanced etching.

275000, which brings the total etch dose to 1.14×10^{13} Ga^{+}/cm (total etch time was about 2 min). The measured slot width was 120 nm. Fig. 4.26(a) shows a top view micrograph of part of the etched slot in access waveguide and racetrack resonator. The alignment errors are mainly caused by the simple visual alignment procedure, and can be alleviated by using more complex alignment strategies implementing image recognition and multi-point alignment of the write field. An example of a slot etched with Raith patterning software after three-point alignment on nearby structures is shown in Fig. 4.26(b). This alignment involves stretching and rotation of the write field and yields a more reproducible result than visual alignments. Furthermore the Raith pattern is etched with more elaborate beam stabilization and with additional shuttering between beam movements. Therefore pattern errors, as shown by the white arrow in Fig. 4.26(a) are avoided. However, our Raith system does not support the short dwell times that gas enhanced etching requires.

Fabrication with FIB lithography

Although the Raith system does not support gas enhanced etching, it can be used for FIB lithography. It was shown earlier that 100 nm slits were etched in a silicon slab (Fig. 4.6). However, the ICP process used for this is not sufficiently directional and etches the sidewalls of the waveguides since only little alumina is deposited here. Fur-

thermore slot width and depth were not sufficiently reproducible. Therefore this approach was abandoned.

Measurement and discussion

The devices were characterized in a fiber-to-fiber transmission measurement. The setup consists of polarization controlled light from a tunable laser that is coupled in and out of broad waveguides by near-vertically positioned fibers and grating couplers. The broad waveguides were adiabatically tapered to 500 and 600 nm wide waveguides. A droplet of water was placed on top of the fabricated devices to provide the aqueous top cladding.

The propagation losses of the straight slot waveguides were calculated by linear regression of the loss through device lengths from 10 μm to 50 μm, as displayed in Fig. 4.27 (Top). The plotted data points are the average values of two consecutive measurements of four identical samples. A distinction between slots up to 20 μm and longer ones can be made: shorter slots were written in one field of view, longer ones were stitched once. The result is a propagation loss of 100 dB/cm, a coupling loss between waveguide and slot waveguide of 1.8 dB, and a stitch loss of 0.1 dB. The coupling losses are about twice as large as what we expect from calculating the mode overlap for perfect alignment. This is likely to be caused by misalignments of the slot, although simulations of this effect were inconclusive.

The propagation losses of 100 dB/cm are close to the value of 200 dB/cm that we have measured for waveguides etched from the top (Chapter 3), which we have attributed to a damaged material layer with a thickness of 40 nm and an absorption coefficient of 1650 cm^{-1}. In the case of a slot or any other vertical structure (similar to the slanted grating slits), the expected residual damaged layer is thinner because of the lesser penetration depth of the impinging ions. Supposing the same loss coefficient of 1650 cm^{-1} we have performed a simulation to determine the modal loss of a slot waveguide as a function of the thickness of this damaged slot sidewall.[10] The slot waveguide dimensions and the top water cladding were taken as in the experiment. For a damaged layer thickness of 10 nm an absorption of the ground mode of 100 dB/cm was obtained, which is in good agreement with the projected ion range of 8 nm that was

[10]This simulation was performed in FIMMWAVE, for more details we refer to Appendix D.

determined with SRIM for 30 keV Ga impact at 89° relative to the surface normal.

These loss values are not as low as previously reported for electron beam fabricated slot waveguides (about 10 dB/cm [90]). However, since FIB is a serial technique, the length of etched devices for prototyping purposes is not likely to exceed 100 μm. This yields a 1 dB loss per device, which is acceptable. Furthermore, FIB can be used to etch slots in existing waveguides, which is difficult with resist-based methods such as electron beam lithography.

The normalized transmission spectrum of the fabricated slot racetrack resonator is displayed in Fig. 4.27 (Bottom). The dips in the spectrum clearly indicate resonances in the racetrack with bend radius of 6 μm. A Q value of about 850 and an extinction ratio of 25 dB were measured around 1560 nm; suggesting that the device is operating near critical coupling. From simulations it can be expected that round trip losses for this ring are dominated by propagation losses, with smaller contributions from bend losses and mode mismatch between straight and bent sections. However, calculation of the round trip losses from the various resonance dips in this measurement has lead to inconclusive results. Although the Q value is likely to increase after high temperature annealing, the current process is attractive as rapid prototyping technique, for instance for the design verification of high-sensitivity bio-sensors. Furthermore, the iodine terminated silicon surface present in the slot can be of interest for localized functionalization [91].

Conclusion

Slots were etched in pre-fabricated waveguides and racetrack resonators, resulting in a slot waveguide propagation loss of 100 dB/cm and a resonator Q value of 850. Similar as in Chapter 3 the propagation loss can be attributed to a residual absorbing silicon layer with estimated thickness of 10 nm and loss of 1650 cm^{-1}.

4.4 Conclusions

This chapter summarizes the strategies used for the fabrication of silicon photonic devices. As pointed out in Chapter 3, iodine etch enhancement can lead to a reduction of the FIB induced losses, but as pointed out in this Chapter it also reduces the dimensional control of etched features and therefore requires the use of a hard etch

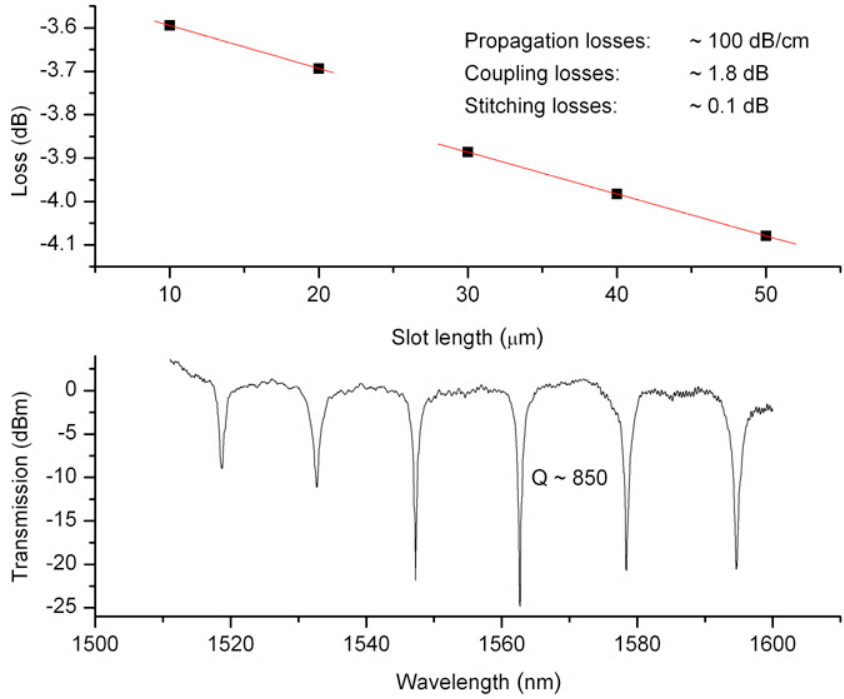

Figure 4.27: Top: transmission measurements of 90 nm wide slots etched in a 500 nm wide silicon waveguide yield a propagation loss of 100 dB/cm. Bottom: transmission spectrum of a 600 nm wide racetrack resonator with 120 nm wide slot. We have measured a Q value of about 850 and an extinction ratio of 25 dB.

mask. Alumina was identified as the most suitable material. A one- and two-step etch procedure was proposed for the fabrication of respectively deep slits and shallow trenches. Both were successfully demonstrated for the fabrication of several prototype devices such as a slanted grating coupler, a slot resonator, and a silicon overlay grating coupler. From vertically etched slots we have extracted the parameters of the residual damaged silicon layer, similar to what was obtained for horizontally etched structures in Chapter 3. Another fabrication strategy - utilizing FIB in combination with plasma etching - was proposed and was successfully used to etch conventional grating couplers, but reproducibility problems have led us to abandon this approach for the fabrication of other prototype devices.

The work presented in this Chapter has led to three publications in scientific literature (Appendix A.2 #1, #8, #10).

Chapter 5

Trimming of silicon photonic devices

5.1 Introduction

Silicon on insulator is the ideal platform for compact and low-cost optical filters for telecommunications or sensor applications. Several geometries, such as ring resonators [92] or photonic band gap materials [93] have good filtering characteristics. However, most of the demonstrated filters were fabricated with electron beam lithography, a serial and therefore slow fabrication technique. In previous work in our group it was demonstrated that these filters can also be fabricated in a parallel way, with 248 nm or 193 nm deep-UV lithography on a CMOS pilot line [62, 94]. This is the only technology that is sufficiently mature and cost effective to allow high volume production at low cost.

However, for the fabrication of CMOS devices, a variation of the critical dimensions of about 10% can be allowed. These variations can be caused by wafer non-uniformity, by for instance varying layer thicknesses on wafer edges, or by non-uniformity within one chip, mainly caused by lithography imperfections near mask edges. These variations of the critical dimensions of devices fabricated by optical lithography are inevitable, even for the most advanced deep-UV lithography with 248 nm and 193 nm excimer lasers. However, for nanophotonic structures a variation of for example the width of a ring resonator by 1 nm (only 0.2% of the waveguide width) causes a resonance wavelength shift of typically 1 nm [94].

A way to assess critical dimension variations in a photonic circuit is to evaluate the resonance wavelength shift of identically designed ring resonators, dispersed over a wafer. These resonators can be fabricated with Q-factors of about 10^4 [92], or a 3 dB bandwidth of 0.15 nm. In practice the resonance wavelength shifts exceed 1 nm [94], which is unacceptable for many applications. This problem can be circumvented by altering the circuit after fabrication. Two different techniques are used for this purpose: trimming and tuning techniques. Tuning denotes a time-dependant and reversible change of the optical circuit; trimming means a non-reversible static change.

The most straightforward tuning technique in silicon is active thermal tuning either by heating the entire sample or by lithographic definition of electrical heaters close to the area of interest [95, 96]. However, if one envisages many resonators on a single chip, thermal tuning (in this case with electrical heaters) would lead to high power consumption and important device complexity. Another tuning solution is carrier injection or depletion [3]. This technique can be used for high-speed modulators but requires local doping of the silicon. From these examples it is clear that tuning techniques are not suited for the purpose of small modifications after the fabrication.

In this chapter we discuss two trimming techniques suited for small non-reversible modifications of the refractive index of nanophotonic structures. We locally and independently trim the resonance wavelength of ring resonators on a silicon chip, either by FIB etching or by electron beam induced compaction. Although these are serial techniques - considering that trimming can greatly improve the performance and reduce the power consumption of devices and that is has to be performed only once - we believe that these techniques can be suitable for high volume production.

5.2 FIB versus electron beam trimming

The resonance wavelength of a ring resonator is trimmed by changing the optical path length of the resonator, in our case by varying the effective index of the guided mode and not the length of the ring. The resonance wavelength fits an integer amount of times in the cavity with length L:

$$Ln_{eff}/\lambda_{res} = m. \tag{5.1}$$

Therefore a change in the effective index causes a shift of the resonance wavelength according to the formula

$$\frac{\Delta n_{eff}}{n_{eff}} = \frac{\Delta \lambda_{res}}{\lambda_{res}}, \tag{5.2}$$

an increase in the effective index thus leads to a resonance shift to longer wavelengths, which we will refer to as red-shift for convenience. Similarly other kinds of cavities, such as 1D or 2D photonic crystal cavities, can be tuned by altering the effective index of the supported mode. This was recently demonstrated on active 2D photonic crystal cavities by the electron beam induced growth of carbon nanocrystals [97].

Trimming by FIB etching can in principle be done by removing material, for example by reducing the width or height of a waveguide. However, considering the high optical losses discussed in Chapter 3, a device would need a thermal treatment after trimming. This is not opportune when *live* trimming is envisaged (by measuring the transmission during trimming). Therefore we will first deposit an alumina layer on top of the devices prior to trimming, as discussed later.

Trimming by UV or electron beam irradiation was demonstrated in several (low to medium index contrast) material systems such as silica glass [98] and SiN/SiON [99, 100]. These waveguide materials are sensitive to either UV or electron beam compaction. Compaction means that the volume of the material shrinks in the irradiated area, causing an increase in density and in refractive index. Due the constraining effect by the surrounding material the resulting material is under tensile strain and the surface is depressed, as depicted in Fig. 5.1. Literature reports on SiO_2 volume compaction and refractive index changes upon irradiation with highly energetic particles. The particles include ions and gamma photons, by which the oxide compacts due to knock-on atom displacements, or electrons and UV photons, where the compaction is caused by ionization-induced relaxation of inherently strained Si-O bonds in the glass network [101, 102, 103].

In low index material systems the compacted material contains most of the optical mode (waveguide core material) and thus relatively large shifts in effective indices can be obtained. E.g. in SiN, more than 10 nm of resonance wavelength shift was obtained for ring resonators operating at 1550 nm [99]. Electron beam [105, 106, 104] as well as UV [107, 108, 109] irradiation have also been used to fabricate or alter waveguides in silica glass and trim arrayed waveguide gratings [108]. However, in SOI the core material is silicon, which can not be compacted by either UV or electrons; only the SiO_2

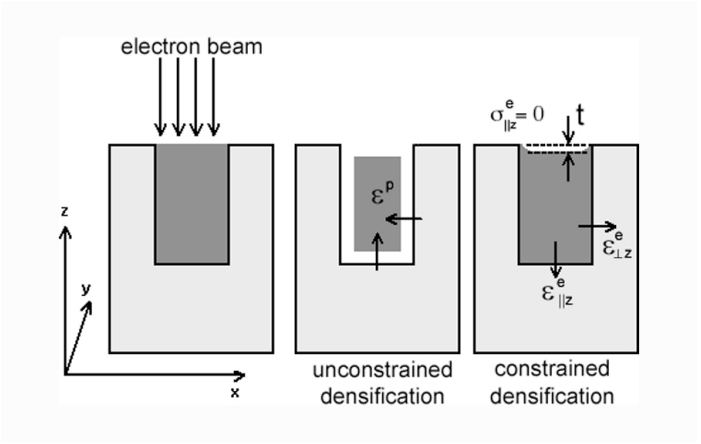

Figure 5.1: Compaction by electron beam irradiation leads to surface depression. Reprinted from Ref. [104].

cladding is susceptible to compaction. Due to the limited modal confinement in the cladding the trimming effect is therefore limited. As will be presented in this chapter this limitation of the trimming range can be circumvented by using compaction induced stress as a complementary effect.

In the following paragraphs we will discuss trimming experiments both by FIB etching and by electron beam compaction and compare the results.

5.3 General experimental setup

Reference ring

The resonance frequency of silicon ring resonators is extremely sensitive to changes of temperature and of the surrounding medium; rings are therefore attractive as sensors [110, 111]. However, in this experiment we want to exclude all external factors and investigate the resonance shifts caused only by the trimming mechanism. Therefore we have fabricated a sample with two rings, with different resonance wavelengths, serially connected to the same waveguide, as depicted in Fig. 5.2. Only one of these rings is trimmed; the transmission spectrum features two superimposed ring spectra of which one moves due to trimming and both can move due to external factors. By evaluating only relative peak shifts between the two ring spectra the external influences such as temperature variations are

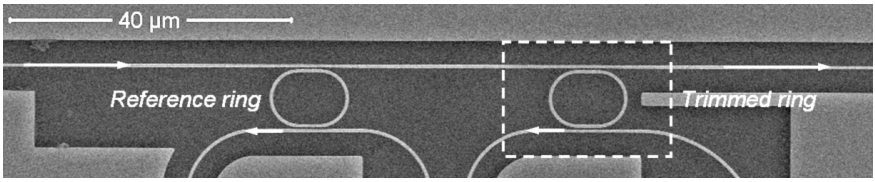

Figure 5.2: Overview of the experiment: the right ring is trimmed by FIB etching or electron beam compaction; the left one is left unchanged as a reference to exclude temperature or ambient variations.

excluded. This assumes that the trimmed ring and the original ring have an identical response to changes in temperature and humidity, which is a good approximation. But it also supposes that all external factors act on both rings at the same time, which is not the case for e.g. dust particles attaching to one of the rings. This will be discusses later.

In situ versus ex situ

Both in situ (i.e. *live* trimming) and ex situ experiments were performed. The in situ trimming experiments were performed inside the vacuum chamber of the FEI system (only for electron beam trimming), by providing it with vacuum fiber feedthroughs. The optical input and output signals are transported by single mode fibers, glued (with UV-curable glue) in a near-vertical position above grating couplers (see Fig. 5.3). The optical circuit, with grating couplers, waveguides, tapering sections, and ring resonators, was fabricated by deep-UV lithography on a CMOS pilot line [62]. Light was generated by a super luminescent LED with center wavelength at 1530 nm and detected by a spectrum analyzer with a resolution of 60 pm. A spectrum was measured every 10 s.

Ex situ experiments were performed (both FIB and electron beam trimming) by subsequently doing the optical measurements and the irradiation. The measurement of the spectrum in this case was performed on a setup with near-vertically positioned fibers, located inside the same clean room as the FEI system. Light was generated from a tunable laser (5 mW), polarization controlled, and detected by a photodiode. First the transmission spectrum of a specific ring was measured; then it was trimmed after loading the sample into the vacuum chamber; then the sample was unloaded and again measured; and so forth. For each data point the sample was loaded in

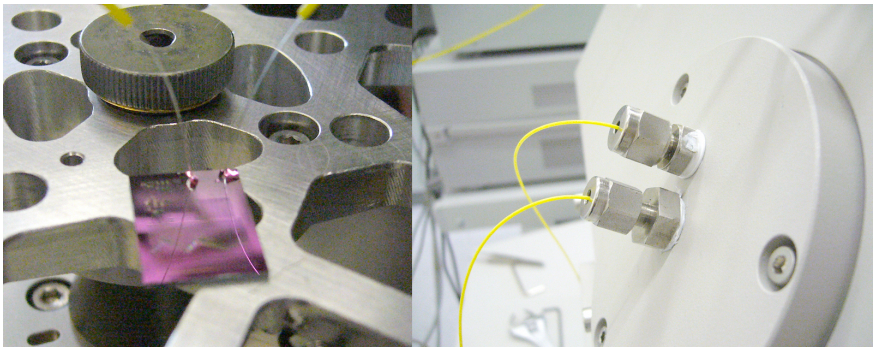

Figure 5.3: Sample mounting with glued fibers and vacuum fiber feedthroughs.

and out of the vacuum chamber, but the sample always remained in a clean room environment.

5.4 FIB Trimming

As we have discussed in Chapter 3, bombardment of silicon with gallium leads to optical losses, even when gas enhancement is used. Although these losses can be reduced by annealing, this approach is not desirable because it excludes the possibility for *live* trimming (i.e. by measuring the resonance while trimming). We have therefore chosen an approach where the resonator is first covered by a protecting alumina layer. Trimming is done by implanting and etching the alumina. For a first experiment an alumina layer of 50 nm was deposited in the regular fashion, i.e. perpendicularly to the sample surface. However, due to the bad alumina coverage of the waveguide sidewalls gallium atoms reach the silicon during trimming, which leads to losses. For a second experiment alumina was deposited both on the top surface and on the sidewalls by double angled deposition.

5.4.1 Single alumina layer

This experiment was performed ex situ. First 50 nm of alumina (Al_2O_3) was deposited on the sample by electron beam evaporation. This is the standard hard mask deposition technique that was also used in previous experiments. Then a racetrack resonator with bend radius of 4 μm was measured and trimmed sequentially. Trimming was performed by scanning the ion beam (with a current of 50 pA)

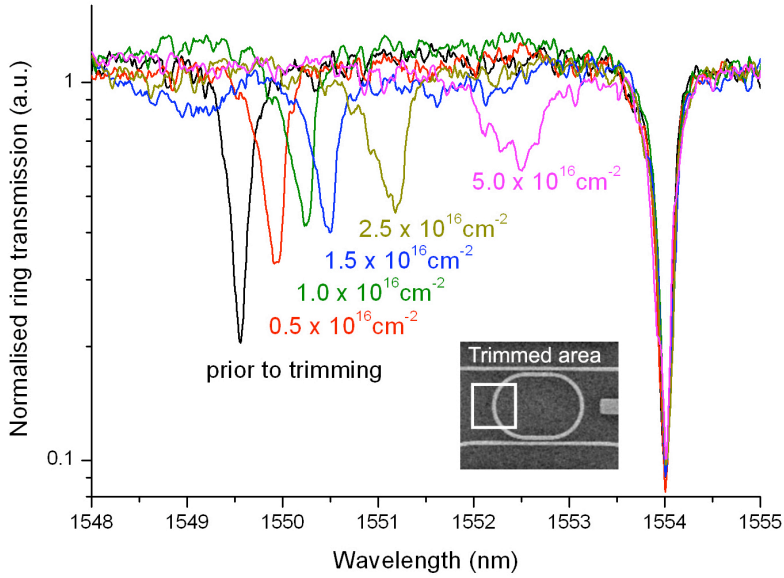

Figure 5.4: Trimming of a ring by etching a deposited 50 nm alumina layer leads to deterioration of the Q value by implantation into the poorly covered waveguide sidewalls.

over a 5×5 μm square located in the middle of a bend section, as depicted in the inset of Fig. 5.4. The graph in Fig. 5.4 represents the consecutive measurements of the transmission through both the reference and the trimmed ring. The position of the curves was adjusted by setting the position of the reference resonance to the value of the first measurement. Furthermore the spectra were normalized. The graph shows a red-shift and a clear Q value deterioration of the resonance (as also shown in Fig. 5.5). This was not expected due to the protecting properties of alumina (see Fig. 4.1). However, we have observed in cross-sectional micrographs that the alumina layer on the sidewalls of wire waveguides is not continuous (see Fig. 4.25). Therefore we believe that the significant deterioration of the Q value is caused by ion implantation into the waveguide sidewalls.

Removal of alumina on top of the waveguide leads to a lower effective index, and thus a blue-shift of the resonance wavelength. From the observed red-shift it is clear that the trimming is dominated by other effects. This will be discussed later.

The observed deviation of the reference ring for this experiment (not shown in the graph) was about linear with the etch dose of the trimmed ring and amounted up to about 1 nm. It is unlikely that

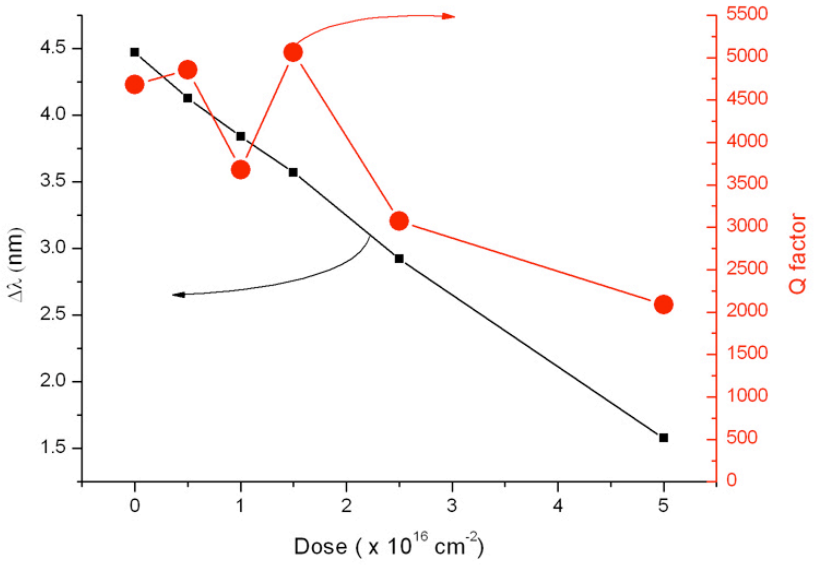

Figure 5.5: Evolution of the wavelength and Q value of the trimmed resonator.

this deviation was caused by a temperature difference (about 10°C). Therefore we believe that the reference ring was unintentionally altered by the ion beam (e.g. by imaging).

5.4.2 Double alumina layer

To avoid implantation into the sidewalls a sample was prepared with a double alumina layer. Two consecutive alumina depositions were performed, both at an angle of 45° with respect to the surface normal. The sample was oriented in such a way that the bend sections of the racetrack resonator (here with bend radius of 3 μm and straight sections of 3 μm) are covered on all sides, whereas the straight sections have poor alumina coverage on the sidewalls. This is indicated in Fig. 5.6. Both angled depositions were performed with identical parameters as for a perpendicularly deposited 50 nm layer. The expected layer thickness on top of the waveguide is therefore $2 * 50/\sqrt{2} \sim 70$ nm. The ring is trimmed by etching with a 50 pA ion beam current on two 3 μm $\times$ 3 μm squares, centered on the bend sections.

The sequentially measured spectra (ex situ trimming) are presented in Fig. 5.8. The spectra are normalized and shifted for iden-

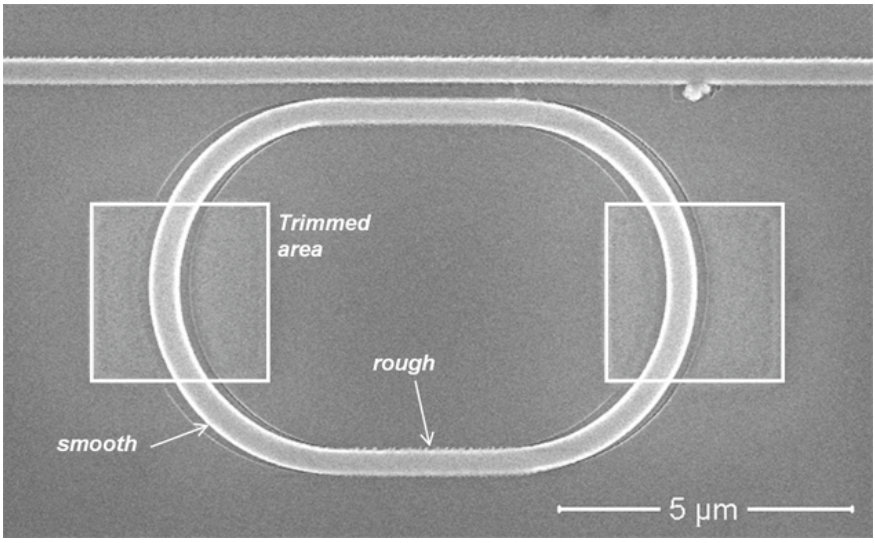

Figure 5.6: Two consecutive alumina depositions lead to good coverage in the bend sections and poor sidewall coverage in the straight sections. Trimming was done by etching inside the squares in the bend areas.

tical position of the reference ring (less than 0.3 nm in this case). The resonance moves to shorter wavelengths after the first trimming step and moves back to longer wavelengths after further etching. The evolution of both the wavelength and the Q value are displayed in Fig. 5.7. Although the deterioration of the Q value is less pronounced compared to the previous experiment (considering the higher dose) it is higher than expected. This will be discussed in the next paragraph.

5.4.3 Discussion

As mentioned the resonance wavelength of a racetrack resonator covered with alumina is expected to shift to shorter wavelengths when the alumina layer is thinned down. The amount of required thinning was estimated by a calculation with a mode solver. When the alumina layer on top of a 500 nm wide and 220 nm high silicon waveguide (on top of oxide) changes from 50 nm to 40 nm, the effective index of the supported ground mode changes by 0.13%. This would lead to a blue-shift of about 2 nm.

We estimated the ion dose required to remove 10 nm of alumina by etching away a 70 nm thick layer; to remove the entire 70 nm layer

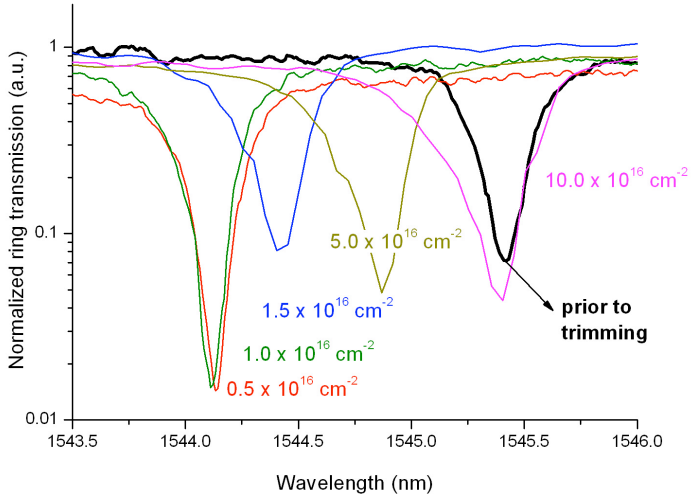

Figure 5.7: Evolution of the wavelength and Q value of the trimmed resonator with double alumina layer.

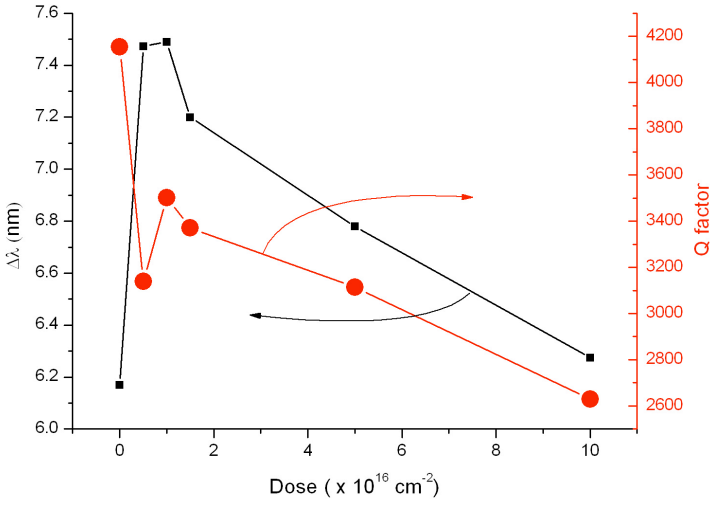

Figure 5.8: The ring with double alumina layer shifts first to lower and then back to higher wavelengths due to FIB trimming.

a dose of about 4×10^{17}cm^{-2} was needed. Therefore, for an etch dose of 0.5×10^{16}cm^{-2} (which was the applied dose after the first step in both presented experiments) we expect a blue-shift of 0.2 nm.

In the first experiment (single layer) we have measured a red-shift after the first step of about 0.3 nm, in the second experiment (double layer) a blue-shift of more than 1 nm (in this case the reduction of 70 nm to 60 nm would lead to only 0.14 nm blue-shift). Consecutive steps gave rise in both experiments to red-shift and reduction of the Q value. However, the first experiment shows a much higher sensitivity to ion impact (3 nm red-shift after an etch dose of 5×10^{16}cm^{-2}) than the second experiment (about 1 nm red-shift after 10×10^{16}cm^{-2}).

We therefore argue that implantation of alumina with gallium leads to a higher refractive index and more optical loss in the alumina. This effect is larger than the expected blue-shift due to material removal. It is likely that the blue-shift observed in the first step of the second experiment is caused by a small dust particle that is removed from the ring by the air flow in the vacuum chamber or during handling. We also argue that the amount of red-shift and optical loss in the first experiment is higher due to the sidewall implantation that makes silicon amorphous. We have simulated that the expected red-shift due to a 10 nm amorphous silicon layer on the waveguide sidewall (n$\sim$3.7) causes a 3.5 nm red-shift.

We conclude that the optical loss of gallium implanted alumina is not sufficiently low for trimming purposes. Furthermore the expected blue-shift is canceled out by red-shift that is most likely caused by the slightly higher refractive index of gallium implanted alumina.

5.5 Electron beam trimming

5.5.1 In situ experiment

During the in situ electron beam trimming experiment a ring resonator was trimmed in three subsequent steps, as depicted in Fig. 5.9. In a first step we have scanned a 0.21 nA beam across a 25.6 μm $\times$ 22.1 μm area for 360 s, and measured a resonance wavelength red-shift of 1.24 nm. In the next step the same beam was scanned over the same area for 300 s to reach an extra shift of 0.82 nm. In a final step a 0.84 nA beam was scanned over a 17.1 μm$\times$14.8 μm area for 400 s, leading to a subsequent shift of 2.77 nm. In total this leads to a 4.91 nm red-shift of the resonance wavelength of the silicon race-

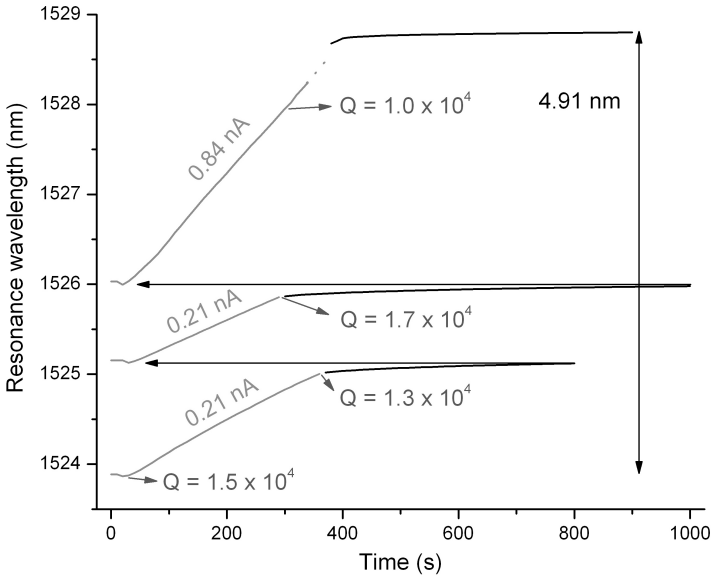

Figure 5.9: Three subsequent steps were used to equate the resonance wavelength of the trimmed resonator with that of the reference resonator. The curves represent the position of the fitted lorentzian peak maxima. The grey lines indicate the actual electron beam irradiation; the black lines show the settling after irradiation. The dotted grey line is the region where both resonance peaks merge and our single peak fitting algorithm yields inconclusive results. The Q-factors of the trimmed ring during the three steps of the experiment were extracted from the measured spectra.

track (with bend radius of 4 μm and straight sections of 3 μm). Fig. 5.9 shows the evolution of the resonance peaks, extracted from the measured spectra (one spectrum was measured every 10 s). In the final step the resonance wavelength of the trimmed ring was equated with that of the reference ring.

To evaluate the propagation losses we have extracted the Q-factors from the measured spectra, as depicted in Fig. 5.9. It is clear that the Q-factor slightly decreases in the third step of the experiment, which is also visible in Fig. 5.10. We argue that the increase during the second step is caused by a varying coupling constant, whereas the decrease in the third step is caused by increasing propagation losses. It is clear from the graph that in the beginning of the electron beam exposure there is a small blue-shift of the resonance (between 100 pm and 200 pm blue shift in our experiments), and after the ex-

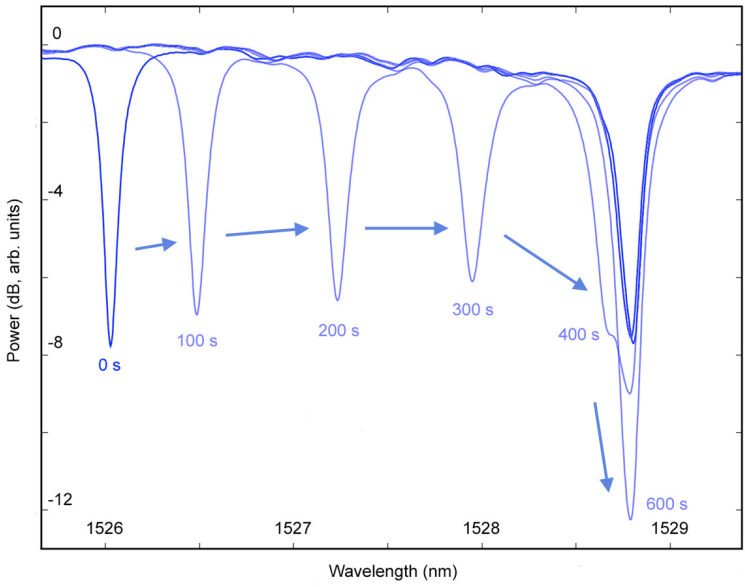

Figure 5.10: Evolution of the resonance during the third stage of the *live* electron beam trimming experiment. The Q-factor of the trimmed ring decreases from 1.7×10^4 at 1526 nm to 1.0×10^4 at 1528 nm.

posure there is settling of the peak towards longer wavelengths (we have measured 153 pm red shift, 45 minutes after the second step). We argue that this is caused by charging of the oxide and subsequent generation of carriers in the silicon. It was reported [103] that compacted silica tends to relax over a period of tens of hours after irradiation. However, we have measured a subsequent red-shift of 0.15 nm, 5 days after the actual irradiation.

5.5.2 Ex-situ experiment

A similar experiment was performed ex-situ, by subsequent measurement and trimming. The evolution of the resonance wavelength and the Q factor of the trimmed resonator are plotted in Fig. 5.11. The spectrum of the reference and trimmed ring were measured 16 times, represented by the black squares in the graph. The squares are grouped by three segmented lines, representing the three different days during which the experiment was conducted. As mentioned before, a subsequent red shift occurs after trimming in a period of hours to days (order of magnitude 100 pm). This effect was not in-

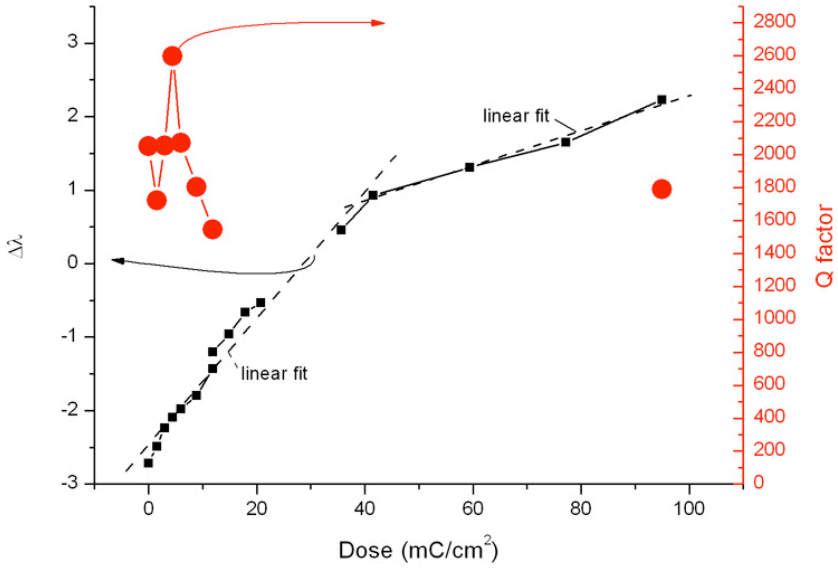

Figure 5.11: Evolution of resonance wavelength and Q factor during the ex-situ experiment. For more details see text.

corporated in this measurement and can explain the deviations from linear behavior. No data points are plotted where the transmission dips of the reference ring and the trimmed ring overlap and only one dip is visible. This can be seen on the transmission spectra shown in Fig. 5.12. These spectra are normalized, vertically shifted and shown on a logarithmic scale. Fig. 5.11 also shows two dashed lines representing linear fits for two sets of operating conditions. In the lower dose range an electron beam current of 0.14 nA was used (measured with a faraday cup) to scan an area of 25.6 μm$\times$22.1 μm. For an irradiation of 60 s this leads to a dose of 1.48 mC/cm^2. In the higher dose range we shifted to a higher electron beam current of 0.56 nA for the same writefield. The Q factors were extracted by fitting a lorentzian curve to the transmission dips, and are depicted as circles in Fig. 5.11. The Q factor after a red-shift of about 5 nm is similar to before the trimming experiment, which suggests that only limited optical losses are induced.

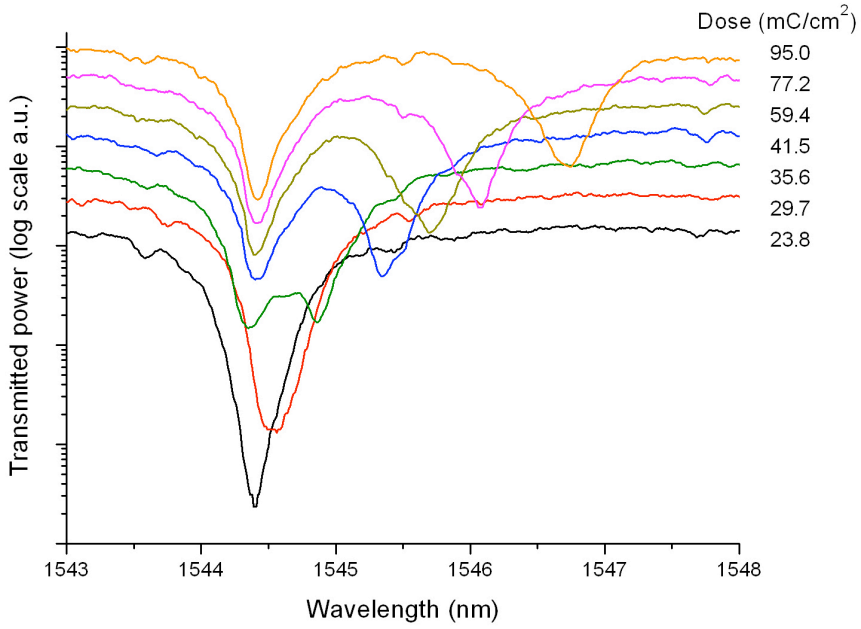

Figure 5.12: Transmission spectra of the second half of the ex-situ electron beam trimming experiment.

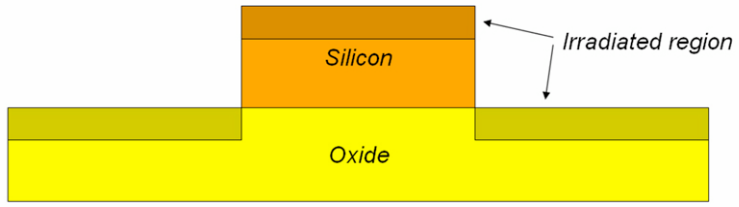

Figure 5.13: Cross-section of the 220 nm thick silicon ring resonator. The 2 keV electrons penetrate 70 nm into silicon and oxide, and lead to volume compaction only in the oxide next to the ridge.

5.5.3 Discussion

Refractive index change caused by compaction

Two distinct physical processes cause the effective index change of the mode in the silicon ring resonator. The first is a larger refractive index of the oxide cladding due to volume compaction; the second is the stress this oxide compaction induces in the silicon lattice. In our experiment we have worked with 2 keV electrons, which have a penetration depth of about 70 nm in Si and SiO_2 (this was calculated with Monte Carlo simulations, and confirmed by [103]). The silicon ring is 220 nm thick, on top of a 2 μm oxide layer; therefore the electrons can not penetrate the silicon and irradiate (and compact) the silica only next to the ridge, as depicted in Fig. 5.13.

Let us first estimate the order of magnitude of the expected contribution of the increasing silica refractive index. There are very few reports on the maximum attainable compaction by 2 keV electron bombardment. By extrapolating the data in Ref. [103] to the dose ranges considered in our experiments, we expect a volume compaction of less than 5%. The maximum dose of the in situ experiment can be written as 2.8×10^{23} keV/cm^3 if we assume that all the energy is deposited in a 70 nm thick layer; this is about a factor 2 higher than what was reported in Ref. [103]. To evaluate the change in the refractive index caused by this densification the Lorentz-Lorentz relation has to be considered [112], which takes into account changes in the polarizability α due to changes of the chemical bonds in the material:

$$\frac{n^2-1}{n^2+2} = \frac{1}{3\epsilon_0}\frac{\alpha}{V}. \tag{5.3}$$

From this one can derive

$$\frac{\Delta n}{n} = \frac{(n^2-1)(n^2+2)}{6n^2}\Big(\frac{\Delta V}{V} + \frac{\Delta\alpha}{\alpha}\Big), \tag{5.4}$$

where a positive volume change represents a densification. Although the polarizability increases for low compaction dose and decreases for high doses, $\Delta\alpha/\alpha = 0$ is a good approximation to estimate the order of magnitude of refractive index change in function of densification. For a refractive index of quartz glass of about 1.5, a volume compaction of 5% causes a refractive index change of 2%.

It was calculated with a mode expansion program that the mode overlap between the optical mode and the cladding next to the ridge (see Fig. 5.13) is only 1.5%. The effect of refractive index change in

the oxide can therefore not lead to more than 0.5 nm in resonance wavelength shift (with the first order approximation that $\Delta n_{eff}/n_{eff}$ = $\Gamma \Delta n/n$, where Γ represents the confinement factor).

Stress induced index change in Si

Due to the limited contribution of the cladding index change it is likely that the largest fraction of the observed resonance wavelength shift is caused by strain in the silicon lattice. Let us estimate the contribution of strain by taking into account the elasto-optical tensor of Si. One can write the change of the optical impermeability (ϵ^{-1}) in function of the strain as follows [113]:

$$\Delta\left(\frac{1}{n^2}\right)_i = p_{ij} S_j, \qquad i,j = 1,2,\ldots,6, \tag{5.5}$$

where p_{ij} is the elasto-optical tensor and S_j is a dimensionless array that represents the strain and shear components (with the convention that tensile strain is positive). The six components of the impermeability (i=1,...,6) represent the six independent components of the symmetric 3×3 tensor. For material systems with cubic symmetry the elasto-optic tensor has only three independent coefficients:

$$p_{ij} = \begin{pmatrix} p_{11} & p_{12} & p_{12} & 0 & 0 & 0 \\ p_{12} & p_{11} & p_{12} & 0 & 0 & 0 \\ p_{12} & p_{12} & p_{11} & 0 & 0 & 0 \\ 0 & 0 & 0 & p_{44} & 0 & 0 \\ 0 & 0 & 0 & 0 & p_{44} & 0 \\ 0 & 0 & 0 & 0 & 0 & p_{44} \end{pmatrix}. \tag{5.6}$$

For this calculation the axis are chosen such that the three off-diagonal components of the impermeability (i=4,5,6) equal zero[1]. We will use the p_{11} and p_{12} coefficients for silicon at a wavelength of 1.15 μm (from Ref. [113]):

$$p_{11} = -0.101, \qquad p_{12} = 0.0094.$$

When the oxide next to the silicon ridge is compacted due to the electron bombardment it will contract. However, it can only do so in the vertical direction. Therefore the dominant direction of the remaining stress and strain is in the plane of the substrate surface. The

[1] X-axis perpendicular to the propagation direction and in the substrate plane, Z-axis in the propagation direction. For more background we refer to Ref. [113]

stress in the oxide layer is tensile, and it will put the silicon ridge under tensile stress as well. Let us suppose a tensile strain in the 70 nm oxide layer of 1% and estimate the expected resonance wavelength shift. We make the rough estimation (in two dimensions) of the silica being a 70 nm wide string (with Young's modulus of 73 GPa) that puts the silicon (a 220 nm thick string with Young's module 150 GPa) under tensile stress from both sides. Under these approximations it becomes clear that the silicon is under less strain than the oxide cladding: a factor two for the difference in modulus and a factor 3 for the difference in width. Furthermore the oxide under the silicon conducts part of the stress. Altogether we can estimate that the average strain in the silicon is about an order of magnitude lower than in the oxide, i.e. 10^{-3}.

Considering that the silicon lattice is stretched in one dominant direction (parallel to the substrate surface), that the p_{12} is much smaller than p_{11}, and that the propagating quasi-TE mode has its electric field primarily along the X-axis, Eq. (5.5) becomes

$$\Delta\left(\frac{1}{n^2}\right)_x = p_{11}S_x. \tag{5.7}$$

After some manipulation this gives (with the convention $n_x = n$)

$$\frac{\Delta n}{n} = -\frac{n^2}{2}p_{11}S_x. \tag{5.8}$$

This leads to a resonance wavelength shift of

$$\Delta\lambda = -\lambda\frac{n^2}{2}p_{11}S_x, \tag{5.9}$$

which yields an estimated wavelength shift of

$$\Delta\lambda \sim 1\ nm, \tag{5.10}$$

for a silicon strain of 10^{-3} resulting from a 1% compaction. This supports the fact that tensile strain in the silicon waveguide can account for the observed wavelength shift of about 5 nm (since the expected volume compaction was 5%).

This was also verified with finite elements simulations (performed in COMSOL[2] with a variable mesh size, down to 10 nm where a large stress gradient is reached), as shown in Fig. 5.14. The overlay picture illustrates the deformed mesh (with a scale factor of 2 for

[2] see Appendix D

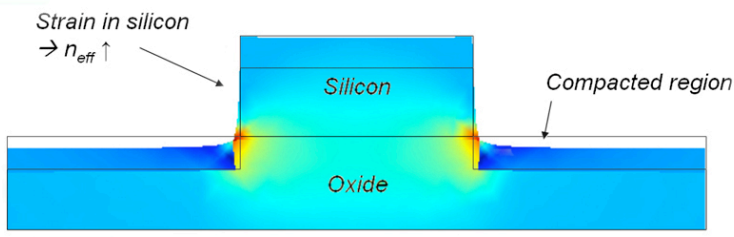

Figure 5.14: The oxide compaction next to the ridge generates a tensile strain in the silicon, parallel to the substrate. This figure shows the first principal strain obtained from a finite element simulation. Color key: dark blue = compressive strain 0.05; red = tensile strain 0.17; light blue as in the edges of the substrate represents strain 0.

better visualization) and the first principal strain in the case of a 10% compacted oxide layer with a thickness of 70 nm. The stress in the silicon lattice is between 1 and 3 GPa tensile, which is of the same order of magnitude than what can be achieved by depositing straining layers, such as demonstrated in Ref. [114] for the enhancement of the $\chi^{(2)}$ non-linearity in silicon. This mechanism of compaction induced stress can therefore also be used to fabricate modulators in silicon.

It was reported [112] that the induced stress in the compacted oxide layer saturates upon high dose electron beam irradiation. However, we have not found reports of this effect for the energy and dose range considered in our experiments. Since a complete study was beyond the scope of this work, we have chosen to estimate the influence of compaction induced stress on the effective index of the supported modes without detailed simulations of the optical mode profile in the strained lattice. We have therefore calculated the average silicon strain in the dominant direction: perpendicular to the waveguide propagation direction and in the plane of the substrate surface. The resonance wavelength shift was calculated by using only the p_{11} component of the silicon elasto-optical tensor. This shift is calculated for varying oxide compaction rates and for three different compacted layer thicknesses (50, 70 and 100 nm). The results, displayed in Fig. 5.15, confirm the order of magnitude that we have estimated with the simplified model, and also confirm that the compaction induced strain is the dominant trimming effect.

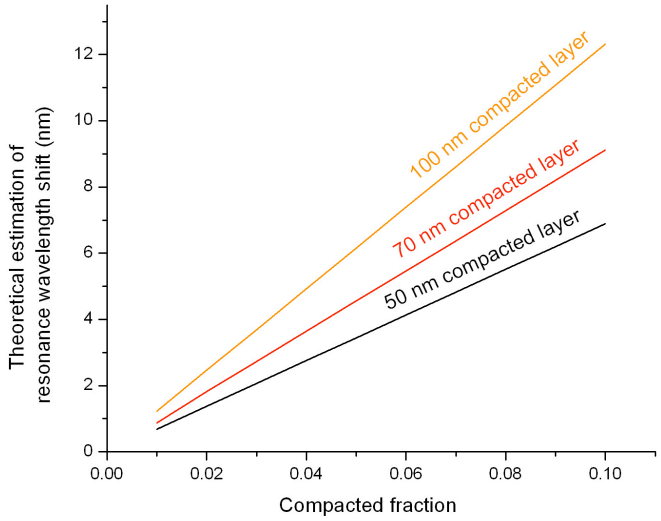

Figure 5.15: Calculated resonance wavelength shift due to strain in the silicon lattice, for varying volume compaction and different compacted layer thicknesses. From this estimation it can be concluded that compaction induced stress can account for the measured resonance wavelength shift of about 5 nm.

Although all experiments in this report were performed with an electron beam, they can in principle be repeated with UV since the penetration depth at wavelengths between 200 nm and 400 nm is sufficiently low to create compaction induced strain. Ring resonators in other semiconductor materials can be compacted in a similar way, as well as other kinds of cavities, such as photonic crystal cavities.

Trimming efficiency

In both the in situ and ex situ experiment we have seen a different trimming efficiency for various beam currents and irradiated areas. To compare the results we will convert the trimming speed - or efficiency - to units of resonance wavelength shift per unit of applied dose. This takes into account the beam current and the irradiated area, and is therefore a measure of the physical trimming efficiency, which we expect to be independent of experimental conditions. The results are presented in Table 5.1.

It is clear that the trimming efficiency for both discussed experiments is of the same order of magnitude; and they are in both cases

	irradiated area (μm^2)	beam current (nA)	trimming efficiency ($pm/mC.cm^{-2}$)
in situ step 1	25.6×22.1	0.21	86
step 2	25.6×22.1	0.21	76
step 3	17.1×14.8	0.84	22
ex situ step 1	25.6×22.1	0.14	86
step 2	25.6×22.1	0.56	24

Table 5.1: Comparison of the experimental conditions in the discussed experiments. The trimming efficiency, given in the right column, varies by a factor of 4, although it should be independent of experimental conditions.

lower for higher beam currents. Although a difference in trimming efficiency for racetracks with different geometries can be expected because the generated strain in coupling section and bends are different, this observation is in contrast with the expected independence of exposure parameters. This deviation from linear behavior is possibly caused by a difference in secondary electron yield or the current leakage through the oxide cladding, that causes a higher charge buildup on the sample surface. This results in more reflected electrons and a reduced effective exposure current. This effect needs further investigation; it might for instance be alleviated by providing conductive paths near the exposed region.

Reproducibility

A number of experiments was carried out ex situ by performing electron beam trimming inside the vacuum chamber of both a tungsten filament SEM and the field effect SEM in the FEI system. The samples were taken outside the clean room and transported to the measurement facilities elsewhere. We have found that these measurements were not predictable and not reproducible. We believe that this is caused by dust particles that attach or detach from the ring resonators during the sample handling. This explains why the experiments inside the clean room were successful.

5.6 Conclusions

We have investigated trimming of silicon photonic devices, more in particular racetrack resonators, by FIB and electron beam trim-

ming. To avoid large optical losses FIB trimming was performed by etching a protective alumina top cladding. Nevertheless, the experiments show optical loss, most likely due to absorption in gallium implanted alumina. We can conclude that FIB is not adequate for *live* trimming of silicon photonic devices with low optical losses.

Therefore we have explored an alternative trimming approach utilizing electron beam compaction of the oxide cladding layer. This compaction causes strain in the silicon lattice, which accordingly changes its refractive index. The experimentally demonstrated trimming range of about 5 nm is more than sufficient to correct for imperfections of deep-UV fabricated silicon photonic devices. Although some issues need to be resolved we believe that this effect is a good candidate for industrial deployment. More specifically in combination with fiber probes [84] this trimming approach is compatible with wafer scale testing and trimming.

The work presented in this chapter is the subject of one publication in scientific literature (Appendix A.2 #4) and one patent application (Appendix A.1 #1).

Chapter 6

FIB fabrication of imprint molds

An interesting application of FIB is the fabrication of imprint molds. This approach circumvents the damage and optical losses introduced by FIB milling, and allows full utilization of the three dimensional nano-patterning potential of FIB. Furthermore, since one mold can be reproduced many times the inherent inconvenience of FIB as being a serial technique and thus slow is bypassed. The combination of FIB and imprint is therefore natural and can be adopted for high volume fabrication of devices. In this chapter we present the design and fabrication of a refractive wedge structure that is used for perfectly vertical coupling to and from silicon waveguides. We will investigate whether the required optical smoothness and flatness of planes can be obtained. A potential application of these wedges is the flip chip bonding of vertical cavity emitting lasers on silicon photonic integrated circuits.

6.1 Application: a refractive polymer wedge

We have introduced the concept of grating couplers in Section 4.2. This approach, where light is coupled vertically or near-vertically out of a silicon chip, is an interesting alternative to horizontal coupling schemes because it enables wafer scale testing of optical chips. Furthermore, since the size of the couplers is equivalent to the size of a single mode fiber core, the required alignment precision is less

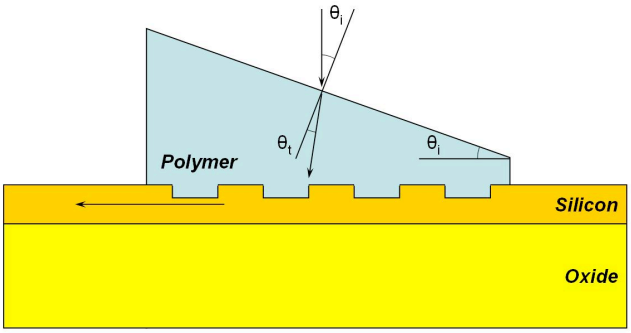

Figure 6.1: Principle of a polymer grating wedge: vertically incident light is refracted to near-vertical incidence, which is optimal for coupling with low reflections into a silicon waveguide.

stringent than in horizontal coupling schemes where lenzed fibers or fibers with reduced core diameter are often used [64].

However, as we have mentioned before, the approach of vertically coupling with a diffractive grating has several inconveniences, some of which have been solved recently. A first inconvenience is the limited efficiency of coupling fiber and silicon waveguide modes. This was recently addressed by incorporating a metal bottom reflector [81], by using a thicker silicon membrane in the grating area [82] or by etching slanted slits (Chapter 4). A second inconvenience is the need for an adiabatic taper that is typically 500 μm long. Recently the use of focusing grating structures was reported, reducing the taper length to less than 70 μm without efficiency penalty [78].

The final inconvenience is the need for near-vertical coupling to avoid reflections while coupling in and out of the silicon integrated circuit. If a grating would be designed for perfectly vertical coupling, the second Bragg diffraction order would cause large reflections. This can partially be overcome by using a thin slit adjacent to the grating, with the purpose of achieving destructive interference for the second order Bragg reflection, as was theoretically shown in Ref. [115]. Another approach was presented in Ref. [116], where a DBR type mirror is placed behind the grating. However, these approaches are not completely satisfactory because reflections are only canceled in a narrow wavelength range. Perfectly vertical coupling potentially opens opportunities for bonding of vertically emitting III-V sources and simplifies packaging and wafer-scale diagnostics.

In this chapter we present design and fabrication of a polymer wedge to refract the first Bragg diffraction order to a vertical wave that couples to a vertically positioned fiber, and vice versa. The principle is shown in Fig. 6.1. Reflections are avoided due to the near-vertical Bragg diffraction. The polymer wedges were fabricated by imprint lithography of a FIB fabricated mold as described later. This procedure is suited for wafer scale fabrication of devices and enables flip-chip bonding of VCSELs on photonic integrated circuits. The approach of bonding of finished III-V devices is currently being used in industry to provide light sources on passive material platforms such as silicon, nitride or silica. However, the coupling (usually of horizontal cavity lasers) often requires slanted edges or angled mirrors that can not be fabricated with typical high-volume fabrication technologies (although they can be fabricated with FIB, as described in Chapter 7). The technique presented in this paragraph envisages the use of VCSELs that inherently emit perfectly vertically and do not require extra mirrors or facets. The polymer wedge and grating couple this perfectly vertical light into the silicon circuit without reflections. Due to the compatibility with high volume manufacturing we believe that this approach is viable for industrial deployment.

In the following sections we will present the design of the wedge using FDTD simulations, the mold fabrication by FIB etching, the imprint replication of the wedges, and the optical measurements of the device.

6.2 Design

The numeric calculations for this design were performed by FDTD in the software package Omnisim (see Appendix D). The refractive polymer element was placed on top of a previously designed grating coupler with 20 rectangular slits of 315 nm wide and 70 nm deep, spaced by 315 nm. This coupler is etched in a 220 nm thick silicon layer on top of a 2 μm thick oxide buffer layer. All simulations were performed in 2D, which is a good approximation for the 10 μm wide waveguides used in the experiments.

In a first step we have calculated the angle under which 1.55 μm light couples out of the silicon waveguide if the grating is completely covered with polymer (refractive index 1.506 of PAK polymer): 8.6 ° relative to the surface normal. This angle is different from the orig-

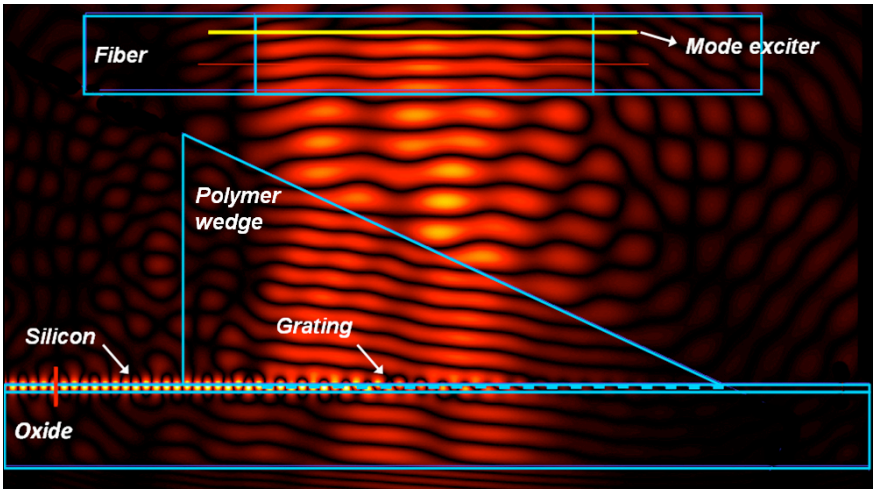

Figure 6.2: FDTD simulation of the polymer wedge with an angle of 24.7°.

inally designed 10° due to the altered effective index of the optical mode.

In a second step we have manually calculated the angle θ_i (see Fig. 6.1) by solving the equation $\theta_i - \theta_t = 8.6\ °$ and snell's law. After some manipulations one obtains $\theta_i = 24.7\ °$. This design was verified with FDTD in Omnisim[1], as depicted in Fig. 6.2. In this picture the mode is excited from the fiber; this setup was used to calculate the power fraction that is coupled between fiber and silicon waveguide. For a standard grating coupler with fiber positioned at 10° off-normal the obtained coupling efficiency is 43%; with the setup as depicted in Fig. 6.2 (wedge angle 24.7°) the coupling efficiency is 49% (both simulations were done with a grid size of 15 nm). This means that theoretically we expect a small increase in efficiency. We have verified this with a calculation of Fresnel's equations, and found that the insertion of a polymer wedge in principle reduces the power reflection of a vertically incident plane wave from 30% to 20%. This increase is somewhat compensated by a decrease of the grating efficiency due to a different angle and index contrast.

To estimate the amount of reflected light we have performed a simulation with mode excitation in the silicon waveguide. Fig. 6.3 shows the power fraction coupled upwards (without taking fiber mode overlap into account), downwards into the substrate, back into the waveguide, and through the grating. Reflections are be-

[1]See Appendix D

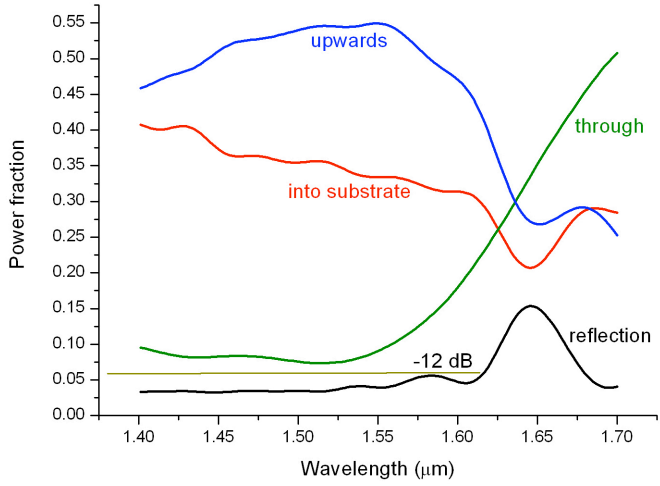

Figure 6.3: By mode excitation from the silicon waveguide we have calculated the power fractions coupled upwards, downwards into the substrate, back into the waveguide, and through the grating coupler.

low -12 dB for wavelengths up to 1616 nm. However, it should be noted that the expected experimental reflections are lower, because scattered light in the wedge creates a noise background during the simulation. By artificially shielding the detector with a thin gold stripe we have obtained a reflection lower than -20 dB. This reflection can in principle be reduced by designing the grating couplers for operation at off-normal angles greater than 10 °.

6.3 Fabrication

6.3.1 Mold fabrication by FIB

The general fabrication scheme (as presented in Fig. 6.4) involves a number of steps that will be discussed in more detail in the following.

Firstly, a mold for imprinting a structure in UV curable polymer on silicon is necessarily transparent to UV radiation, so we have chosen a quartz substrate. However, to avoid charging problems during FIB etching of the wedge molds the quartz substrate was first covered with a 100 nm layer of Ti that was electrically connected to the sample stage in the FIB vacuum chamber during etching. Op-

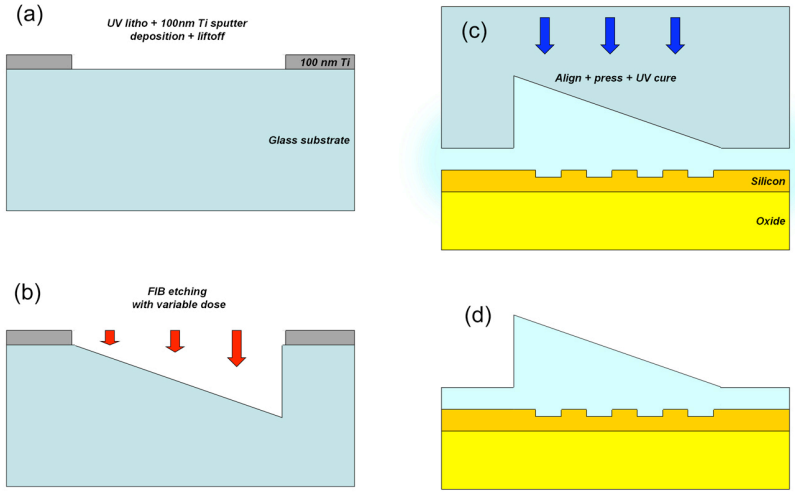

Figure 6.4: Schematic overview of the wedge fabrication procedure: (a) definition of wedge locations by optical lithography; (b) FIB etching of the wedges; (c) imprint of the wedges and curing with UV; (d) the final wedge after mold removal.

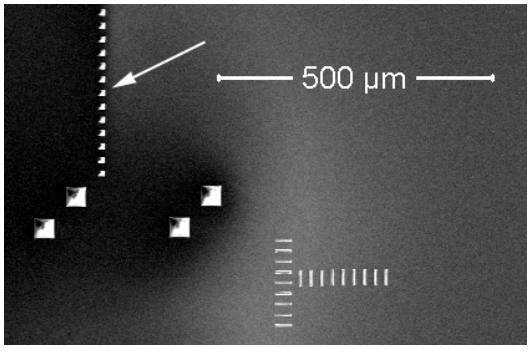

Figure 6.5: Overview of the patterned Ti layer on the quartz mold. The negative wedges will be defined in the squares indicated by the arrow. The other structures are meant for alignment during imprinting.

tical lithography and liftoff of the Ti was performed to define the locations of the wedges and to print alignment structures for the imprint lithography. An electron micrograph after this first step is displayed in Fig. 6.5, where the white arrow indicates where an array of wedges will be etched.

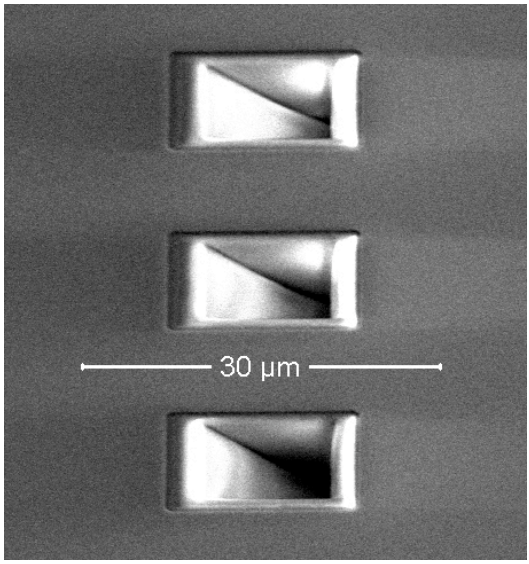

Figure 6.6: The negative wedges were etched after an image recognition scan and automated alignment.

In a second step the negative wedges were etched with FIB at normal incidence (7 nA, 30 keV). Image recognition was used to align and etch 60 wedges in an automated way (about 15 minutes per wedge). Three of these wedges are presented in Fig. 6.6. The precisely angled and smooth bottom of the wedge molds was obtained by varying the dose in the etched rectangle. The mask consists of an array of 160 lines, 100 nm apart and 14 μm long. These are scanned digitally, with a step size of 200 nm and a varying dwell time (from 1.2 mC/cm^2 to 30.965 mC/cm^2 with a step of 0.1872 mC/cm^2). This procedure was repeated 60 times; so the dose of the deepest line was 1.86 C/cm^2. This process was conducted with the Raith scan generator connected to the FEI system. Optimization of this procedure was performed by cross-sectional inspection and iteration. We have found that the angled etch pit bottom (the optically smooth refraction plane) is no longer planar when the largest available beam current of 20 nA is used, which is most likely caused by a lesser beam quality. We have also experimented with larger wedge angles and found that angles larger than about 45° could not be obtained with smooth refraction planes. In this case we have observed the formation of ripples.

Although FIB fabrication of a mold inherently avoids the problems of optical losses, these can still be detrimental when a transpar-

ent mold is used. If too much losses (for UV transmission) would be introduced by the etch procedure, exposure would become difficult. However, we have observed no effects of this kind. No specific transmission measurements were performed, but by microscopic inspection of the mask during alignment no noticeable darkening (for visible light) was observed.

6.3.2 Wedge fabrication by imprint

The imprint work presented in this paragraph was done in collaboration with S. Scheerlinck, and is discussed in more detail in Ref. [84].

After the wedge etching the quartz mold was prepared for imprinting by performing an anti-adhesive treatment. For a first generation of wedges the patterned Ti layer and the negative wedges were first covered with a 100 nm thick layer of silica by plasma deposition. Then the mold was immersed in (tridecafluoro-1,1,2,2-tetrahydrooctyl) trichlorosilane ($C_8H_4Cl_3F_{13}Si$, ABCR GmbH) in pentane solution (0.1%) and subsequently rinsed using acetone, isopropyl alcohol, and deionized water. The thin deposited silica layer was necessary because this anti-adhesive treatment is designed for silicon oxide. An extra anticipated advantage of the patterned Ti layer is that, as the UV exposure does not penetrate the Ti layer, regions in between wedges are not exposed. This eliminates the residual layer. However, we have found that in this case the wedges are easily released from the silicon during mold removal or subsequent rinsing. In a later generation the yield was greatly increased by completely removing the Ti layer (in diluted HF) and doing the anti-adhesive treatment directly on the quartz. This leaves behind a residual layer with a thickness that depends on the applied pressure and the viscosity of the polymer.

Two different UV curable polymers were used: PAK (PAK-01 from Toyo Gosei Co. Ltd.) and SU8 (SU8-10 from MicroChem). Both were dispensed on the sample prior to alignment and pressing of the mold, and then UV exposed (performed on Karl Suss MA6 mask aligner). The SU8 resist is more viscous so a thicker residual layer can be expected. After mask removal the samples were flood exposed under a UV fiber lamp for 5 minutes. Some SEM micrographs (after deposition of a thin gold layer) are presented in Fig. 6.7. Note the smoothness of the refractive plane.

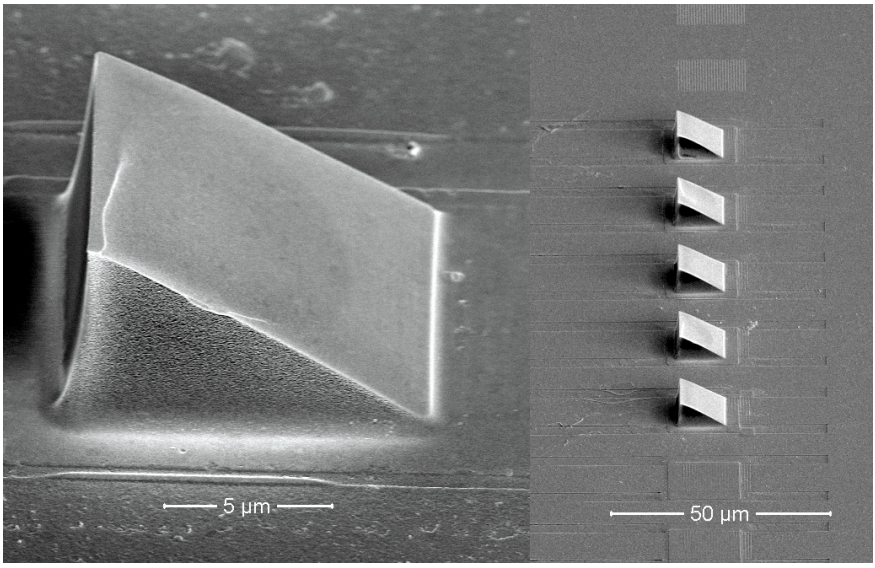

Figure 6.7: Micrographs of fabricated polymer wedges covered with a thin layer of gold to avoid charging. Note the smoothness of the refractive plane.

6.4 Measurement

To determine the coupling efficiency of the fabricated coupling structure we have used a fiber-to-fiber transmission measurement for TE polarized light from a super luminescent LED. The structure consisted of two shallow input coupler fabricated with optical lithography and polymer wedges. In the integrated circuit the light is guided by a straight 10 μm wide waveguide and tapered down to a wire with approximate width of 500 nm. First a reference measurement was performed on gratings without polymer wedge, with both fibers positioned nearly vertically (at an angle of 10°). Then, the fibers were tilted to a perfectly normal position and positioned above the gratings with polymer wedges. The measurements were performed on the second generation of wedges, where the Ti layer was removed from the mask and thus a residual polymer layer covers the waveguides. Two different samples were fabricated, one with PAK and one with SU8 polymer. Fig. 6.8 depicts the measured fiber-to-fiber coupling efficiencies for 5 different wedge pairs on both samples. Coupling with near-vertical fibers causes a loss of about 13 dB, i.e. about 6.5 dB per coupler, which is equivalent to what was reported before. The vertically positioned fibers above

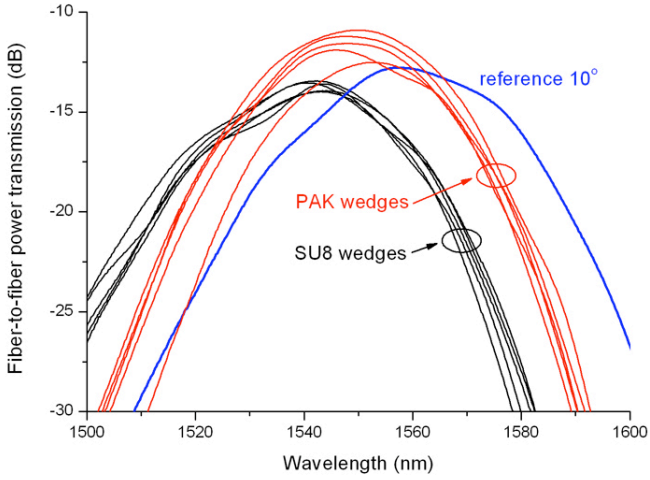

Figure 6.8: Fiber-to-fiber power transmission for 5 wedge pairs on two different samples.

the PAK wedges have a slightly higher coupling efficiency, 5-6 dB per coupler. This increase in efficiency is supported by the simulations in section 6.2. The SU8 wedges, on the other hand, show a somewhat lower efficiency. This can be attributed to a thicker residual layer (due to the higher viscosity) and possibly due to some misalignment. Nevertheless, form these results it is clear that the angled refractive planes have a good optical quality (as visible in Fig. 6.7). This proves the ability of FIB milling of optically smooth structures in quartz.

These polymer wedges enable flip-chip bonding of vertically emitting lasers. However, this process requires a thermal cycle of typically between 240 and 300°C. To asses the thermal stability of the two polymers we have therefore baked both samples for 5 minutes at 300°C on a hotplate in air. Afterwards the fiber-to-fiber transmission was measured again (this time with a tunable laser), as depicted in Fig. 6.9. The PAK polymer wedges show a significant decrease of efficiency, although the value does not drop below that of the reference couplers. The SU8 wedges show no decrease in efficiency. We can therefore conclude that SU8 polymer shows a better thermal stability, but to obtain a higher efficiency with SU8 wedges they have to be fabricated with SU8 of lower viscosity, which can be obtained by mixing with an appropriate solvent.

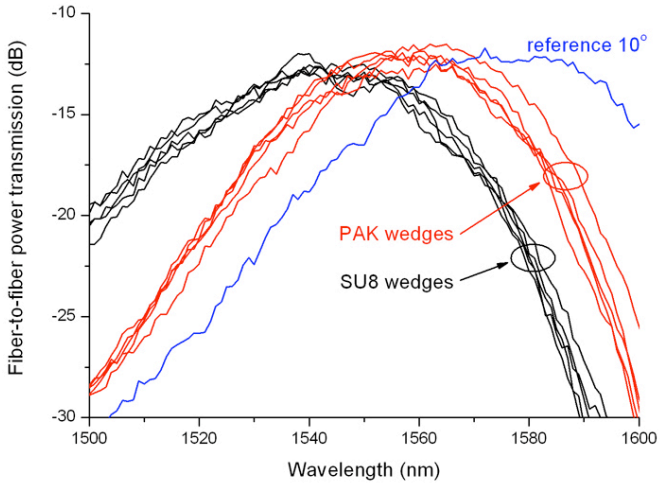

Figure 6.9: After a thermal cycle at 300°C the PAK polymer shows a slight decrease of efficiency; SU8 is stable.

6.5 Conclusions

We have successfully designed, fabricated and measured polymer wedges that enable perfectly vertical coupling to a silicon photonic integrated circuit. The wedges were fabricated by imprinting a UV curable polymer with a focused-ion-beam fabricated mold with 3D geometry. The devices were submitted to a thermal treatment at 300°C to verify the applicability of of this procedure for flip-chip soldering of vertical cavity lasers. The measurement results support that there is no coupling efficiency penalty when the correct polymer is chosen. The presented results prove the applicability of FIB for the fabrication of imprint molds with 3D geometry.

The results obtained in this chapter are subject of a patent application (see Appendix A.1 #2), and are currently under investigation for commercial deployment.

Chapter 7

FIB etching of III-V materials

In Chapter 1 we have mentioned that work was done on the device modifications and prototyping in III-V materials. In this chapter we will give a more detailed overview of literature. A number of devices was demonstrated, but the detrimental effect of FIB induced losses was often reported. The prototyping of nanophotonic devices, where the overlap of the optical mode with the FIB damaged material is more pronounced, requires loss reduction treatments. In this chapter we will present a study of FIB induces loss in both passive and active III-V devices. First we will discuss the reduction of optical losses in passive InP waveguides that were implanted with FIB. Then we will present FIB etched laser facets.

7.1 Literature overview

Horizontal laser cavity mirrors are not straightforward to make when cleaving is not an option. For example if one wants to integrate other functionality such as waveguides or splitters on the same chip as the horizontal laser cavity, the laser facets have to be etched. Making etched facet mirrors with conventional etching techniques is a challenge due to the required smoothness and steepness. On the other hand, distributed Bragg reflector (DBR) mirrors are hard to make because of the required aspect ratio (very narrow and deep trenches). FIB has the ability to make smooth and vertical sidewalls anywhere on a chip, and can be used for DBR mirrors when sufficient etch selectivity is achieved. A number of examples of such devices in various III-V material systems were demonstrated in lit-

erature. FIB was used to etch facets and DBR mirrors of visible light lasers in InGaAlP [117, 20] and GaN based systems [19, 118] (where cleaving is often impossible due to misalignment of the III-V layers with the sapphire or SiC host substrate) . Other examples include the fabrication of a low reflectance angled facet on a GaAs based super luminescent LED (broadband and high power light emitter) [119], and the fabrication of an angled facet to vertically couple light out of a horizontal distributed feedback (DFB) laser [120]. Furthermore, the FIB etching of vertical total internal reflection mirrors was adopted to make a broadband optical switch [121], and FIB etched slits were used to integrate a molecular beam epitaxy (MBE) grown quantum dot laser and modulator, and to make a coupled cavity single mode Fabry-Perot laser [120].

Vertical laser cavities have also been modified with FIB. This was done for mode control by altering the top surface; both by providing it with a photonic crystal structure [24], or by modifying the top DBR reflectivity by local FIB etching [122]. Other work has demonstrated the fabrication of vertically emitting micropillars in GaAs based material for quantum dot lasers [123].

Gratings and photonic crystals have been fabricated with FIB because the required pitches are often difficult to achieve with optical lithography and because FIB offers more flexibility than electron beam lithography. Localized implantation and etching was used to make both refractive index and gain modulating DFB gratings [18] by a damage induced wet etching technique [124]. FIB was also used to directly etch 2D photonic crystal structures in both active [125, 21] and passive [126, 49] devices.

Conclusion

These examples clearly demonstrate the flexibility of FIB as a device modification and prototyping tool. However, in most of the examples where FIB is used to alter active devices it is difficult to assess the influence of optical loss caused by FIB induced damage. That is because the device operation is changed to such an extent that comparison is often difficult. The only laser devices that allow a simple evaluation of the losses are Fabry-Perot lasers where one facet is polished with FIB. Nevertheless, from the presented examples in literature it is clear that the FIB induced losses for active devices are

not dramatic if sufficient pumping can be obtained to compensate for the losses. This is often not the case for nanophotonic devices. For passive devices the optical losses can be evaluated by simple transmission measurements, but they are usually not presented because of the high losses. Similarly to what was discussed in Chapter 3, gas etch enhancement can be used to increase the photo luminescence signal of active material [72, 73] or reduce the optical losses of passive structures [49].

It can be concluded that two types of experiments are desirable to clarify the issue of FIB induced optical losses in III-V materials: losses induced by implanting and etching predefined passive waveguides; and losses induced by polishing a facet of a Fabry-Perot laser cavity. These experiments were both performed in this work, with the main focus on InP based material systems due to its compatibility with telecom wavelengths. They are presented in the following two paragraphs.

7.2 Implantation of passive InP waveguides

To investigate the optical losses of FIB etched passive InP we have done similar experiments as presented in Chapter 3. Passive InP waveguides with geometry depicted in Fig. 7.1 were defined by optical lithography and ICP etching[1]; the indicated dimensions were verified by imaging a cross-section. They were then implanted and etched by scanning the ion beam across the top surface, either with or without iodine etch enhancement, as will be discussed later. Finally 1 mW polarization controlled light (with the electric field component in the substrate plane) from a tunable laser was horizontally coupled to the waveguide and projected onto a photodetector (the waveguides show single-mode behavior). The optical loss of the waveguides was extracted from the Fabry-Perot transmission spectrum; the loss per unit length was obtained by linear regression of the loss in waveguides with different implanted length sections.

After either direct or iodine enhanced etching we have reduced the losses by a number of different treatments, such as baking and selective wet etching. First we will present the optical loss measurements for these different treatment, and later we will discuss the loss reduction mechanisms.

[1]The fabrication was done by St Andrews University in the framework of the European project ePIXnet.

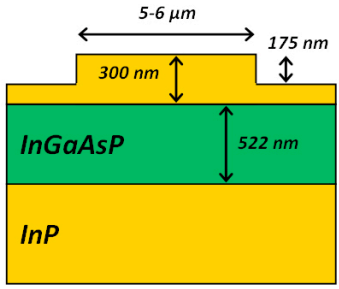

Figure 7.1: Geometry of the passive InP implanted waveguides: a 300 nm top InP cladding is etched 175 nm deep; the core layer is 522 nm thick lattice matched InGaAsP with Q=1.22 (bandgap 1.02 eV); the ridges are 5 to 6 μm wide.

7.2.1 Loss measurements

Two identical samples were prepared with directly etched waveguides (no gas enhancement) and two with iodine gas enhancement; one of each set was then baked for 30 minutes at 300°C on a hotplate in nitrogen prior to the optical measurement. The etching was done by scanning the ion beam on 20 μm wide rectangles with different lengths: 50, 100, 150, 200 and 250 μm, with a 300 pA ion beam and a dose of 5×10^{15} Ga^{+}/cm^{2} (both with and without iodine enhancement). Alignment of these rectangles on the waveguides was done without imaging with the ion beam, but by working on the coincidence point of electron and ion beam. The magnification was chosen in such a way that no stitching was necessary; and we used a beam defocus to obtain a beam diameter of about 200 nm. The etch depth after direct etching was determined with a profilometer: 10 nm. After iodine enhanced etching the etch depth was about 200 nm, which means that the top InP layer next to the ridges is completely removed, which was confirmed by the appearance of the arsenic peak in an EDX measurement[2]. After measuring the two directly etched samples (one with and one without thermal treatment) were both etched for 3 minutes in a wet etch bath of 1:1:18 parts of H_2SO_4:H_2O_2:H_2O and measured again. This etch mixture does not etch crystalline InP, but potentially etches damaged and amorphous InP.

[2] see Appendix C

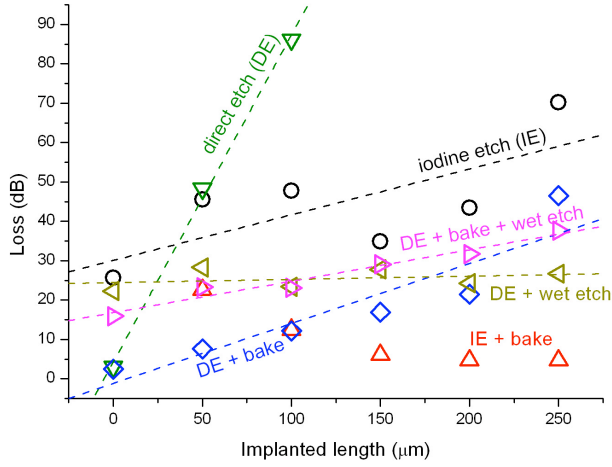

Figure 7.2: Loss measurements of directly etched (DE) and iodine etched (IE) InP waveguides after various treatments. The loss values per unit implanted length are extracted by linear regression and displayed in Table 7.1.

	Loss (dB/cm)
direct etch	8300 ± 400
direct etch + bake	950 ± 10
direct etch + wet etch	82 ± 126
direct etch + bake + wet etch	800 ± 80
iodine etch	1160 ± 550
Iodine etch + bake	< 200

Table 7.1: Loss values per unit length as extracted by linear regression from Fig. 7.2. For the last value linear regression yields negative losses; only the lowest measurement point was used.

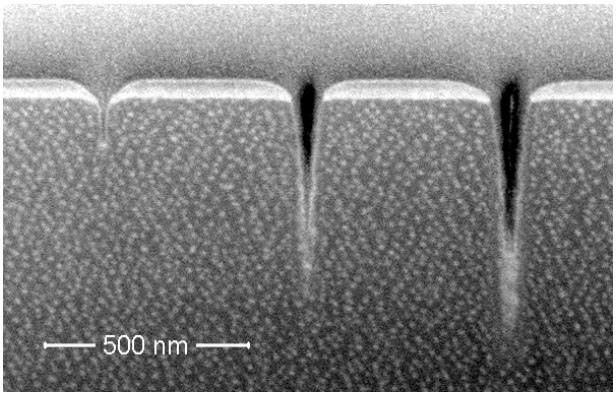

Figure 7.3: Cross-sectional image of slits through alumina on InP.

The results, as indicated in Table 7.1 and depicted in Fig. 7.2 show that both baking and wet etching reduce the losses significantly. After direct etching, baking reduces the losses, but not as much as wet etching; wet etching after baking does not significantly reduce the loss further. After iodine enhanced etching, baking significantly reduced the losses. However, it is clear that much larger uncertainty shows in these measurements, as compared to the silicon waveguides in Chapter 3. This is due to the lesser quality of the optical lithography that was used to define the waveguide ridges.

7.2.2 Cross-sections of damage removal

A different type of experiment was performed to visualize the effects of wet etching and baking for damage removal after direct etching. For this purpose we have deposited a 50 nm layer of alumina on InP. Then we have etched slits with varying depths (without gas enhancement) and visualized them by making a FIB cross-section (as depicted in Fig. 7.3). The results will be discussed in the next paragraphs.

Another cross-section was made after wet etching of identical slits, as depicted in Fig. 7.4. The sample was etched in the same mixture of sulfuric acid, peroxide and water for 3 minutes. It can be seen that there is etching under the alumina layer (of 40-50 nm in the horizontal direction) and that the slits are made deeper (by 100-200 nm).

To assess the wet damage removal after baking we did the same experiment, but with a temperature treatment (30 min @ 300°C on

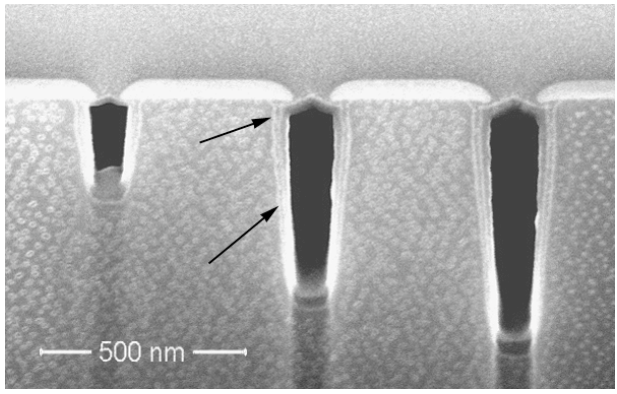

Figure 7.4: The same slits after wet etching: the damaged layer has been etched selectively. The black arrows indicate the edge of the slit; the black areas are voids created by the cross-sectioning (see Chapter 2).

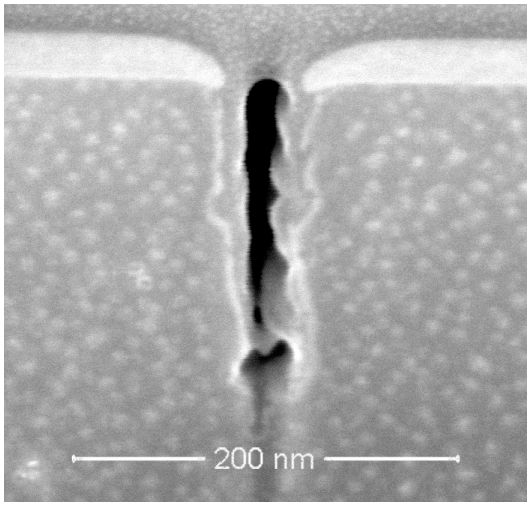

Figure 7.5: Wet etching after baking removes less material but makes the sidewalls rougher.

a hot plate in nitrogen) before the wet etching. The corresponding cross-section is depicted in Fig. 7.5. It can be seen that there is far less material removal than without the temperature treatment. However, the sidewalls have become rougher.

7.2.3 EBSD analysis

To qualitatively assess the crystallinity, a number of EBSD[3] measurements was conducted with 10 keV electrons under 70° incidence (similar to what was done on silicon in Chapter 3). From these measurements we have found that the InP surface becomes amorphous due to Ga implantation (dose 5×10^{15} Ga^+/cm^2), both with and without iodine gas enhancement. The samples were subsequently baked (30 min @ 300°C on a hot plate in nitrogen) and measured again: only baking after iodine enhancement etching partly restores the electron diffraction image (this was not the case for silicon); baking after direct etching does not restore crystallinity.

7.2.4 Discussion

Let us consider the results from previous paragraphs and discuss the different mechanisms. It is clear that direct implantation and etching leads to high optical losses. It should be noted that the sputter yield for InP is much higher than for silicon (about 6 times higher, see Table 2.1), which makes that the steady state dose is lower (see Fig. 3.6). Nevertheless, the obtained loss of 8300 dB/cm is much higher than the 3500 dB/cm for silicon waveguides. According to SRIM simulations the gallium ions are stopped in the top 50 nm layer of InP. By approximating this 50 nm damaged layer as homogeneous we have calculated a confinement of less than 0.5% of the ground mode (with a mode solver), whereas it is about 20% in a 220 nm thick silicon slab waveguide. We can thus conclude that the optical loss in gallium implanted InP is about 100 times higher (2.5 times higher loss for 40 times lower confinement) than in gallium implanted silicon, although the maximum implantation dose is expected to be a factor of 6 lower. It is clear that this experiment with lower refractive index contrast waveguides, is less sensitive to material loss (due to the lower mode overlap with the damaged region) than the high index contrast silicon devices.

In Fig. 7.2 and Table 7.1 it can be seen that baking after direct etching reduces these losses considerably, although the crystalline structure is not restored (EBSD analysis). We argue that most of this loss reduction is caused by evaporation of gallium impurities. Furthermore we have demonstrated that the losses drop to low values (82 ± 126 dB/cm) when the directly implanted waveguides are etched in the diluted mixture of sulfuric acid and peroxide. This

[3] see Appendix C

is caused by a removal of the entire damaged layer, as can be seen in Fig. 7.4. In the case where the wet etching is performed after baking, the loss reduction is less. It can also be seen in Fig. 7.5 that less material is removed, although the material did not show recrystallization after the baking (EBSD analysis). Furthermore, the rougher sidewalls may attribute to the optical loss. A similar wet etching technique was presented in Refs. [124, 18]. In this case diluted and heated HF acid is used, in combination with an ultrasonic etch bath. However, the implantation doses reported are $10^{13} - 10^{14}$ cm^{-2}, which is one to two orders of magnitude smaller than what is needed to substantially sputter InP. We have conducted some tests with the same HF wet etch process for higher doses, without noticeable material removal.

On the other hand, the use of iodine etch enhancement also substantially reduced the optical losses, as depicted in Fig. 7.2 and Table 7.1. Furthermore, baking at 300° partly restores crystallinity and further reduces the losses, similarly as we have reported in silicon. From the measurements we have obtained a negative loss value, which can be attributed to poor waveguide quality. Nevertheless, a consistently low loss was measured for the longest three implanted sections. If we take only the lowest measured loss into account we can estimate the loss to be lower than about 200 dB/cm. Given the etch depth of about 200 nm in this case the mode overlap is 0.8% (calculated with a mode solver), leading to an approximate material loss of 6000 cm^{-1}, which is about 4 times higher than the values we have reported in Chapter 3. A similar calculation for the iodine etched samples prior to baking gives a material loss of about 30,000 cm^{-1}. We will come back to these numbers in the next section where we discuss laser facet polishing.

A detailed study of iodine enhanced etching of InP was recently presented in Refs. [49, 127, 128]. It is reported that the removal rate of indium triiodide (InI_3, the reaction product of the chemical reaction between InP and iodine) limits the etch yield at room temperature. This can be avoided by heating the stage during the etching to typically 150°C. It is likely that a similar process, i.e. the removal of a reaction product layer, occurs when the samples are baked after the etching. Although the modification of a photonic crystal Y splitter was demonstrated in Ref. [49], no clear measurement of the optical losses was presented. This would be desirable to compare both loss reduction schemes.

7.2.5 Conclusions

From the presented measurements we can derive the provisional conclusion that the optical losses of both directly etched and iodine enhancement etched passive InP are one to two orders of magnitude larger than than for silicon. These losses are clearly reduced by wet etching after direct FIB milling and by baking after iodine enhanced etching, although they remain higher than in FIB etched silicon.

7.3 Fabrication and modification of active III-V devices

In the previous section we have discussed the etching of passive InP waveguides and ways to reduce the optical losses. Wet etching has come out as a good technique to reduce the optical losses after direct etching. However, this technique is not desirable for active structures since the mixture of sulfuric acid and peroxide etches ternary and quaternary layers that reach the surface. To use wet etching for the cleaning of for example FIB etched laser facets a new mixture that selectively removes the damaged layer and not the active layer is required. We did not find an appropriate mixture, so we will concentrate on iodine enhanced etching and baking for the reduction of the optical losses. In a first paragraph we present the fabrication of a microdisk laser, in the second paragraph we discuss the fabrication of Fabry-Perot laser facets or mirrors.

7.3.1 Microdisk

To verify the feasibility of nanophotonic device fabrication with FIB we have etched microdisks in an active InP based membrane on oxide. An InP membrane containing multiple strained InGaAsP quantum wells is transferred from growth substrate to a silicon substrate with an intermediate oxide layer by bonding. More details on this substrate and on the fabrication of microdisk lasers by optical lithography are discussed in Ref. [7]. To verify the feasibility of FIB etched microdisk lasers, identical disks were fabricated (a 700 nm thick membrane, disk diameters from 2 to 10 μm). The membrane was first covered with a 50 nm alumina layer to allow the etching of vertical sidewalls. The alumina mask was then etched by using TFA gas enhancement and etching a ring with inner diameter ranging from 2 to 10 μm, an etch dose of 0.85 - 1.7 $\times$ 10^{17} Ga^{+}/cm^{2} and a beam cur-

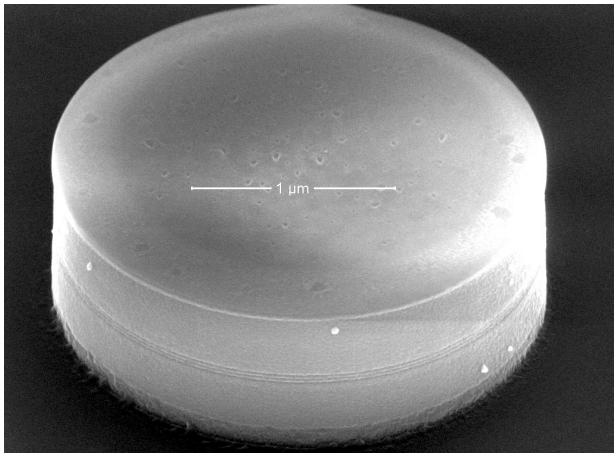

Figure 7.6: FIB etched microdisk. We have observed no lasing in a photoluminescence experiment due to the FIB induced optical loss.

rent of 0.1 nA. In a subsequent step the same ring was etched with iodine etch enhancement (beam current 0.1 nA and etch dose of 4.7 $\times$ 10^{16} Ga^{+}/cm^{2}) after one to two ion imaging alignment scans. After fabrication the sample was baked on a hotplate in nitrogen for two hours at 300°C. The smallest resulting microdisk is displayed in Fig. 7.6.

The microdisks were characterized on a micro-photoluminescence setup by pumping with light from a red diode laser (20 mW) and by capturing the luminescence signal with a multimode fiber connected to a spectrum analyzer. The optical lithography fabricated lasers showed clear lasing peaks, whereas non of the FIB fabricated disks showed lasing. A similar experiment was performed by providing pump light from a 980 nm laser (70 mW) coupled to a standard single mode fiber. In this experiment the luminescence was captured with a multimode fiber aligned closely to the disk. The result of both experiments were similar: spontaneous emission around 1550 nm was observed (although decreased in the disk as compared to the slab region) but no lasing was observed.

The reason that these experiments were not successful is obvious from the results from the previous section. Even though the optical losses are greatly reduced by using iodine etch enhancement and baking they are still in the order of 6000 dB/cm for a thin layer on the outer shell of the disk. This is exactly where the lasing mode (a whispering gallery mode) propagates. This mode has a large overlap

with the damaged region; therefore an unrealistically high modal loss occurs. Considering that the optical material gain is typically 1000-3000 cm-1 (not taking into account the mode confinement in the active layer) the mode will never develop sufficient gain for lasing.

It can therefore be concluded that the FIB fabrication of InP based nanophotonic structures with the optical mode close to the etched region is unrealistic.

7.3.2 Etching of laser facets and mirrors

Another experiment to assess the feasibility of FIB etching of active III-V devices is the etching of laser facets. This is important for applications such as slanted total internal reflection mirrors to vertically couple light out of horizontal cavity mirrors (for example for flip-chip bonding on top of vertical grating couplers). We will assess the FIB induced losses on such vertically etched walls (as opposed to implantation from the top) by polishing the facets of cleaved Fabry-Perot mirrors. These lasers show an increase in threshold current from which one can derive the reduced optical reflection of the polished facet. From this value we will calculate the loss per reflection, which is the measure of interest for total internal reflection mirrors. We will discuss the reduction of the induced losses (or thus increase of the facet reflection) by using iodine gas enhancement and by subsequent baking.

First we will discuss how to derive the change in mirror reflection from the change in laser threshold current. Let us consider the definition of threshold current density as the carrier current density required to obtain population inversion:

$$I_{th} = \frac{qN_{th}}{\tau_c}, \tag{7.1}$$

where q is the elementary charge, τ_c is the carrier lifetime, and N_{th} is the threshold carrier density. This can be written as

$$I_{th} = \frac{q}{\tau_c}\Big(N_{tr} + \frac{1}{G\tau_p}\Big), \tag{7.2}$$

with N_{tr} the carrier density at transparency, G the modal gain, and τ_p the photon lifetime inside the cavity. The photon lifetime takes into account the loss of photons both by internal absorption and by transmission through the mirror facets and is therefore inversely

proportional to the loss coefficients:

$$\frac{1}{\tau_p} \propto [\alpha_{int} + \alpha_{mir}] \propto \left[\alpha_{int} + \frac{1}{2L} \ln\left(\frac{1}{R_1 R_2}\right)\right], \tag{7.3}$$

where L is the length of the cavity and R_1 and R_2 represent the power reflection coefficients of the two mirrors. Thus if we want to determine the difference in mirror reflectance from a change in threshold current by FIB polishing of a single facet, the following relation can be used:

$$\frac{I_{th,before}}{I_{th,after}} = \frac{\alpha_{mir,after} + \alpha_{int}}{\alpha_{mir,before} + \alpha_{int}}, \tag{7.4}$$

considering that the carrier density required for transparency is much smaller than at the laser threshold. If we express the reflection of the FIB etched facet as R_{fib} and the standard facet as R (i.e. about 30%) we can deduce after some manipulation:

$$R_{fib} = \frac{1}{\exp\left[2L\frac{I_{th,before}}{I_{th,after}}\left(\frac{1}{L}\ln\frac{1}{R} + \alpha_{int}\right) - \ln\frac{1}{R} - 2L\alpha_{int}\right]}. \tag{7.5}$$

To estimate the material loss from the reduced reflection let us assume that the FIB damaged layer has a thickness of 30 nm [129]. The reduced reflection is then caused by absorption when the light passes through the damaged layer (twice for each round trip). The loss per unit length α_{fib} (cm^{-1}) can therefore be calculated as follows:

$$\alpha_{fib}[cm^{-1}] = \frac{R - R_{fib}}{R} \times \frac{10^7}{60\ nm}. \tag{7.6}$$

For the experiment we have used two Fabry-Perot lasers (with ridge widths of 5 and 8 μm) on a sample with multiple strained quantum wells and an internal loss of about 20 cm^{-1}. The lasers were cleaved with a length of 800 μm. The threshold current was measured by electrically pumping the lasers and measuring the output power at one of the facets with a photodetector. The measurement was repeated after FIB polishing of one laser facet with a beam current of 100 pA and iodine etch enhancement. Subsequently the samples were baked for 1 hour at 200°C on a hotplate in nitrogen. The temperature was chosen lower than previously to avoid deterioration of the active devices, considering that temperature of about 150°C are sufficient for loss reduction during in situ heating [49]. The measured threshold currents and calculated facet reflection and

	I_{th}	R_{fib}	α_{fib} (cm^{-1})	loss per reflection (dB)
device 1 before etch	24.2	0.3		
device 1 after iodine etch	25.5	0.22	43,000	1.3
device 1 after iodine etch +bake	24.7	0.27	18,000	0.5
device 2 before etch	31.0	0.3		
device 2 after iodine etch	32.5	0.23	40,000	1.2
device 2 after iodine etch + bake	31.8	0.26	22,000	0.6

Table 7.2: The measured threshold current of two Fabry-Perot lasers of which one facet was polished by iodine enhanced FIB etching. The reflectivity of the polished facet, material loss and loss per reflection were calculated according to the presented model.

material loss are presented in Table 7.2. The loss values prior to baking are of the same order of magnitude as presented in the previous paragraph (∼30,000 cm^{-1}). However, baking at 200°C does not reduce the loss to the previously mentioned value of 6000 cm^{-1}.

If we calculate the expected loss per reflection for a directly etched facet (with an approximate material loss value of 10^5 cm^{-1}) we obtain about 5 dB loss per reflection. The use of iodine etch enhancement can reduce these losses considerably, to about 0.5 dB per reflection. This improvement is important for the etching of total internal reflection mirrors, angled facets, etc.

As discussed similar devices were demonstrated in literature. For example the fabrication of total internal reflection mirrors in Ref. [121], however, no loss characteristics were measured. A similar result was presented in Ref. [120]: the fabrication of a 45° angled mirror to vertically couple light out of a horizontal cavity DFB mirror. Again no loss measurements were reported. It is likely that in both reported devices no loss reduction mechanisms were used. The etch process developed in this work can reduce the loss per reflection of these mirrors by several dB's.

7.4 Conclusions

In this chapter we have discussed a literature overview of III-V devices that were successfully modified or fabricated by FIB etching. Most of these devices are active, and the FIB induced loss of optical power (in a small volume) is usually compensated by gain in the rest of the device (large volume). However, for nanophotonic applications, where the optical mode mostly has a reasonably large overlap with the lossy FIB etched region, gain is not sufficient to compensate for the FIB induced loss. We have for the first time characterized the FIB induced loss in passive InP waveguides and studied loss reduction mechanisms such as iodine enhanced etching, wet etching, and thermal treatments. The result is a considerable reduction of the optical losses. For a typical application such as the etching of a total internal reflection mirror in a horizontal laser we have reduced the optical loss to 0.5 dB by using iodine enhancement followed by a thermal treatment.

Chapter 8

Conclusions and future perspectives

FIB fabrication of nanophotonic devices

At the onset of this work FIB had grown into a versatile fabrication technique that allows for direct etching of three dimensional nanostructures. Its potential to fabricate nanophotonic structures had been demonstrated in literature with moderate success, due to the high optical losses that FIB etching induces in semiconductor materials. Therefore a detailed analysis of FIB induced optical losses was desirable.

In this work we have studied optical losses in Si and InP, which are the dominant material systems for nanophotonic devices at wavelengths around 1.5 μm. We have performed experiments to measure the losses induced at horizontally and vertically etched structures. These are different, primarily due to the different implantation depth of the ions into the structures. For horizontal structures the loss was measured by implanting and etching the top surface of predefined waveguides. Slots in pre-fabricated waveguides were used as a reference for losses in vertical structures in Si; In InP microdisk lasers and FIB polished laser facets in InP based ridge lasers were used.

The primary goal of this work was to reduce these optical losses. To obtain this we have focused mainly on chemical etch enhancement with iodine gas, although techniques such as wet damage removal and high temperature annealing were also under discussion.

We have found that iodine etch enhancement is efficient in reducing the losses, and even more so when successive baking is performed. This is caused by the low volatility of the etch products at room temperature. This approach was pursued because it is compatible with post processing of finished devices that possibly include metals and polymers (high temperature annealing is not).

We have observed that the losses in Si for horizontally (resp. vertically) etched structures can be approximated by a 40 nm (resp. 10 nm) thick layer of damaged material with a loss of 1650 cm^{-1}. This leads to a typical loss of 100-200 dB/cm in silicon nanophotonic devices, dependent on the overlap between the optical modes and the damaged material. In InP based devices we have measured higher losses (4-10 times higher), which can only be overcome if sufficient gain can be obtained. FIB is therefore less interesting to fabricate nanophotonic devices in InP.

Although the reported losses ($\sim$100 dB/cm) are considerable, it should be noted that the typical maximum device length is 100 μm, which yields a loss of 1 dB per device. This argument is supported by the serial nature of FIB fabrication: it will not likely be used for the fabrication of access waveguides; therefore somewhat higher losses are acceptable. For devices etched without gas enhancement the losses are on the order of 35 dB per device. The reduction to 1 dB that was achieved in this work greatly broadens the horizon of FIB prototyping. This fabrication strategy of iodine enhanced etching in combination with an alumina hardmask was applied in Si for the prototyping of various devices.

The analysis of FIB etching techniques in this work offer important insight in the optical loss mechanisms that cause bad device characteristics. We believe that the presented model with horizontal and vertical structures (with different damaged layer thickness) in Si and InP offers the insight to predict the feasibility of FIB fabrication. In the past it was often not possible to explain why FIB etched structures featured poor device performance. The results from this work help to overcome this hurdle.

The emphasis of FIB fabrication of photonic devices has mostly been on the fabrication of prototypes due to the serial nature of the technique. Nevertheless, we believe that FIB can be a production technology for medium to high volume manufacturing of devices with unprecedentedly small and complex features. Firstly, we have demonstrated that FIB can be used to write only the smallest features on pre-fabricated blank structures. The use of FIB is permitted because these small structures do not require long writing times. An

example of a similar high volume fabrication scheme, currently used in industry, is the FIB trimming of the weight of hard disk writing heads. Furthermore, the presented FIB fabrication of molds with angled features is fully compatible with high-volume replication.

In analogy to writing only the smallest features in a pre-fabricated blank structure, FIB can also be used to make small changes to finished devices that do not fulfill the requirements. This is necessary in many high-performance nanophotonic structures that are fabricated with high-volume fabrication technologies. An example are filters for wavelength division networks, fabricated in silicon by optical deep-UV lithography. Due to the serial nature of FIB these small changes (i.e. trimming) can be made *live*, during characterization of the device. In combination with the recently presented fiber probes this technique is fully compatible with wafer scale testing and trimming and can therefore be adopted for manufacturing of high volumes.

Future perspectives

In this work we have presented the optical characterization of the properties of FIB etched silicon and InP. However, for a more complete understanding of how FIB fabricated nanophotonic devices operate, more specifically electrically pumped sources and modulators, a thorough electrical characterization is desirable. It can be expected that the FIB damaged layer has an increased conductivity and that leakage currents arise. More work is needed to fully understand this effect and predict device performance.

As device functionality and complexity of nanophotonic structures will further increase, FIB as a technology that enables three dimensional nanostructures will become more prominent. Current models for the fabrication of arbitrary 3D shapes with FIB show promising results and demonstrate the thorough insight in structure formation by direct milling. Inverse simulation methods, enabling the milling of arbitrary shapes are therefore within reach.

One could argue that the need for a technique complementary to optical lithography, offering a better resolution, will diminish as optical lithography techniques themselves evolve. However, direct writing techniques do not suffer the resolution limitations of a resist layer; it is therefore likely that these techniques have more potential to become the future fabrication technologies with ultimate resolution. Furthermore the optical loss problems of current FIB systems

are likely to decrease as the energy per impinging nucleon decreases. This evolution is now visible through the commercial availability of the first cluster ion sources.

A clear evolution is visible in commercially available FIB systems towards even more flexibility and versatility. For instance the use of other source elements such as indium can increase the sputter yield and minimize the effects of material damage. Other examples include the use of hot or cold sample stages and machines that operate under a low vacuum. These evolutions lead the way to an ever broader applicability of focused-ion-beam.

Appendix A

Publications

A.1 Patent applications

1. J. Schrauwen, D. Van Thourhout, R. Baets, Method for wavelength trimming of optical components and optical components thus obtained, US-61/021,250 (Pending, 1/2008)

2. J. Schrauwen, S. Scheerlinck, G. Roelkens, D. Van Thourhout, Integrated Photonic Devices Including Refractive Elements and Methods of Coupling Light Between an Integrated Photonic Waveguide and an Optical Element, US-61/054,401 (Pending, 5/2008)

A.2 Journal publications

1. J. Schrauwen, J. Van Lysebettens, T. Claes, K. De Vos, P. Bienstman, D. Van Thourhout, R. Baets, Focused-ion-beam fabrication of slots in silicon waveguides and ring resonators, *IEEE Photonics Technology Letters*, 20(23), p.2004 (2008).

2. S. Scheerlinck, J. Schrauwen, G. Roelkens, D. Van Thourhout, R. Baets, Vertical fiber-to-waveguide coupling using adapted fibers with angled facet fabricated by a simple molding technique, *Applied Optics*, 47(18), p.3241-3245 (2008).

3. D. Van Thourhout, G. Roelkens, R. Baets, W. Bogaerts, J. Brouckaert, P.P.P. Debackere, P. Dumon, S. Scheerlinck,

J. Schrauwen, D. Taillaert, F. Van Laere, J. Van Campenhout, Coupling mechanisms for a heterogeneous silicon nanowire platform, *Semiconductor Science and Technology*, 23, p.064004(9pp) (2008).

4. J. Schrauwen, D. Van Thourhout, R. Baets, Trimming of silicon ring resonator by electron beam induced compaction and strain, *Optics Express*, 16(6), p.3738-3743 (2008).

5. F. Van Laere, T. Claes, J. Schrauwen, S. Scheerlinck, W. Bogaerts, D. Taillaert, L. O'Faolain, D. Van Thourhout, R. Baets, Compact Focusing Grating Couplers for Silicon-on-Insulator Integrated Circuits, *IEEE Photonics Technology Letters*, 19(23), p.1919-1921 (2007)

6. J. Schrauwen, D. Van Thourhout, R. Baets, Iodine enhanced focused-ion-beam etching of silicon for photonic applications, *Journal of applied physics*, 102, p.103104 (2007).

7. S. Scheerlinck, J. Schrauwen, F. Van Laere, D. Taillaert, D. Van Thourhout, R. Baets, Efficient, broadband and compact metal grating couplers for silicon-on-insulator waveguides, *Optics Express*, 15, p.9639-9644 (2007).

8. J. Schrauwen, F. Van Laere, D. Van Thourhout, R. Baets, Focused-ion-beam fabrication of slanted grating couplers in silicon-on-insulator waveguides, *IEEE Photonics Technology Letters*, 19(11), p.816-818 (2007).

9. F. Van Laere, G. Roelkens, M. Ayre, J. Schrauwen, D. Taillaert, D. Van Thourhout, T. F. Krauss, R. Baets, Compact and highly efficient grating couplers between optical fiber and nanophotonic waveguides, *Journal of Lightwave Technology*, 25(1), p.151-156 (2007).

10. J. Schrauwen, D. Van Thourhout, R. Baets, Focused-ion-beam fabricated vertical fiber couplers on silicon-on-insulator, *Applied Physics Letters*, 89, p.141102 (2006).

A.3 International conference publications

1. J. Schrauwen, S. Scheerlinck, D. Van Thourhout, R. Baets, Polymer wedge for perfectly vertical light coupling to silicon wave-

guides, (accepted for publication at) *Photonics West*, United States, (2009).

2. J. Schrauwen, T. Claes, D. Van Thourhout, R. Baets, Focused-ion-beam fabrication of slots in silicon waveguides and ring resonators, (accepted for publication at) *IEEE LEOS Benelux sumposium*, The Netherlands, (2008).

3. J. Schrauwen, J. Van Lysebettens, M. Vanhoutte, D. Van Thourhout, R. Baets, Iodine enhanced FIB etching of silicon for photonic device modification and prototyping, *International workshop on Fib for photonics*, Netherlands, p.4-7 (2008).

4. J. Schrauwen, G. Roelkens, D. Van Thourhout, R. Baets, Focused-ion-beam lithography for prototyping of silicon photonic compontnets, *The 52nd International Conference on electron, ion and photon beam technology and nanofabrication (EIPBN2008)*, United States, (2008).

5. J. Schrauwen, E.J. Klein, F. Ay, W.C.L. Hopman, R.M. De Ridder, D. Van Thourhout, R. Baets, Reducing optical losses in focused-ion-beam etched silicon by annealing, *The 52nd International Conference on electron, ion and photon beam technology and nanofabrication (EIPBN2008)*, United States, (2008).

6. D. Van Thourhout, W. Bogaerts, J. Brouckaert, P. Dumon, G. Roelkens, S. Scheerlinck, S. Selvaraja, J. Schrauwen, D. Taillaert, J. Van Campenhout, P. Bienstman, R. Baets, Silicon nanophotonics on CMOS, *33rd International Conference on Micro- and Nano-Engineering 2007 (MNE07)*, Denmark, p.113-114 (2007).

7. G. Roelkens, J. Schrauwen, D. Van Thourhout, R. Baets, High efficiency fiber-to-waveguide grating couplers in silicon-on-insulator waveguide structures, *Proceedings of OSA Topical Meetings : Integrated Photonics and Nanophotonics and Applications (IPNRA 2007)*, United States, p.paper IMC2 (2007.

8. S. Scheerlinck, J. Schrauwen, F. Van Laere, D. Van Thourhout, R. Baets, Metal grating coupler for Silicon-on-Insulator, *Annual Workshop of the IEEE/LEOS Benelux Student Chapter*, Netherlands, p.17 (2007).

9. S. Scheerlinck, J. Schrauwen, D. Taillaert, D. Van Thourhout, R.Baets, Efficient, broadband and compact metal grating cou-

plers fo silicon-on-insulator, *CLEO/QELS 2007*, United States, (2007).

10. S. Scheerlinck, F. Van Laere, J. Schrauwen, D. Taillaert, D. Van Thourhout, R. Baets, Gold Grating Coupler for Silicon-on-Insulator Waveguides with 34 % Coupling Efficiency, *ECIO*, Denmark, (2007).

11. J. Schrauwen, F. Van Laere, D. Van Thourhout, R. Baets, Focused-ion-beam fabrication of slanted fiber couplers in silicon-on-insulator waveguides, *ECIO*, Denmark, (2007).

12. S. Scheerlinck, J. Schrauwen, D. Van Thourhout, R. Baets, Metal grating for coupling to photonic crystal circuits, *PECS-VII*, United States, p.B-48, (2007).

13. J. Schrauwen, D. Van Thourhout, R. Baets, Focused ion beam for photonics, a new versatile fabrication method, *ePIXnet winterschool 2007*, Switzerland, (2007).

14. J. Schrauwen, F. Van Laere, D. Van Thourhout, R. Baets, Focused-ion-beam fabrication of slanted fiber couplers in silicon-on-insulator waveguides, *IEEE Leos Benelux*, (2006).

15. J. Brouckaert, W. Bogaerts, P. Dumon, J. Schrauwen, D. Van-Thourhout, R. Baets, Planar concave grating demultiplexer on a nanophotonic silicon-on-insulator platform, *IEEE LEOS Annual Meeting Conference Proceedings*, Canada, p.312-313, (2006).

16. G. Roelkens, J. Brouckaert, S. Verstuyft, J. Schrauwen, D. Van Thourhout, R.Baets, Heterogeneous integration of III-V photodetectors and laser diodes on Silicon-on-Insulator waveguide circuits, *IEEE Group IV photonics*, Canada, p.ThB2, (2006).

17. J. Schrauwen, D. Van Thourhout, R. Baets, Focused-Ion-Beam Fabricated Vertical Fiber Couplers on Silicon-on-Insulator Waveguides, *IEEE Group IV Photonics*, Canada, (2006).

18. J. Schrauwen, D. Van Thourhout, R. Baets, Reducing optical losses in devices fabricated with focused ion beam, *ePIXnet wintershool 2006* , Switzerland, (2006).

19. F. Van Laere, G. Roelkens, J. Schrauwen, D. Taillaert, P.Dumon, W. Bogaerts, D. Van Thourhout, R. Baets, Compact grating

couplers between optical fibers and Silicon-on-Insulator photonic wire waveguides with 69% coupling efficiency, *OFC*, United States, p.PDP15, 2006.

A.4 National conference publications

1. J. Schrauwen, D. Van Thourhout, R. Baets, Focused ion beam for photonics: a new versatile fabrication method, *7e UGent-FirW Doctoraatssymposium*, interactive poster session, Belgium, p.paper nr. 20, (2006).

Appendix B

Dose conversion

In the following we give a short summary on how to calculate the implantation dose from the parameters of the FEI and Raith machines. The physical quantity most often used for ion implantation or etching is dose, usually defined as

$$d\left[\frac{\text{number of particles}}{\text{cm}^2}\right]. \tag{B.1}$$

When implanting and doping a semiconductor one is most interested in the concentration of impurities in the substrate (number of particles/cm^3), which is a depth dependant quantity that can be calculated by simulating or measuring the depth profile of the implantation [33]. Typical implantation doses range form 10^{13} cm^{-2} to 10^{16} cm^{-2} and this yields typical impurity concentrations of 10^{17} cm^{-3} to 10^{20} cm^{-3}. However, for particle lithography purposes (ion or electron beam lithography) the dose is usually defined as

$$d_{\text{litho}}\left[\frac{\mu\text{C}}{\text{cm}^2}\right]; \tag{B.2}$$

conversion to implantation dose (B.1) is done by incorporating the charge of a single particle, assuming that all particles have the elementary charge. As an example a lithography dose of 1 μC/cm^2 is converted as follows:

$$\begin{aligned} 1\,\frac{\mu\text{C}}{\text{cm}^2} &= 10^{-6}\,\frac{\text{C}}{\text{cm}^2}\cdot\frac{1}{1.602\cdot 10^{-19}\,\text{C/particle}}, \\ &= 6.24\times 10^{12}\,\frac{\text{particle}}{\text{cm}^2}, \end{aligned} \tag{B.3}$$

which is the same as

$$d\left[\frac{\text{particles}}{\text{cm}^2}\right] = 6.24 \times 10^{12} \cdot d_{\text{litho}}\left[\frac{\mu\text{C}}{\text{cm}^2}\right]. \tag{B.4}$$

This factor can be used to convert between Raith lithography settings and implantation dose (B.1). However, the FEI software uses a different convention. Here every material is accounted a milling rate, in $\mu\text{m}^3/\text{nC}$, and the actual dose is set by the *required etch depth*. This simple model is adequate only for low aspect ratio craters (large area and shallow) and for sufficiently high doses (because for low doses implantation and swelling occur). This *required etch depth* is thus often not the actually milled depth. To convert to (B.1) we will use the example of silicon milling, for which the milling rate in the FEI software was set to 0.15 $\mu\text{m}^3/\text{nC}$. The conversion assumes that for the digital scanning algorithm the dose of an irradiated area is

$$\frac{\text{milling time} \cdot \text{beam current}}{\text{area}}. \tag{B.5}$$

Suppose that we set the FEI software to mill a silicon volume with area A (in units of μm^2) and depth D (in nm). In this case the software will calculate the charge to be administered from the volume V to be removed and the preset milling rate:

$$\begin{aligned} \text{charge [nC]} &= \frac{V\ [\mu\text{m}^3]}{\text{milling rate}\ [\mu\text{m}^3/\text{nC}]}, \\ &= \frac{A\ [\mu\text{m}^2] \cdot D\ [\text{nm}] \cdot 10^{-3}}{\text{milling rate}\ [\mu\text{m}^3/\text{nC}]}. \end{aligned} \tag{B.6}$$

Division by the area, in cm^2, and conversion of the charge unit yields the lithography dose as in (B.2):

$$\begin{aligned} d_{\text{litho}}\ [\mu\text{C}/\text{cm}^2] &= \frac{\text{charge}\ [\mu\text{C}]}{A\ [\text{cm}^2]}, \\ &= \frac{D\ [\text{nm}] \cdot 10^{-3}}{\text{milling rate}\ [\mu\text{m}^3/\text{nC}]} \cdot \frac{10^8}{10^3}. \end{aligned} \tag{B.7}$$

Taking (B.4) into account this yields

$$d\left[\frac{\text{particles}}{\text{cm}^2}\right] = 6.24 \times 10^{14} \cdot \frac{D\ [\text{nm}]}{\text{milling rate}\ [\mu\text{m}^3/\text{nC}]}. \tag{B.8}$$

As an example, when silicon is etched with a *set depth* of 1 nm, the dose is

$$d = 6.24 \cdot \frac{1}{0.15} \times 10^{14} = 4.16 \times 10^{15}\ \text{cm}^{-2}. \tag{B.9}$$

Each material or gas enhanced etch program has a different milling rate in the FEI software; Table B.1 summarizes them.

Etch program	Used gas	FEI milling rate (μm^3/nC)	*set depth*	dose (Ga^+/cm^2)
Si	None	0.15	1 nm	4.16 x 10^{15}
			0.24 nm	1 x 10^{15}
Enhanced etch	I_2	0.2	1 nm	3.12 x 10^{15}
			0.32 nm	1 x 10^{15}
Delineation etch	TFA	1.1	1 nm	5.67 x 10^{14}
			1.76 nm	1 x 10^{15}
Carbon etch	H_2O	0.3	1 nm	2.08 x 10^{15}
			0.48 nm	1 x 10^{15}

Table B.1: Summary of dose and *set depth* conversions for the FEI software of the Nova Nanolab 600 machine, as calculated with equation (B.8).

Appendix C

Characterization techniques

This appendix gives a short overview of the various sample characterization techniques used in this work for element and chemical analysis, surface analysis, concentration depth profiling and crystallographic analysis.

C.1 EDS

Energy dispersive X-ray spectroscopy is a characterization technique used for element analysis. It relies on the interaction between matter and bombarding electrons and is most commonly used in combination with electron microscopes, both in SEM and TEM. When electrons in the keV range bombard a sample they can eject electrons from core shells leaving behind a hole. When electrons from higher energy orbits fill this hole they emit characteristic X-rays that carry the signature of the chemical element. The X-rays are then collected by a liquid nitrogen cooled detector close the the beam impact. The energy spectrum shows several peaks that are correlated to the chemical elements present in the sample. Typically the technique is not sensitive for low-energy X-rays that are generated by light elements, and many elements show overlapping peaks. The range of the ejected X-rays is correlated to the energy of the impinging electrons. By varying the electron energy one can change the volume from which the X-rays are emitted.

C.2 XPS

X-ray photoelectron spectroscopy uses electrons emitted from the top 1-10 nm of a sample in response to being bombarded with X-rays. The binding energy of the emitted photons is calculated by subtracting their kinetic energy from the initial X-ray energy. The number of detected electrons is then plotted as function of the electron binding energy, yielding characteristic peaks for electrons from different elements in different electronic configurations or chemical bonds. The energy resolution of this technique is thus determined by the resolution of the incident X-ray beam, and is smaller for commercially available XPS tools than for synchrotron-based experiments. This technique has a detection limit of typically 0.1 at%; and can be used for depth profiling if it is used in combination with e.g. intermediate argon ion beam milling of the surface. For further reading and list of spectra we refer to Ref. [130].

C.3 SIMS

Secondary ion mass spectroscopy detects the secondary particles that are ejected from the sample surface by sputtering with a primary ion beam. Only the charged ejected particles can be used for mass separation by electromagnetic lenses. Although only a small amount of the ejected particles is charged, SIMS is the most sensitive surface analysis technique and allows detection in the parts per billion range. E.g. in silicon - with a density of 5×10^{22} cm^{-3} - impurities with concentrations of 10^{13} cm^{-3} can be measured. This is thanks to detection of the ejected particles after mass separation with electron multipliers that can detect the impact of a single ion. The technique can be used for analysis of surfaces but also for depth profiling in a dynamic mode. While a crater is etched the ejected ions are detected after mass separation.

C.4 EBSD

Electron backscatter diffraction is used to study crystallographic properties of materials in a SEM. When a crystalline material is mounted at an angle of 70° with respect to the electron beam, the Bragg conditions for backscatter diffraction are potentially satisfied for various crystal planes. Due to the high angle of incidence these electrons can escape from the sample surface, to collide with a fluorescent screen

that is positioned close to the sample. The screen - imaged with a camera - shows patterns that are characteristic for the crystal structure and orientation of the sample. This technique can thus identify the seven crystal systems and their orientation in the sample, and is capable of making crystal orientation maps of materials with grains or different phases. The technique probes only the top surface of the sample (about the top 20-100 nm) and yields no patterns when an amorphous material studied. In this work the technique was used to verify the recrystallization of a amorphous silicon surface.

C.5 TEM

Transmission electron microscopy is a high-resolution microscopy technique where the specimen, in the shape of a thin slice, is used as a transparency in a broad electron beam that is imaged onto a screen or camera. The technique generally uses 200-300 keV electrons and requires a specimen thickness of typically less than 100 nm. The image resolution is often better than 0.1 nm and individual atoms can be distinguished. Sample preparation can be done by mechanical polishing and ion milling of part of a sample that is glued on a TEM *grid*. However, site-specific TEM inspection is difficult with standard techniques and requires FIB liftout of a specimen lamella.

Appendix D

Simulation techniques

This appendix gives a short overview of the various simulation techniques that were used in this work: mode solvers, FDTD simulation tools and a general finite element solver.

D.1 FDTD

The finite difference time domain (FDTD) method uses a discretized space and time to solve the time dependant Maxwell's equations. The 2D or 3D simulation setup is divided in small discrete volumes to which correspond discrete electromagnetic field components. These are calculated in a leap-frog manner: first the electric field is calculated in a grid volume at a certain point in time; then the magnetic field for the same volume is calculated in the next time-step. Thanks to the arbitrary choice of the grid this technique is suited for devices with any shape, including angled structures. Furthermore, as long as a sufficiently broadband input pulse is used, the time domain method yields full spectral behavior of a device with a single simulation. However, since this technique requires a gridding that is sufficiently fine to resolve the smallest wavelength and the smallest features of a simulation, it becomes slow for a large variety of devices such as long thin structures. These are more conveniently modeled with mode solvers. In this work the commercial package OMNISIM was used, it can cope with 2D and 3D simulations, including metals.

D.2 Mode solvers

This approach of electromagnetic simulations solves Maxwell's equations in the frequency domain. It uses the optical modes supported by slab waveguides and the effective index method to calculate modes in a 2D cross-section of a device. The calculated modes are then propagated along e.g. the length of a waveguide or a laser cavity and transmission and reflection matrices are calculated when the cross-section of the device changes. This approach is orders of magnitude faster than the FDTD method for a large variety of devices such as many waveguide-based structures (couplers, bends, splitter,...). However, due to the inherent composition of devices from horizontal and vertical interfaces this method is not well suited for angled structures, since this requires a large number of thin slices and therefore slows down the simulation. Furthermore, to investigate the spectral behavior the simulation has to be run several times at different wavelengths. In this work we have used the commercially available FIMMWAVE software and the CAMFR software developed in our group.

D.3 Finite element solver

Finite element methods are used to look for approximate solutions of partial differential equations or integral equations. In this work we have used the commercial software COMSOL to calculate stress after volume compaction of a material in a 2D approximation. First a grid with variable mesh size was defined, then a portion of material was contracted by using the thermal expansion equations in the software (by setting the thermal expansion coefficient zero in non-compacted regions of the simulation space and using an arbitrary temperature change). Then the stress and strain in the setup were calculated, taking into account the various material properties. The program COMSOL can be used for various engineering and physics problems involving simple or coupled differential equations.

Bibliography

[1] T. Tsuchizawa, K. Yamada, H. Fukuda, T. Watanabe, J. Takahashi, M. Takahashi, T. Shoji, E. Tamechika, S. Itabashi, and H. Morita. Microphotonics devices based on silicon microfabrication technology. *IEEE Journal of Selected Topics in Quantum Electronics*, 11(1):232–240, 2005.

[2] P. Dumon, W. Bogaerts, D. Van Thourhout, D. Taillaert, R. Baets, J. Wouters, S. Beckx, and P. Jaenen. Compact wavelength router based on a silicon-on-insulator arrayed waveguide grating pigtailed to a fiber array. *Optics Express*, 14(2):664–669, 2006.

[3] Q. F. Xu, B. Schmidt, S. Pradhan, and M. Lipson. Micrometre-scale silicon electro-optic modulator. *Nature*, 435(7040):325–327, 2005.

[4] H. S. Rong, R. Jones, A. S. Liu, O. Cohen, D. Hak, A. Fang, and M. Paniccia. A continuous-wave raman silicon laser. *Nature*, 433(7027):725–728, 2005.

[5] G. Roelkens, D. Van Thourhout, R. Baets, R. Notzel, and M. Smit. Laser emission and photodetection in an inp/ingaasp layer integrated on and coupled to a silicon-on-insulator waveguide circuit. *Optics Express*, 14(18):8154–8159, 2006.

[6] A. W. Fang, R. Jones, H. Park, O. Cohen, O. Raday, M. J. Paniccia, and J. E. Bowers. Integrated algainas-silicon evanescent racetrack laser and photodetector. *Optics Express*, 15(5):2315–2322, 2007.

[7] J. Van Campenhout, P. Rojo Romeo, P. Regreny, C. Saessal, D. Van Thourhout, S. Verstuyft, L. Di Cioccio, J.-M. Fedeli, C. Lagahe, and R. Baets. Electrically pumped inp-based microdisk lasers integrated with a nanophotonic silicon-on-insulator waveguide circuit. *Optics Express*, 15(11):6744–6749, 2007.

[8] J. A. W. Heymann, M. Hayles, I. Gestmann, L. A. Giannuzzi, B. Lich, and S. Subramaniam. Site-specific 3d imaging of cells and tissues with a dual beam microscope. *Journal of Structural Biology*, 155(1):63–73, 2006.

[9] P. Olivero, S. Rubanov, P. Reichart, B. C. Gibson, S. T. Huntington, J. R. Rabeau, A. D. Greentree, J. Salzman, D. Moore, D. N. Jamieson, and S. Prawer. Characterization of three-dimensional microstructures in single-crystal diamond. *Diamond and Related Materials*, 15(10):1614–1621, 2006.

[10] J. C. Weeber, Y. Lacroute, A. Dereux, E. Devaux, T. Ebbesen, C. Girard, M. U. Gonzalez, and A. L. Baudrion. Near-field characterization of bragg mirrors engraved in surface plasmon waveguides. *Physical Review B*, 70(23):–, 2004.

[11] P. Muhlschlegel, H. J. Eisler, O. J. F. Martin, B. Hecht, and D. W. Pohl. Resonant optical antennas. *Science*, 308(5728):1607–1609, 2005.

[12] J. Gierak, E. Bourhis, M. N. M. Combes, Y. Chriqui, I. Sagnes, D. Mailly, P. Hawkes, R. Jede, L. Bruchhaus, L. Bardotti, B. Prevel, A. Hannour, P. Melinon, A. Perez, J. Ferre, J. P. Jamet, A. Mougin, C. Chappert, and V. Mathet. Exploration of the ultimate patterning potential achievable with focused ion beams. *Microelectronic Engineering*, 78-79:266–278, 2005.

[13] R. Nassar, M. Vasile, and W. Zhang. Mathematical modeling of focused ion beam microfabrication. *Journal of Vacuum Science & Technology B*, 16(1):109–115, 1998.

[14] M. J. Vasile, R. Nassar, J. Xie, and H. Guo. Microfabrication techniques using focused ion beams and emergent applications. *Micron*, 30(3):235–244, 1999.

[15] M. J. Vasile, J. S. Xie, and R. Nassar. Depth control of focused ion-beam milling from a numerical model of the sputter pro-

cess. *Journal of Vacuum Science & Technology B*, 17(6):3085–3090, 1999.

[16] Y. Fu and N. K. A. Bryan. Fabrication of three-dimensional microstructures by two-dimensional slice by slice approaching via focused ion beam milling. *Journal of Vacuum Science & Technology B*, 22(4):1672–1678, 2004.

[17] H. B. Kim, G. Hobler, A. Steiger, A. Lugstein, and E. Bertagnolli. Full three-dimensional simulation of focused ion beam micro/nanofabrication. *Nanotechnology*, 18(24):245303, 2007.

[18] S. Rennon, L. Bach, H. Konig, J. P. Reithmaier, A. Forchel, J. L. Gentner, and L. Goldstein. Nanoscale patterning by focused ion beam enhanced etching for optoelectronic device fabrication. *Microelectronic Engineering*, 57-8:891–896, 2001.

[19] A. J. Steckl and I. Chyr. Focused ion beam micromilling of gan and related substrate materials (sapphire, sic, and si). *Journal of Vacuum Science & Technology B*, 17(2):362–365, 1999.

[20] Q. Ren, B. Zhang, J. Xu, Z. S. Zhang, Y. B. Jin, Y. Qian, and D. P. Yu. Etched facet and semiconductor/air dbr facet of a algainp laser diode prepared by focused ion beam milling. *Solid State Communications*, 130(6):433–436, 2004.

[21] T. Stomeo, G. Visimberga, M. T. Todaro, A. Passaseo, R. Cingolani, M. De Vittorio, S. Cabrini, A. Carpentiero, and E. Di Fabrizio. Rapid prototyping of two-dimensional photonic crystal devices by a dual beam focused ion beam system. *Microelectronic Engineering*, 78-79:417–421, 2005.

[22] N. F. Yu, J. Fan, Q. J. Wang, C. Pflugl, L. Diehl, T. Edamura, M. Yamanishi, H. Kan, and F. Capasso. Small-divergence semiconductor lasers by plasmonic collimation. *Nature Photonics*, 2(9):564–570, 2008.

[23] D. J. Moss, V. G. Ta'eed, B. J. Eggleton, D. Freeman, S. Madden, M. Samoc, B. Luther-Davies, S. Janz, and D. X. Xu. Bragg gratings in silicon-on-insulator waveguides by focused ion beam milling. *Applied Physics Letters*, 85(21):4860–4862, 2004.

[24] A. J. Danner, J. J. Raftery, N. Yokouchi, and K. D. Choquette. Transverse modes of photonic crystal vertical-cavity lasers. *Applied Physics Letters*, 84(7):1031–1033, 2004.

[25] Y. Tanaka, M. Tymczenko, T. Asano, and S. Noda. Fabrication of two-dimensional photonic crystal slab point-defect cavity employing local three-dimensional structures. *Japanese Journal of Applied Physics Part 1-Regular Papers Brief Communications & Review Papers*, 45(8A):6096–6102, 2006.

[26] J. P. Justice, P. Lambkin, M. Meister, R. Winfield, and B. Corbett. Monolithic integration of wavelength-scale diffractive structures on red vertical-cavity lasers by focused ion beam etching. *IEEE Photonics Technology Letters*, 16(8):1795–1797, 2004.

[27] K. E. Zinoviev and C. Dominguez. Diffraction grating couplers milled in si3n4 rib waveguides with a focused ion beam. *Optics Express*, 13(21):8618–8624, 2005.

[28] H. Lohmeyer, K. Sebald, J. Gutowski, R. Kroger, C. Kruse, D. Hommel, J. Wiersig, and F. Jahnke. Resonant modes in monolithic nitride pillar microcavities. *European Physical Journal B*, 48(3):291–294, 2005.

[29] M. P. Bernal, N. Courjal, J. Amet, M. Roussey, and C. H. Hou. Lithium niobate photonic crystal waveguides: Far field and near field characterisation. *Optics Communications*, 265(1):180–186, 2006.

[30] D. Freeman, S. Madden, and B. Luther-Davies. Fabrication of planar photonic crystals in a chalcogenide glass using a focused ion beam. *Optics Express*, 13(8):3079–3086, 2005.

[31] P. S. Chan, H. K. Tsang, and C. Shu. Mode conversion and birefringence adjustment by focused-ion-beam etching for slanted rib waveguide walls. *Optics Letters*, 28(21):2109–2111, 2003.

[32] P. Sigmund. Theory of sputtering .i. sputtering yield of amorphous and polycrystalline targets. *Physical Review*, 184(2):383, 1969.

[33] J. F. Ziegler. Srim-2003. *Nuclear Instruments & Methods in Physics Research Section B-Beam Interactions with Materials and Atoms*, 219-20:1027–1036, 2004.

[34] E. Chason, S. T. Picraux, J. M. Poate, J. O. Borland, M. I. Current, T. D. delaRubia, D. J. Eaglesham, O. W. Holland, M. E. Law, C. W. Magee, J. W. Mayer, J. Melngailis, and A. F. Tasch.

Ion beams in silicon processing and characterization. *Journal of Applied Physics*, 81(10):6513–6561, 1997.

[35] A. Meldrum, R. F. Haglund, L. A. Boatner, and C. W. White. Nanocomposite materials formed by ion implantation. *Advanced Materials*, 13(19):1431–+, 2001.

[36] A. Lugstein, B. Basnar, G. Hobler, and E. Bertagnolli. Current density profile extraction of focused ion beams based on atomic force microscopy contour profiling of nanodots. *Journal of Applied Physics*, 92(7):4037–4042, 2002.

[37] Y. Yamamura and H. Tawara. Energy dependence of ion-induced sputtering yields from monatomic solids at normal incidence. *Atomic Data and Nuclear Data Tables*, 62(2):149–253, 1996.

[38] N. Laegreid and G.K. Wehner. Sputtering yields of metals for ar+ and ne+ ions with energies from 50 to 600 ev. *Journal of Applied Physics*, 32(3):365–369, 1961.

[39] J. S. Williams. Ion implantation of semiconductors. *Materials Science and Engineering a-Structural Materials Properties Microstructure and Processing*, 253(1-2):8–15, 1998.

[40] R. L. Kubena and J. W. Ward. Current-density profiles for a ga+ ion microprobe and their lithographic implications. *Applied Physics Letters*, 51(23):1960–1962, 1987.

[41] J. P. Reithmaier and A. Forchel. Focused ion-beam implantation induced thermal quantum-well intermixing for monolithic optoelectronic device integration. *IEEE Journal of Selected Topics in Quantum Electronics*, 4(4):595–605, 1998.

[42] D. Petit, C. C. Faulkner, S. Johnstone, D. Wood, and R. P. Cowburn. Nanometer scale patterning using focused ion beam milling. *Review of Scientific Instruments*, 76(2):–, 2005.

[43] Company FEI. xt nova nanolab user's manual, 2005.

[44] A. A. Tseng. Recent developments in micromilling using focused ion beam technology. *Journal of Micromechanics and Microengineering*, 14(4):R15–R34, 2004.

[45] T. Ishitani and H. Kaga. Calculation of local temperature rise in focused-ion-beam sample preparation. *Journal of Electron Microscopy*, 44(5):331–336, 1995.

[46] A. A. Tseng. Recent developments in nanofabrication using focused ion beams. *Small*, 1(10):924–939, 2005.

[47] S. Reyntjens and R. Puers. A review of focused ion beam applications in microsystem technology. *Journal of Micromechanics and Microengineering*, 11(4):287–300, 2001.

[48] M. Prestigiacomo, L. Roussel, A. Houel, P. Sudraud, F. Bedu, D. Tonneau, V. Safarov, and H. Dallaporta. Studies of structures elaborated by focused ion beam induced deposition. *Microelectronic Engineering*, 76(1-4):175–181, 2004.

[49] V. Callegari, P. M. Nellen, J. Kaufmann, P. Strasser, and F. Robin. Focused ion beam iodine-enhanced etching of high aspect ratio holes in inp photonic crystals. *Journal of Vacuum Science & Technology B*, 25(6):2175–2179, 2007.

[50] R. J. Young, J. R. A. Cleaver, and H. Ahmed. Characteristics of gas-assisted focused ion-beam etching. *Journal of Vacuum Science & Technology B*, 11(2):234–241, 1993.

[51] J Orloff, M Utlaut, and L Swanson. *High resolution Focused Ion Beams*. Kluwer Academic/Plenum publishers, New York, 2003.

[52] K. Edinger and T. Kraus. Modeling of focused ion beam induced chemistry and comparison with experimental data. *Microelectronic Engineering*, 57-8:263–268, 2001.

[53] P. D. Rack, S. Randolph, Y. Deng, J. Fowlkes, Y. Choi, and D. C. Joy. Nanoscale electron-beam-stimulated processing. *Applied Physics Letters*, 82(14):2326–2328, 2003.

[54] Z. Postawa, B. Czerwinski, M. Szewczyk, E. J. Smiley, N. Winograd, and B. J. Garrison. Enhancement of sputtering yields due to c-60 versus ga bombardment of ag111 as explored by molecular dynamics simulations. *Analytical Chemistry*, 75(17):4402–4407, 2003.

[55] A. H. Vanommen. Diffusion of ion-implanted as in sio2. *Journal of Applied Physics*, 56(10):2708–2715, 1984.

[56] L. Romano, A. M. Piro, M. G. Grimaldi, G. M. Lopez, and V. Fiorentini. Influence of point defects injection on the stability of a supersaturated ga-si solid solution. *Physical Review B*, 71(16):–, 2005.

[57] M. Y. Tsai, B. G. Streetman, V. R. Deline, and C. A. Evans. Gallium distribution and electrical activation in ga+-implanted si. *Journal of Electronic Materials*, 8(2):111–126, 1979.

[58] C. H. Chu, Y. F. Hsieh, L. R. Harriott, and H. H. Wade. Structural damage induced by ga+ focused ion-beam implantation in (001) si. *Journal of Vacuum Science & Technology B*, 9(6):3451–3455, 1991.

[59] R. R. Hart, C. L. Anderson, H. L. Dunlap, R. L. Seliger, and V. Wang. High-current density ga+ implantations into si. *Applied Physics Letters*, 35(11):865–867, 1979.

[60] M. Tamura, S. Shukuri, M. Moniwa, and M. Default. Focused ion-beam gallium implantation into silicon. *Applied Physics a-Materials Science & Processing*, 39(3):183–190, 1986.

[61] H. C. Mogul and A. J. Steckl. Rapid thermal annealing effects on si p+-n junctions fabricated by low-energy fib ga+ implantation. *IEEE Electron Device Letters*, 14(3):123–125, 1993.

[62] W. Bogaerts, D. Taillaert, B. Luyssaert, P. Dumon, J. Van Campenhout, P. Bienstman, D. Van Thourhout, R. Baets, V. Wiaux, and S. Beckx. Basic structures for photonic integrated circuits in silicon-on-insulator. *Optics Express*, 12(8):1583–1591, 2004.

[63] W. Bogaerts, R. Baets, P. Dumon, V. Wiaux, S. Beckx, D. Taillaert, B. Luyssaert, J. Van Campenhout, P. Bienstman, and D. Van Thourhout. Nanophotonic waveguides in silicon-on-insulator fabricated with cmos technology. *Journal of Lightwave Technology*, 23(1):401–412, 2005.

[64] D. Taillaert, P. Bienstman, and R. Baets. Compact efficient broadband grating coupler for silicon-on-insulator waveguides. *Optics Letters*, 29(23):2749–2751, 2004.

[65] B. D. Huey and R. M. Langford. Low-dose focused ion beam nanofabrication and characterization by atomic force microscopy. *Nanotechnology*, 14(3):409–412, 2003.

[66] S. Rubanov and P. R. Munroe. Fib-induced damage in silicon. *Journal of Microscopy-Oxford*, 214:213–221, 2004.

[67] R. A. Soref and J. P. Lorenzo. All-silicon active and passive guided-wave components for lambda=1.3 and 1.6 mu-m. *IEEE Journal of Quantum Electronics*, 22(6):873–879, 1986.

[68] V. Chakarian, D. K. Shuh, J. A. Yarmoff, M. C. Hakansson, and U. O. Karlsson. The adsorption of i2 on si(111)-7x7 studied by soft-x-ray photoemission. *Surface Science*, 296(3):383–392, 1993.

[69] D. Rioux, F. Stepniak, R. J. Pechman, and J. H. Weaver. Chemisorption and thermally activated etching of si(100)-2x1 by iodine. *Physical Review B*, 51(16):10981–10988, 1995.

[70] C. M. Aldao and J. H. Weaver. Halogen etching of si via atomic-scale processes. *Progress in Surface Science*, 68(4-6):189–230, 2001.

[71] Y. Yang and J. A. Yarmoff. Internal charge distribution of iodine adatoms on silicon and silicon oxide investigated with alkali ion scattering. *Surface Science*, 573(3):335–345, 2004.

[72] M. Taneya, Y. Sugimoto, and K. Akita. Characterization of subsurface damage in gaas processed by ga+ focused ion-beam-assisted cl-2 etching using photoluminescence. *Journal of Applied Physics*, 66(3):1375–1381, 1989.

[73] Y. Sugimoto, M. Taneya, H. Hidaka, and K. Akita. Reduction of induced damage in gaas processed by ga+ focused-ion-beam-assisted cl-2 etching. *Journal of Applied Physics*, 68(5):2392–2399, 1990.

[74] Y. Sugimoto, M. Taneya, K. Akita, and H. Hidaka. Gaas pattern etching with little damage by a combination of ga+focused-ion-beam irradiation and subsequent cl-2 gas etching. *Journal of Applied Physics*, 68(12):6415–6419, 1990.

[75] A. Pan, Y. L. Wang, C. S. Wu, C. D. Chen, and N. W. Liu. Effects of focused gallium ion-beam implantation on properties of nanochannels on silicon-on-insulator substrates. *Journal of Vacuum Science & Technology B*, 23(6):2288–2291, 2005.

[76] H. H. Tao, C. Ren, S. Feng, Y. Z. Liu, Z. Y. Li, B. Y. Cheng, D. Z. Zhang, and A. Z. Jin. Optical improvement of photonic devices fabricated by ga+ focused ion beam micromachining. *Journal of Vacuum Science & Technology B*, 25(5):1609–1614, 2007.

[77] W. C. L. Hopman, F. Ay, W. B. Hu, V. J. Gadgil, L. Kuipers, M. Pollnau, and R. M. de Ridder. Focused ion beam scan

routine, dwell time and dose optimizations for submicrometre period planar photonic crystal components and stamps in silicon. *Nanotechnology*, 18(19):195305, 2007.

[78] F. Van Laere, T. Claes, J. Schrauwen, S. Scheerlinck, W. Bogaerts, D. Taillaert, L. O'Faolain, D. Van Thourhout, and R. Baets. Compact focusing grating couplers for silicon-on-insulator integrated circuits. *IEEE Photonics Technology Letters*, 19(21-24):1919–1921, 2007.

[79] B. Wang, J. H. Jiang, and G. P. Nordin. Embedded, slanted grating for vertical coupling between fibers and silicon-on-insulator planar waveguides. *IEEE Photonics Technology Letters*, 17(9):1884–1886, 2005.

[80] F. Van Laere, M. V. Kotlyar, D. Taillaert, D. Van Thourhout, T. F. Krauss, and R. Baets. Compact slanted grating couplers between optical fiber and inp-ingaasp waveguides. *IEEE Photonics Technology Letters*, 19(5-8):396–398, 2007.

[81] F. Van Laere, M. Ayre, D. Taillaert, D. Van Thourhout, T. F. Krauss, and R. Baets. Compact and efficient fibre-to-waveguide grating couplers in inp-membrane. *Electronics Letters*, 42(6):343–345, 2006.

[82] G. Roelkens, D. Van Thourhout, and R. Baets. High efficiency silicon-on-insulator grating coupler based on a poly-silicon overlay. *Optics Express*, 14(24):11622–11630, 2006.

[83] G. Roelkens, D. Vermeulen, D. Van Thourhout, R. Baets, S. Brision, P. Lyan, P. Gautier, and J. M. Fedeli. High efficiency diffractive grating couplers for interfacing a single mode optical fiber with a nanophotonic silicon-on-insulator waveguide circuit. *Applied Physics Letters*, 92(13):131101, 2008.

[84] S. Scheerlinck. PhD thesis, University of Ghent, 2008.

[85] S. Scheerlinck, J. Schrauwen, F. Van Laere, D. Taillaert, D. Van Thourhout, and R. Baets. Efficient, broadband and compact metal grating couplers for silicon-on-insulator waveguides. *Optics Express*, 15(15):9625–9630, 2007.

[86] S. Scheerlinck, D. Taillaert, D. Van Thourhout, and R. Baets. Flexible metal grating based optical fiber probe for photonic integrated circuits. *Applied Physics Letters*, 92(3):031104, 2008.

[87] V. R. Almeida, Q. F. Xu, C. A. Barrios, and M. Lipson. Guiding and confining light in void nanostructure. *Optics Letters*, 29(11):1209–1211, 2004.

[88] Q. F. Xu, V. R. Almeida, R. R. Panepucci, and M. Lipson. Experimental demonstration of guiding and confining light in nanometer-size low-refractive-index material. *Optics Letters*, 29(14):1626–1628, 2004.

[89] E. Jordana, J.-M. Fedeli, P. Lyan, J.P. Colonna, P. Gautier, N. Daldosso, L. Pavesi, Y. Lebour, P. Pellegrino, B. Garrido, J. Blasco, F. Cuesta-Soto, and P. Sanchis. Deep-uv lithography fabrication of slot waveguides and sandwiched waveguides for nonlinear applications. In *IEEE Group IV Photonics 2007*, pages 1–3, Japan, 2007.

[90] T. Baehr-Jones, M. Hochberg, C. Walker, and A. Scherer. High-q optical resonators in silicon-on-insulator-based slot waveguides. *Applied Physics Letters*, 86(8):081101, 2005.

[91] W. Cai, Z. Lin, T. Strother, L. M. Smith, and R. J. Hamers. Chemical modification and patterning of iodine-terminated silicon surfaces using visible light. *Journal of Physical Chemistry B*, 106(10):2656–2664, 2002.

[92] P. Dumon, W. Bogaerts, V. Wiaux, J. Wouters, S. Beckx, J. Van Campenhout, D. Taillaert, B. Luyssaert, P. Bienstman, D. Van Thourhout, and R. Baets. Low-loss soi photonic wires and ring resonators fabricated with deep uv lithography. *IEEE Photonics Technology Letters*, 16(5):1328–1330, 2004.

[93] Y. Akahane, T. Asano, B. S. Song, and S. Noda. High-q photonic nanocavity in a two-dimensional photonic crystal. *Nature*, 425(6961):944–947, 2003.

[94] S. Salvaraja, P. Jaenen, S. Beckx, W. Bogaerts, P. Dumon, D. Van Thourhout, and R. Baets. Silicon nanophotonic wire structures fabricated by 193nm optical lithography. *LEOS annual meeting 2007*, 2007.

[95] I. Kiyat, A. Aydinli, and N. Dagli. Low-power thermooptical tuning of soi resonator switch. *IEEE Photonics Technology Letters*, 18(1-4):364–366, 2006.

[96] E. J. Klein, D. H. Geuzebroek, H. Kelderman, G. Sengo, N. Baker, and A. Driessen. Reconfigurable optical add-drop multiplexer using microring resonators. *IEEE Photonics Technology Letters*, 17(11):2358–2360, 2005.

[97] M. K. Seo, H. G. Park, J. K. Yang, J. Y. Kim, S. H. Kim, and Y. H. Lee. Controlled sub-nanometer tuning of photonic crystal resonator by carbonaceous nano-dots. *Optics Express*, 16(13):9829–9837, 2008.

[98] Y. Nasu, M. Kohtoku, M. Abe, and Y. Hibino. Birefringence suppression of uv-induced refractive index with grooves in silica-based planar lightwave circuits. *Electronics Letters*, 41(20):1118–1119, 2005.

[99] H. Haeiwa, T. Naganawa, and Y. Kokubun. Wide range center wavelength trimming of vertically coupled microring resonator filter by direct uv irradiation to sin ring core. *IEEE Photonics Technology Letters*, 16(1):135–137, 2004.

[100] S. Ueno, T. Naganawa, and Y. Kokubun. High uv sensitivity of sion film and its application to center wavelength trimming of microring resonator filter. *IEICE Transactions on Electronics*, E88c(5):998–1004, 2005.

[101] W. Primak and R. Kampwirth. The radiation compaction of vitreous silica. *Journal of Applied Physics*, 39(12):5651–5658, 1968.

[102] W. Primak. Mechanism for radiation compaction of vitreous silica. *Journal of Applied Physics*, 43(6):2745–2754, 1972.

[103] C. B. Norris and E. P. Eernisse. Ionization dilatation effects in fused silica from 2 to 18-kev electron-irradiation. *Journal of Applied Physics*, 45(9):3876–3882, 1974.

[104] S. Garcia-Blanco and J. S. Aitchison. Direct electron beam writing of optical devices on ge-doped flame hydrolysis deposited silica. *IEEE Journal of Selected Topics in Quantum Electronics*, 11(2):528–538, 2005.

[105] A. J. Houghton and P. D. Townsend. Optical-waveguides formed by low-energy electron-irradiation of silica. *Applied Physics Letters*, 29(9):565–566, 1976.

[106] D. Barbier, M. Green, and S. J. Madden. Wave-guide fabrication for integrated-optics by electron-beam irradiation of silica. *Journal of Lightwave Technology*, 9(6):715–720, 1991.

[107] M. Svalgaard, C. V. Poulsen, A. Bjarklev, and O. Poulsen. Direct uv writing of buried singlemode channel wave-guides in ge-doped silica films. *Electronics Letters*, 30(17):1401–1403, 1994.

[108] D. A. Zauner, J. Hubner, K. J. Malone, and M. Kristensen. Uv trimming of arrayed-waveguide grating wavelength division demultiplexers. *Electronics Letters*, 34(8):780–781, 1998.

[109] H. N. J. Fernando, J. Canning, L. Wosinski, B. Jaskorzynska, and M. Dainese. Characterization of ultra-violet-induced changes in planar waveguides. *Journal of Optics a-Pure and Applied Optics*, 5(4):335–340, 2003.

[110] K. De Vos, I. Bartolozzi, E. Schacht, P. Bienstman, and R. Baets. Silicon-on-insulator microring resonator for sensitive and label-free biosensing. *Optics Express*, 15(12):7610–7615, 2007.

[111] D. Taillaert, W. Van Paepegem, J. Vlekken, and R. Baets. A thin foil optical strain gage based on silicon-on-insulator microresonators. *Third European Workshop on Optical Fibre Sensors (EWOFS 2007)*, 6619:661914, 2007.

[112] T. A. Dellin, D. A. Tichenor, and E. H. Barsis. Surface compaction in irradiated vitreous silica. *Bulletin of the American Physical Society*, 21(3):296–296, 1976.

[113] Amnon Yariv and Pochi Yeh. *Optical waves in Crystals*. John Wiley & Sons, Inc., Hoboken, New Jersey, 2003.

[114] R. S. Jacobsen, K. N. Andersen, P. I. Borel, J. Fage-Pedersen, L. H. Frandsen, O. Hansen, M. Kristensen, A. V. Lavrinenko, G. Moulin, H. Ou, C. Peucheret, B. Zsigri, and A. Bjarklev. Strained silicon as a new electro-optic material. *Nature*, 441(7090):199–202, 2006.

[115] G. Roelkens, D. Van Thourhout, and R. Baets. High efficiency grating coupler between silicon-on-insulator waveguides and perfectly vertical optical fibers. *Optics Letters*, 32(11):1495–1497, 2007.

[116] D. Taillaert. *Grating Couplers as Interface between Optical Fibres and Nanophotonic Waveguides*. PhD thesis, University of Ghent, 2004.

[117] M. H. F. Overwijk and J. A. Depoorter. High-quality focused-ion-beam-made mirrors for ingap/ingaalp visible-laser diodes. *Journal of Applied Physics*, 74(12):7048–7053, 1993.

[118] C. Marinelli, M. Bordovsky, L. J. Sargent, M. Gioannini, J. M. Rorison, R. V. Penty, I. H. White, P. J. Heard, M. Benyoucef, M. Kuball, G. Hasnain, T. Takeuchi, and R. P. Schneider. Design and performance analysis of deep-etch air/nitride distributed bragg reflector gratings for alingan laser diodes. *Applied Physics Letters*, 79(25):4076–4078, 2001.

[119] Z. Y. Zhang, I. J. Luxmoore, Q. Jiang, H. Y. Liu, K. M. Groom, D. T. Childs, M. Hopkinson, A. G. Cullis, and R. A. Hogg. Broadband quantum dot superluminescent led with angled facet formed by focused ion beam etching. *Electronics Letters*, 43(10):587–589, 2007.

[120] N Kwong, N Chen, H Qi, S Chen, J.-S. Chen, H Erlig, T.R. Chen, and A. Sherer. Novel single mode laser fabrication using focus ion beam (fib) etching. In *OFC*, page OWI89, U.S., 2006.

[121] K. A. Williams, G. F. Roberts, T. Lin, R. V. Penty, I. H. White, M. Glick, and D. McAuley. Integrated optical 2 x 2 switch for wavelength multiplexed interconnects. *IEEE Journal of Selected Topics in Quantum Electronics*, 11(1):78–85, 2005.

[122] P. Dowd, L. Raddatz, Y. Sumaila, M. Asghari, I. H. White, P. J. Heard, G. C. Allen, R. P. Schneider, M. R. T. Tan, and S. Y. Wang. Mode control in vertical-cavity surface-emitting lasers by post-processing using focused ion-beam etching. *IEEE Photonics Technology Letters*, 9(9):1193–1195, 1997.

[123] Y. L. D. Ho, R. Gibson, C. Y. Hu, M. J. Cryan, J. G. Rarity, P. J. Heard, J. A. Timpson, A. M. Fox, M. S. Skolnick, M. Hopkinson, and A. Tahraoui. Focused ion beam etching for the fabrication of micropillar microcavities made of iii-v semiconductor materials. *Journal of Vacuum Science & Technology B*, 25(4):1197–1202, 2007.

[124] H. Konig, J. P. Reithmaier, and A. Forchel. Highly resolved maskless patterning on inp by focused ion beam enhanced wet chemical etching. *Japanese Journal of Applied Physics Part 1-Regular Papers Short Notes & Review Papers*, 38(10):6142–6144, 1999.

[125] S. Cabrini, A. Carpentiero, R. Kumar, L. Businaro, P. Candeloro, M. Prasciolu, A. Gosparini, C. Andreani, M. De Vittorio, T. Stomeo, and E. Di Fabrizio. Focused ion beam lithography for two dimensional array structures for photonic applications. *Microelectronic Engineering*, 78-79:11–15, 2005.

[126] M. J. Cryan, M. Hill, D. C. Sanz, P. S. Ivanov, P. J. Heard, L. Tian, S. Y. Yu, and J. M. Rorison. Focused ion beam-based fabrication of nanostructured photonic devices. *IEEE Journal of Selected Topics in Quantum Electronics*, 11(6):1266–1277, 2005.

[127] V. Callegari and P. M. Nellen. Spontaneous growth of uniformly distributed in nanodots and ini3 nanowires on inp induced by a focused ion beam. *Physica Status Solidi a-Applications and Materials Science*, 204(6):1665–1671, 2007.

[128] V. Callegari, P. M. Nellen, T. H. Yang, R. Hauert, U. Muller, F. Hernandez-Ramirez, and U. Sennhauser. Surface chemistry and optimization of focused ion beam iodine-enhanced etching of indium phosphide. *Applied Surface Science*, 253(22):8969–8973, 2007.

[129] S. Rubanov. PhD thesis, University of New South Wales, Sydney, 2003.

[130] John F. Moulder, William F. Stickle, Peter E. Sobol, and Kenneth D. Bomben. *Handbook of X-ray photoelectron spectroscopy: A Reference Book of Standard Spectra for Identification and Interpretation of Xps Data*. Eden Prairie, Minn. : Physical Electronics Division, Perkin-Elmer Corp., 1979.